Max-Planck-Institut
für Meteorologie

MAX-PLANCK-GESELLSCHAFT

International Max Planck Research School
on Earth System Modelling

The North Atlantic Deep Western Boundary Current - seasonal cycle, decadal variability and relation to the Atlantic Meridional Overturning Circulation

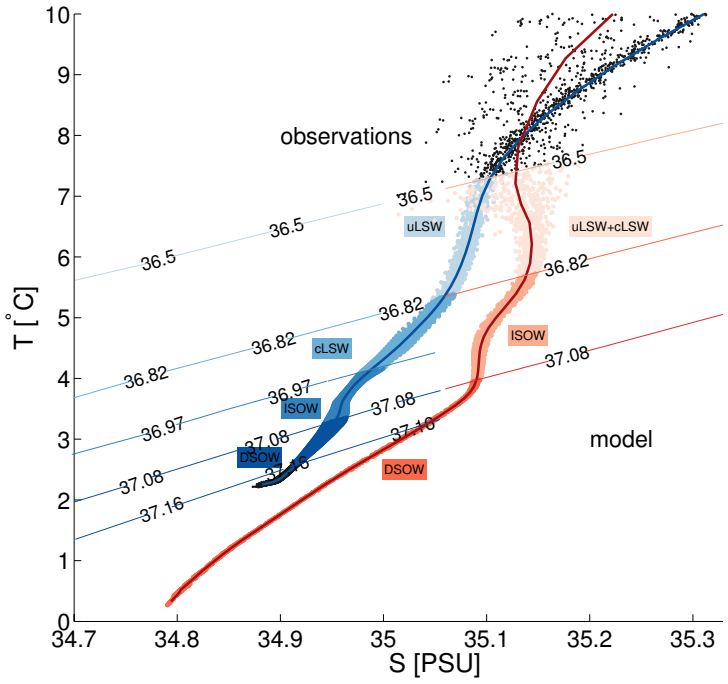

Charlotte Laura Mielke

Hamburg 2015

Berichte zur Erdsystemforschung
Reports on Earth System Science

166
2015

Hinweis

Die Berichte zur Erdsystemforschung werden vom Max-Planck-Institut für Meteorologie in Hamburg in unregelmäßiger Abfolge herausgegeben.

Sie enthalten wissenschaftliche und technische Beiträge, inklusive Dissertationen.

Die Beiträge geben nicht notwendigerweise die Auffassung des Instituts wieder.

Die "Berichte zur Erdsystemforschung" führen die vorherigen Reihen "Reports" und "Examensarbeiten" weiter.

Notice

The Reports on Earth System Science are published by the Max Planck Institute for Meteorology in Hamburg. They appear in irregular intervals.

They contain scientific and technical contributions, including Ph. D. theses.

The Reports do not necessarily reflect the opinion of the Institute.

The "Reports on Earth System Science" continue the former "Reports" and "Examensarbeiten" of the Max Planck Institute.

Anschrift / Address

Max-Planck-Institut für Meteorologie
Bundesstrasse 53
20146 Hamburg
Deutschland

Tel./Phone: +49 (0)40 4 11 73 - 0
Fax: +49 (0)40 4 11 73 - 298

name.surname@mpimet.mpg.de
www.mpimet.mpg.de

Layout

Bettina Diallo and Norbert P. Noreiks
Communication

Copyright

The North Atlantic Deep Western Boundary Current - seasonal cycle, decadal variability and relation to the Atlantic Meridional Overturning Circulation

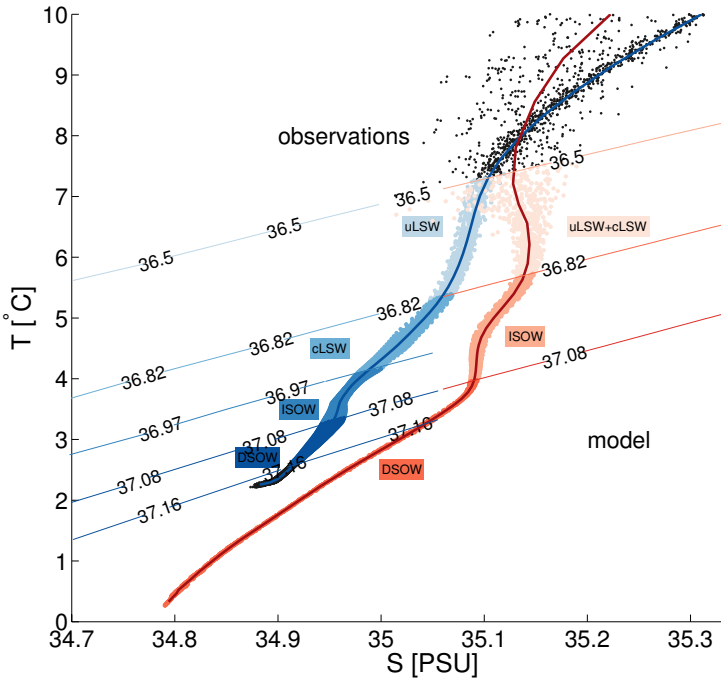

Charlotte Laura Mielke

Hamburg 2015

Charlotte Laura Mielke

Max-Planck-Institut für Meteorologie

Institut für Meereskunde
Universität Hamburg

Bundesstrasse 53
20146 Hamburg

Als Dissertation angenommen
vom Fachbereich Geowissenschaften der Universität Hamburg

auf Grund der Gutachten von
Prof. Dr. Johanna Baehr
und
Dr. Stefan Gary

Berichte zur Erdsystemforschung / Max-Planck-Institut für Meteorologie 166
Reports on Earth System Science / Max Planck Institute for Meteorology 2015

ISSN 1614-1199

Abstract

Despite its importance for the climate system, the natural variability of the Atlantic meridional overturning (AMOC) and its deep western return flow, the Deep Western Boundary Current (DWBC), is still not well understood. Observations of the AMOC or the DWBC exist at single latitudes and are usually limited to a few years, complicating the description of the seasonal cycle and the decadal variability. Also, it is not clear whether observations at one latitude are representative of the variability at other latitudes. Here, I first compare results from a high-resolution ocean model with observations of both scalar quantities and integrated transports to obtain the simulated DWBC. Second, I investigate the meridional coherence of the seasonal cycle and the decadal variability of the DWBC, and compare it to the AMOC's.

I find that the DWBC has a robust seasonal cycle, which is closely related to the local wind stress curl variability. As a result, the DWBC shows a coherent seasonal cycle throughout both the subtropical and the subpolar gyre, but not across the gyre boundary. The modeled AMOC seasonal cycle, however, is coherent throughout the entire North Atlantic, but is 180−degree out-of-phase between the two available observational estimates.

On decadal timescales, the DWBC's variability is also dominated by the local wind stress curl. This implies that the DWBC and the AMOC show opposing behavior if the western boundary and basin interior wind stress curl anomalies are of opposite sign.

My results suggest that both the AMOC and the DWBC at one latitude are representative of the variability of the same quantity over a wide range of adjacent latitudes. AMOC and DWBC may – under certain conditions – be used as a proxy for one another: On seasonal timescales, the DWBC variability itself might be inferred from satellite observations, particularly in the subtropical North Atlantic. For an observational estimate of the seasonal AMOC variability, the thus-obtained DWBC would have to be combined with an estimate of the upper-ocean variability (for example from ARGO data). On decadal timescales, observations of the DWBC could only be used as a proxy for the AMOC variability if the boundary and basin-wide wind stress curl are in phase.

Zusammenfassung

Obwohl die atlantische meridionale Umwälzbewegung (AMOC) und der tiefe westliche Randstrom (DWBC) große Bedeutung für das Klimasystem haben, ist ihre natürliche Variabilität noch unzureichend verstanden. Beobachtungen der AMOC oder des DWBC existieren nur an einzelnen Breiten und sind in der Regel auf wenige Jahre beschränkt. Dies erschwert die Beschreibung des Jahresgangs und der dekadischen Variabilität. Außerdem ist nicht klar, ob Beobachtungen an einem Breitengrad stellvertretend für die Variabilität an anderen Breiten sind. Um einen simulierten DWBC zu erhalten, vergleiche ich Ergebnisse eines hochauflösenden Ozeanmodells mit Beobachtungen skalarer Größen und integrierter Transporte. Anschließend untersuche ich die Kohärenz des Jahresgangs und der dekadischen Variabilität des DWBC, und vergleiche sie mit dem Jahresgang und der dekadischen Variabilität der AMOC.

Auf saisonalen Zeitskalen finde ich heraus, dass der DWBC einen robusten Jahresgang aufweist, der eng mit der Rotation des lokalen Windstresses zusammenhängt. Infolgedessen ist der Jahresgang des DWBC sowohl im subtropischen als auch im subpolaren Wirbel kohärent, jedoch nicht über die Grenze zwischen den Wirbeln hinaus. Der Jahresgang der simulierten AMOC ist dagegen kohärent im gesamten Nordatlantik, im Gegensatz zu den beiden Beobachtungszeitreihen, die 180 Grad außer Phase sind.

Auch auf dekadischen Zeitskalen wird die Variabilität des DWBC von der Rotation des lokalen Windstresses bestimmt. Daraus folgt, dass sich der DWBC und die AMOC gegensätzlich verhalten, wenn das Vorzeichen der Rotation des Windstresses am Westrand und im Becken-Inneren nicht übereinstimmen.

Meine Ergebnisse legen nahe, dass sowohl die AMOC als auch der DWBC an einer Breite stellvertrend für die Variabilität derselben Größe über einen weiten Bereich angrenzender Breiten sind. Unter bestimmten Umständen können AMOC und DWBC wechselseitig auseinander abgeleitet werden: Insbesondere im subtropischen Nordatlantik kann die Variabilität des DWBC auf saisonalen Zeitskalen aus Satellitenbeobachtungen gewonnen werden. Um die beobachtete AMOC-Variabilität zu erhalten müsste der auf diese Weise berechnete DWBC dann mit Beobachtungen der Variabilität des oberen Ozeans (beispielsweise

aus Argo-Daten) kombiniert werden. Auf dekadischen Zeitskalen kann die Variabilität der AMOC nur aus dem DWBC gewonnen werden, wenn die Rotation des Windstresses am Westrand und im Becken-Inneren übereinstimmen.

Contents

1 Introduction

1.1 History of the overturning circulation in the North Atlantic

In 1798, Count Rumford first proposed the existence of an overturning circulation as an explanation for the cold layer in the deep ocean observed some 50 years earlier, which could not be explained by the local surface temperatures (Longworth and Bryden, 2013). Rumford suggested that the cold deep waters must originate from the polar regions, which would in turn require poleward surface currents to uphold continuity. This scheme soon gained acceptance, and was further developed in subsequent years as more observational data became available. While in the beginning, the circulation in the two hemispheres was regarded as strictly separated and more or less symmetric, interhemispheric circulation was first documented in 1921 as more observational data became available (Richardson, 2008).

With an already considerably improved picture of the overturning circulation, the first transbasin section at 25°N was conducted in 1957 (Fuglister, 1960). As temperature and salinity are easier to measure than velocities, the overturning's strength was indirectly estimated by computing the geostrophic shear from hydrographic data. Combined with measurements of the Florida Current, the estimated strength of the overturning of 15 to 18 Sv (1 Sverdrup (Sv) =

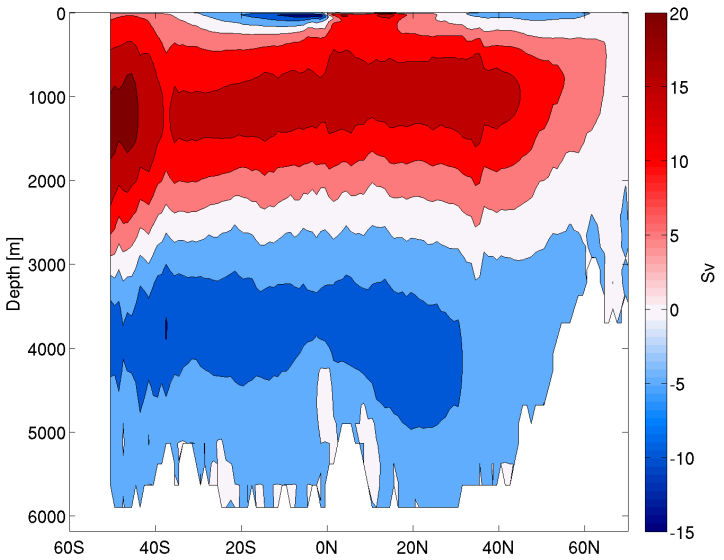

Figure 1.1: Mean meridional overturning streamfunction from the MPI ocean model (STORM project).

$10^6 m^3/s$) far exceeded previous expectations (Longworth and Bryden (2013) and references therein).

The picture of the circulation in the Atlantic became three-dimensional when Henry Stommel in 1957 revolutionized the understanding of the deep circulation (Stommel, 1957). Stommel's theory was based on a simple assumption: The sinking of surface waters in the North Atlantic and the Arctic must be balanced by an upwelling to the ocean's surface. Conservation of potential vorticity then requires that all flow in the basin interior must be northward, which requires the southward transport to be concentrated at the western boundary in a deep western boundary current (Stommel and Arons, 1960). Observations soon confirmed the existence of a southward deep western boundary current (Swallow and Worthington, 1961), setting a unique example of a current that was predicted from theoretical considerations before it was first observed.

In the following years, the so-called Atlantic meridional overturning ciculation

(AMOC) became imbedded in the large-scale global ocean circulation (the ocean conveyor belt), and the picture became more detailed, both through observations and modeling efforts (Richardson, 2008). For practical purposes, the AMOC is nowadays conventionally defined mathematically (e.g. Lozier (2012)): The zonally integrated meridional velocities show an upper cell of poleward flowing waters and a lower cell of southward flowing waters. Cumulatively integrating the velocities from the surface, then integrating zonally yields the overturning streamfunction (Figure 1.1). The AMOC at a specific latitude is defined as the maximum of the overturning streamfunction. In the North Atlantic, this maximum is usually located at a depth of about 1000 m, below which the flow is southward. Note that this zonally averaged, two-dimensional representation of the AMOC does not show that most of flow is concentrated at the western boundary in the northward Gulf Stream and the southward Deep Western Boundary Current (DWBC), and does not make any assumptions about forcing mechanisms.

Historically, buoyancy forcing at high latitudes has been regarded as the main driver of the overturning, but recent studies suggest that wind-forcing might be more important on decadal and shorter timescales (Biastoch et al., 2008). Also, eddy-driven processes have recently received attention, as high spatial resolutions are required to resolve them, but prove to be an important factor for the AMOC's variability (Lozier, 1997, Wunsch, 2008). The established picture of the global ocean conveyor belt therefore likely oversimplifies the system's complexity (Lozier, 2010).

1.2 Climate Impacts

Associated with the AMOC is a northward heat transport of up to 1.3 PW (1PW = 10^{15}W) (Ganachaud and Wunsch, 2003), or up to 25% of the total ocean-atmosphere heat transport in the northern hemisphere (Wunsch, 2005).

This makes the AMOC a key player in the North Atlantic climate system. For example, a short-term intermittent reduction of the AMOC by 30%, as it happened during the winter of 2009/10, led to anomalous snowfall both in central North America and Northwestern Europe (Seager et al., 2010), an increase in tropical hurricane frequency (Bryden et al., 2014) and a record-low of the North Atlantic Oscillation (NAO) in the following winter (Taws et al., 2011).

Lasting changes in the overturning circulation are expected as a response to anthropogenic forcing, due to increased freshwater influx from the melting Greenland Ice Sheet (Gregory et al., 2005). Although a complete shutdown of the AMOC in the near future is no longer considered likely, a decrease of the AMOC is expected over the 21st century (IPCC, 2013), and could imply far-reaching consequences for the climate due to the close relation of the AMOC with sea surface temperatures (e.g. Knight et al. (2005)). Specifically, a slowdown of the AMOC would likely result in a cooling of Europe and North America (Vellinga and Wood, 2002). Other potential consequences include rising of sea levels (Levermann et al., 2005), a southward shift of the intertropical convergence zone in both the Atlantic and the Pacific (Zhang and Delworth, 2005) which would affect rainfall in the equatorial regions (Zhang and Delworth, 2006), a change in the concentration of atmospheric CO_2 (Schmittner et al., 2013), a reduction in productivity of the terrestrial vegetation (Vellinga and Wood, 2002), or a decline in marine biomass and the marine ecosystem (Schmittner, 2005).

For the detection of long-term trends, it is crucial to understand the AMOC's and its components' natural variability. Otherwise, natural multidecadal oscillations might be mistaken for anthropogenically induced lasting changes in the overturning's strength. Also, climate predictions on seasonal to decadal timescales inherently rely on the correct representation of the present-day climate as a starting point. This requires both sustained observational and modeling efforts. Below, I review aspects of the status quo, and identify open

questions.

1.3 Observations of the AMOC

The sixth hydrographic section at 26°N was completed in 2010 (Atkinson et al., 2012). 26°N thus remains one of the best observed regions in the world oceans. The first five hydrographic sections indicated a decrease in the strength of the overturning circulation by 30% over the last 50 years (Bryden et al., 2005). Other observational estimates did not show a downturn, and demonstrated that the choice of level-of-no-motion plays a large role in estimating data from hydrographic sections (Lumpkin and Speer, 2007). Also, the downturn did not continue in the 2010 section. Generally, synoptic hydrographic sections include too many uncertainties due to temporal aliasing for conclusions about long-term behavior (e.g. Kerr (2005)).

Hence, continuous observations of the AMOC are needed. Although this could in principle be done by repeat hydrographic sections (Keller et al., 2007), sustained efforts require a more cost-effective method. In the late 1990s, Marotzke et al. (1999) proposed a method that only requires continuous measurements of temperature and salinity at the eastern and western boundaries to estimate the AMOC. The basic concept behind this idea is the thermal wind balance, which is obtained from combining the frictionless geostrophic momentum equations with the hydrostatic equation (e.g. Olbers et al. (2012)). A consequence of the thermal wind balance is that the geostrophic transport can be inferred from density differences between the western and eastern boundaries (Marotzke et al., 1999).

The RAPID/MOCHA array at 26°N, which went operational in 2004, uses this technique, with moorings at both boundaries of the basin as well as the Mid-Atlantic Ridge to measure the mid-ocean transport (Cunningham et al., 2007). Previous to deployment, the array was tested extensively in numerical

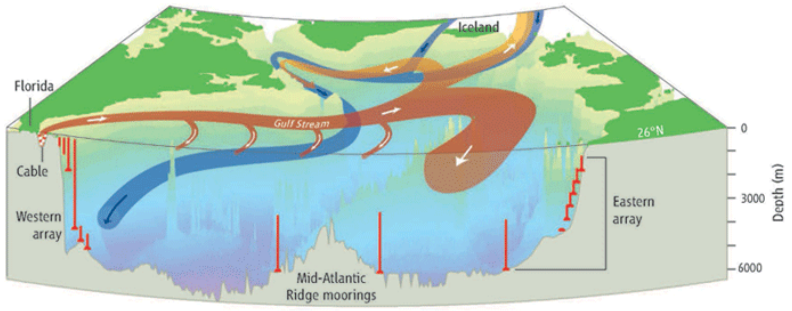

Figure 1.2: Schematic of the RAPID/MOHCHA monitoring array at 26°N, reprinted from Church (2007).

models to ensure that it indeed captures the mean and temporal variability of the AMOC (Hirschi et al., 2003, Baehr et al., 2004). Aside from its historical significance, 26°N was chosen because of its unique geographical setup (Figure 1.2): At 26°N, the northward Florida Current is separated from the basin by the Bahamas, and the DWBC is closely spaced. For these reasons, the configuration used at 26°N cannot easily be implemented at other latitudes (Baehr et al., 2004). For an estimate of the full AMOC at 26°N, the mid-ocean transport is combined with cable voltage measurements of the Gulf Stream in the Florida Straits (Meinen et al., 2010) and an estimate of the wind-induced Ekman transport, computed from satellite-based wind stress reanalyses.

Data of the first year of the RAPID/MOCHA array showed large seasonal and sub-seasonal variability, with the total AMOC transport ranging from 4 to 35 Sv with a mean of about 19 Sv (Cunningham et al., 2007). Subsequent years of observations found a robust seasonal cycle (Kanzow et al., 2010), but the winter 2009/10 marked an unforeseen, large downturn of the circulation (McCarthy et al., 2012). Although the AMOC recovered quickly in the summer of 2010, the first eight years of the time series showed a gradual weakening of the AMOC (Smeed et al., 2014). It is not clear whether this weakening is part of a multi-year oscillation, or a longterm trend, as timescales of decades are expected to be required to detect changes induced by anthropogenic forcing (Baehr et al., 2009), and the AMOC is expected to weaken over the next decade

due to natural variability (Keenlyside et al., 2008).

The unexpected magnitude of intra-seasonal variability confirms that hydrographic sections are an inadequate method for estimating decadal changes in the AMOC, since temporal aliasing will mask any long-term trend (Kanzow et al., 2010). This applies especially to the upper ocean, where seasonal and sub-seasonal variability are high. Indeed, after correcting the estimates from the six hydrographic sections at 26°N for seasonal variability (computed from the first five years of the RAPID/MOCHA array), the data no longer show a decrease in AMOC strength (Atkinson et al., 2010). Still, the hydrographic sections provide valuable information on the temporal evolution of the deep ocean, where the influence of seasonal variability is reduced. The six hydrographic sections show a change in deep water transports over the 50 years of observations (Atkinson et al., 2010).

At 41°N, a very different technique is used to continuously estimate the AMOC (Willis, 2010): Here, the transports are estimated from data gathered by Argo floats and altimetry.

The Argo project (www.argo.net) currently has over 3500 floats in the global ocean, which operate autonomously. They surface every ten days to transmit their position and a temperature and salinity profile via satellite. In this way, the Argo floats provide an unprecedented number of hydrographic data as well as observations of time-averaged velocity. They operate year-round and are uniformly distributed, unlike previous data sets which depended on shipping routes.

To obtain an estimate of the geostrophic transport at 41°N, the density field is computed from temperature and salinity, and the float positions over time are used to estimate the dynamic height. Because of the close relation of sea surface height with the subsurface circulation, variations in sea surface height obtained from altimeter data help to reduce the sampling error (Willis and Fu, 2008, Willis, 2010). The geostrophic transport is then combined with the

Ekman transport to estimate the AMOC at 41°N (Willis, 2010).

Like the 26°N setup, the technique used at 41°N cannot readily be employed at any latitude: As the Argo floats dive to about 2000 m to gather temperature and salinity data, they cannot operate in shallower regions. Thus, at latitudes where a significant part of the circulation sits on the continental shelf, which is the case for the Gulf Stream at many latitudes, the Argo floats would miss part of the northward circulation, and therefore the technique used to estimte the AMOC at 41°N would underestimate the northward transport (Willis, 2010).

The estimated AMOC at 41°N shows a clear seasonal cycle. The seasonal range and time-mean of the AMOC at 41°N are reduced compared to 26°N (Willis, 2010).

The meridional heat transport is also estimated at both 26°N and 41°N, although it is more challenging to monitor than the mass transport, since the temperature field is needed in addition to the velocity field. At both 26°N and 41°N, there is a close correspondence between observed mass and heat transports (Hobbs and Willis, 2012, Msadek et al., 2013).

1.4 Latitudinal dependence

Although the observational estimates at 26°N and 41°N allow unprecedented insights in the temporal variability of the AMOC, it is not clear if they represent the AMOC variability throughout the entire Atlantic. Knowledge whether the observed AMOC at one latitude is representative of the AMOC variability at other latitudes might therefore greatly enhance the scope of the already available and of future observational time series: Plans are underway for monitoring arrays in the subpolar North Atlantic (www.o-snap.org) and another array is already operating in the South Atlantic (Meinen et al., 2013b).

The latitudinal dependence of the AMOC has been investigated in a number of model studies. In an early study, Bryan (1982) found a latitude dependence in the seasonality of the meridional heat transport. In more recent studies, Böning et al. (2006) and Biastoch et al. (2008) find coherent signals of subpolar origin in the decadal AMOC variability in both the subtropical and the subpolar gyre, although they are obscured by high-frequency wind-driven variability in the subtropics (Jayne and Marotzke, 2001, Böning et al., 2006). In contrast, Zhang (2010) finds that anomalies propagate with advection speed, resulting in a lag of several years between subpolar and subtropical variability. On shorter timescales, Balan Sarojini et al. (2011) find coherence over several latitudes, but not across the whole North Atlantic. Thus, it is to date not clear how the observed AMOC variability is related to the AMOC variability at other latitudes.

The newly available AMOC observations at 26°N and 41°N offer the opportunity to jointly analyse two observed time series, and address the question

- Are AMOC observations at one latitude representative of the AMOC variability at other latitudes?

1.5 Deep water formation and export

Monitoring the deep water formation and export is another option for expanding the observational data base of variability in the North Atlantic. Although other forcing mechanisms have received attention during the past years, buoyancy fluxes remain a key feature of the Atlantic meridional overturning circulation.

At specific places in the world oceans, namely in the North Atlantic in the Greenland Sea, the Labrador Sea (Figure 1.3a) and the north-western Mediterranean Sea; and in the Southern Ocean in the Weddell and Ross Seas, surface

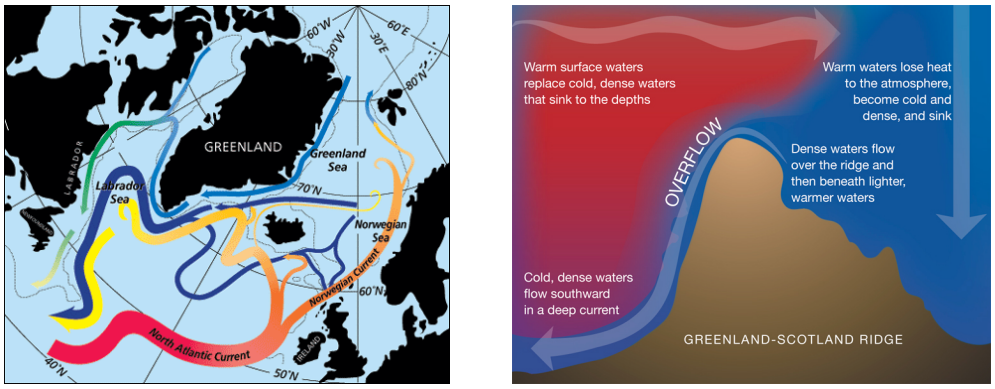

Figure 1.3: a) Map of the subpolar North Atlantic and the pathways of warm and cold waters. b) Schematic of the overflow over the Greenland-Scotland Ridge. Both figures were retrieved from http://www.whoi.edu/oceanus/illustrations.

waters can in winter become denser than the waters below and sink in a process called open ocean convection. Open ocean convection requires very specific conditions, including favorable atmospheric forcing and a weak stratification (Marshall and Schott, 1999). There is no open ocean convection in the Pacific Ocean, as the Pacific Ocean is fresher than the Atlantic and surface waters thus do not become dense enough to sink. Convection activity in the North Atlantic has been linked to a number of climate variables, including the North Atlantic Oscillation, and varies on decadal timescales, both in the Greenland and the Labrador Sea (Dickson et al., 1996, Yashayaev, 2007).

As the north-western Mediterranean Sea is globally the least important convection site (albeit the best observed) I will focus on convection in the Labrador and Greenland Seas. In the Greenland Sea, convection typically occurs in March after a deepening of the mixed layer over the previous months (Marshall and Schott, 1999). Deep waters from the Greenland Sea partially flow over the Greenland-Scotland Ridge, and enter the subpolar North Atlantic. Depending on their point of entry, these water masses are termed either Iceland-Scotland Overflow Water (leaving the Greenland Sea between Iceland and Scotland, Figure 1.3b) or Denmark Straits Overflow Water (leaving the Greenland Sea via the Denmark Strait). Combined, the Nordic Seas overflow waters account for two thirds of the volume transport in the lower limb of the AMOC (Quadfasel

and Käse, 2013).

After entering the subpolar North Atlantic, the Iceland-Scotland Overflow Water and the Denmark Straits Overflow Water flow into the Labrador Sea in a western boundary current. As a result of an increase or decrease in convection intensity conditions in the Labrador Sea have been shown to change (Yashayaev, 2007), but the Labrador Sea Water, which forms by deep convection in the Labrador Sea, is always fresher and colder than the western boundary current. Through eddy-driven property exchange, the boundary current takes up Labrador Sea Water on its way around the basin (Straneo 2006). This results in a colder, fresher and stronger deep boundary current at the exit of the Labrador Sea. Together, the three water masses (Labrador Sea Water, Iceland-Scotland Overflow Water and Denmark Straits Overflow Water) form the North Atlantic Deep Water.

1.6 The Deep Western Boundary Current

The North Atlantic Deep Water can be traced until the Southern Ocean by its physical and chemical properties. In contrast to Stommel's model of the deep circulation, the DWBC is no longer considered the sole pathway for its export from the higher latitudes. Studies with different types of floats released in the central Labrador Sea show that only few floats reach the subtropics via the DWBC (Fischer and Schott, 2002, Bower et al., 2009). Instead, they travel via the basin interior. They do however tend to stay in the western part of the basin, west of the Mid-Atlantic Ridge. The importance of interior pathways for the export of deep waters from the higher latitudes has also been demonstrated in tracer (e.g. Rhein et al. (2002)) and model studies (Gary et al., 2011, 2012).

Subpolar anomalies propagate southward in the DWBC through fast coastally trapped waves and eventually through advection (Johnson and Marshall, 2002,

Zhang, 2010, Elipot et al., 2013). While the DWBC is not the only export pathway for deep waters, it is still expected to be the fastest, with a transit time of ten years for Labrador Sea Water from 53°N to 26°N (Molinari et al., 1998), and might thus be best suited for the detection of changes in deep water formation at the subtropical latitudes.

As in the case of the AMOC, the long-term variability of the DWBC can only be estimated from hydrographic sections. Both Bacon (1998) and Kieke and Rhein (2006) report decadal variability in the DWBC from an analysis of hydrographic sections in the western subpolar North Atlantic. But again the interpretation of results is however complicated by the sparse temporal sampling (Kieke and Rhein, 2006).

Continuous observations of the DWBC currently exist at 26°N as part of the RAPID/MOCHA array, at Line W at about 38°N (Toole et al., 2011), at 53°N in the Labrador Sea (Dengler et al., 2006, Fischer et al., 2014a) and in the Denmark Straits (Jochumsen et al., 2012). At 26°N, Line W and 53°N, the time series exhibit energetic high-frequency variability, complicating the detection of long-term changes. The short-term variability is weaker in the Denmark Straits, but does, to date, not show a significant trend (Jochumsen et al., 2012). At the higher latitudes, the DWBC variability has been linked to convection events, but further south, high-frequency eddy variability and other local processes might obscure the link between DWBC variability and convection activity (Peña-Molino et al., 2012). In my thesis, I will therefore address the question

- Can changes in convection activity be observed in the subtropical DWBC?

Like the DWBC, the higher-latitude AMOC is related to convection activity, but it is not clear if the propagation to lower latitudes is instantaneous (Böning

et al., 2006, Biastoch et al., 2008) or occurs at a lag of several years (Zhang, 2010). Influences from local wind forcing further complicate the relation (Jayne and Marotzke, 2001, Böning et al., 2006).

Observations of the DWBC at 26°N and Line W show that the mean transport and variability of the DWBC far exceed the observed AMOC at 26°N and 41°N (Johns et al., 2008, Toole et al., 2011, Meinen et al., 2013a). This high-frequency variability in the DWBC has been linked to recirculations outside the range of moorings (Johns et al., 2008), local processes in the western basin and deep transports in the eastern part of the basin (Meinen et al., 2013a), or baroclinic Rossby waves (Kanzow et al., 2008), but a definite explanation has not been put forward. Also, longer timescales cannot be investigated with the available observations. The question

- Can observations of the DWBC be used as a proxy for AMOC observations?

therefore remains open.

1.7 Methods of the thesis

The overall aim of this thesis is to contribute to the understanding of the variability of the AMOC and its deep western return flow, the DWBC, by using both the available observational time series at 26°N, Line W (about 38°N) and 41°N and results from a high-resolution, wind-forced general ocean model.

The thesis is motivated by the importance of the AMOC for the climate system, the need to understand its inherent natural variability and the lack of observational data. The unexpected downturn of the AMOC in 2009/10 demonstrated

that knowledge of the seasonal cycle may not be sufficient to predict the next year's variability. Observations at 26°N and 41°N might not be representative of the AMOC variability at other latitudes. Also, it is currently not possible to infer the AMOC variability over the last half-century from direct observations, as hydrographic sections – the only long-term records of the AMOC's strength – have proven to be inadequate.

To understand the possibilities for a broader use of available observations and the underlying mechanisms of variability, especially away from the deep water formations, I investigate the following research questions:

1. Are AMOC observations at one latitude representative of the AMOC variability at other latitudes?
2. Can changes in convection activity be observed in the subtropical DWBC?
3. Can observations of the DWBC be used as a proxy for AMOC observations?

With these questions in mind, I analyse the newly available observational time series at 26°N, Line W and 41°N. For longer timescales and the question of latitudinal coherence throughout the North Atlantic, I complement the analysis with results from a wind-forced ocean general circulation model. Specifically, I use a high-resolution run with the Max-Planck-Institute ocean model (Marsland et al. (2003), Jungclaus et al. (2006), von Storch et al. (2012), Figure 1.4).

1.8 Outline of the thesis

Each chapter of the thesis is written in the form of a journal publication, with its own abstract, introduction and conclusions.

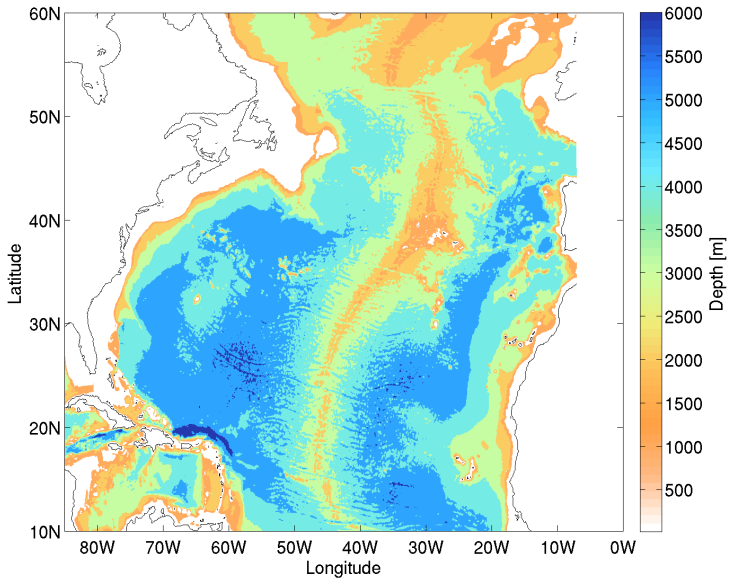

Figure 1.4: Bathymetry of the North Atlantic ocean in the MPI ocean model (STORM project).

In Chapter 2, I jointly analyse the recently available observational AMOC time series at 26°N and 41°N, and compare them to results from the high-resolution ocean model described above. The aim of this chapter is to understand the seasonal coherence of the observed and modeled AMOC between 26°N and 41°N. I also discuss how well the model reproduces the observed AMOC variability. Due to the shortness of the observational time series the analysis mainly focuses on seasonal timescales, although interannual time scales are investigated as well. The chapter has been published in *Geophysical Research Letters* (Mielke et al., 2013).

As a follow-up to Chapter 2, in Chapter 3, I investigate the seasonal variability of the meridional heat transport, which is more directly linked to climate variations than the mass transport. I also investigate the relation of the AMOC and the meridional heat transport in both model and observations. The purpose of this chapter is to evaluate differences between heat and mass transport and identify open questions and possible future steps.

In Chapter 4, I investigate the seasonal variability of the DWBC in model and observations. To this end, I first define the model DWBC in density classes after a comparison of modeled and observed temperature and salinity data, and after a careful analysis of the time-varying velocity fields to define the zonal extent of the DWBC. After a comparison of the mean, structure and temporal variability of the observed DWBC, I investigate the seasonality of the DWBC and its forcing mechanisms. Finally, the relation between the DWBC and AMOC seasonality is investigated. The chapter has been submitted to *Journal of Geophysical Research: Oceans*.

In Chapter 5, I again use the definition of the DWBC established in Chapter 4 to investigate the variability of the DWBC on decadal timescales. The focus of this chapter is on the relation of the DWBC and the basin-wide transport, i.e. the AMOC, on decadal timescales.

Together, Chapters 4 and 5 address the question whether changes in deep water formation at the higher latitudes are reflected in the subtropical DWBC, and whether the AMOC can be inferred from the DWBC on seasonal to decadal timescales.

Overall conclusions and implications are presented in Chapter 6.

2 Observed and simulated variability of the AMOC at 26°N and 41°N[1]

Abstract

Time series of the observational estimate of the Atlantic meridional overturning circulation (AMOC) have recently become available, but so far no contemporaneous relation has been documented between them. Here, we analyze the variability of the 26°N RAPID and the 41°N ARGO-based AMOC estimates on seasonal timescales, and we compare them to a simulation from a high-resolution NCEP-forced ocean model. In our analysis of the observed time series, we find that the seasonal cycles of the non-Ekman component of the AMOC between 26°N and 41°N are 180-degrees out-of-phase. Removing the mean seasonal cycle from each time series, the residuals have a non-stationary covariability. Our results demonstrate that the AMOC is meridionally covariable between 26°N and 41°N at seasonal timescales. We find the same covariability in the model, though the phasing differs from the observed phasing. This may offer the possibility of inferring AMOC variations and associated

[1]C. Mielke, E. Frajka-Williams, and J. Baehr (2013), Observed and simulated variability of the AMOC at 26°N and 41°N, *Geophysical Research Letters*, **40**, 1159-1164.

climate anomalies throughout the North Atlantic from discontinuous observations.

2.1 Introduction

With a northward heat transport of up to 1.3 PW (Ganachaud and Wunsch, 2003), the Atlantic meridional overturning circulation (AMOC) is one of the prominent components of today's climate and has a strong influence on the climate of North America and Europe (e.g., (Sutton and Hodson, 2005)). Seasonal AMOC variations impact the seasonal heat storage and sea surface temperature in the North Atlantic, which affects climate phenomena such as North Atlantic hurricane activity (Zhang and Delworth, 2006) and the North Atlantic Oscillation (NAO) (Taws et al., 2011). The AMOC variability has been the subject of many, mostly model-based studies over the years, whether at a single location (Böning et al., 2001, Baehr et al., 2009) or across several latitudes (Bryan, 1982, Balan Sarojini et al., 2011, Munoz et al., 2011). It has been suggested that the AMOC variability might be gyre-specific, with higher variability in the subtropical gyre (Bingham et al., 2007, Lozier et al., 2010), but coherence across the gyres has so far not been identified on seasonal timescales.

Continuous AMOC estimates are at present restricted to two latitudes (26 °N and 41 °N, (Cunningham et al., 2007, Willis, 2010), and they have only recently become available. Therefore, a joint analysis of two observed, albeit short, AMOC time series is now possible for the first time. In agreement with the studies mentioned above, no relation has yet been documented between these two time series.

Here, we analyze the seasonal to interannual variability of the AMOC transport time series at 26°N and 41°N from both observations and a numerical model. As the underlying mechanisms will be subject of research for many

years to come, the scope of the present study is to describe and compare the meridional covariability of the seasonal and interannual variability in the model and observations as a reference for further investigations.

2.2 Description of observations, model and methods

Observations at 26°N are from the RAPID/MOCHA array (Cunningham et al., 2007). The array was tested in numerical models to ensure that it can indeed capture the mean and short-term variability of the overturning (Hirschi et al., 2003, Baehr et al., 2004). Data are available at daily resolution from April 2004 to December 2010 and have so far been the subject of several studies (e.g., (Kanzow et al., 2007, 2010, Rayner et al., 2011, McCarthy et al., 2012)). The AMOC transport is calculated as the sum of Florida Straits transport, Ekman transport and upper mid-ocean transport derived from moorings placed across 26°N. The Ekman transport is calculated from the ERA-Interim wind product (Dee et al., 2011), but no significant differences are found if NCEP reanalysis data (Kalnay et al., 1996) are used (Figure S1). Here, we use monthly mean data, smoothed by a three-month moving average.

The AMOC estimates at 41°N are from Willis (2010) and are computed using Argo floats and altimeter data. Data are available as three-month running means, from January 2002 to September 2010. The Ekman transport is computed from NCEP reanalysis data (Kalnay et al., 1996).

The reader should be aware that although both time series will be treated equally in the following analysis, there are fundamental differences between the two estimates: At 26°N, the AMOC is calculated as the maximum of the overturning circulation, using profiles of density at the eastern and western boundary and the Mid-Atlantic Ridge and applying a compensation veloc-

ity by assuming zero net transport (Kanzow et al., 2007, 2010). At 41°N, a monthly time series of density from the surface to 2000m is derived from Argo data, referencing the geostrophic shear using a level of known motion from the mapped Argo parking depth velocities and altimetry (Willis and Fu, 2008). The AMOC is then calculateed by integrating from the surface to 1130m, the average depth of no motion at 41°N (Willis, 2010).

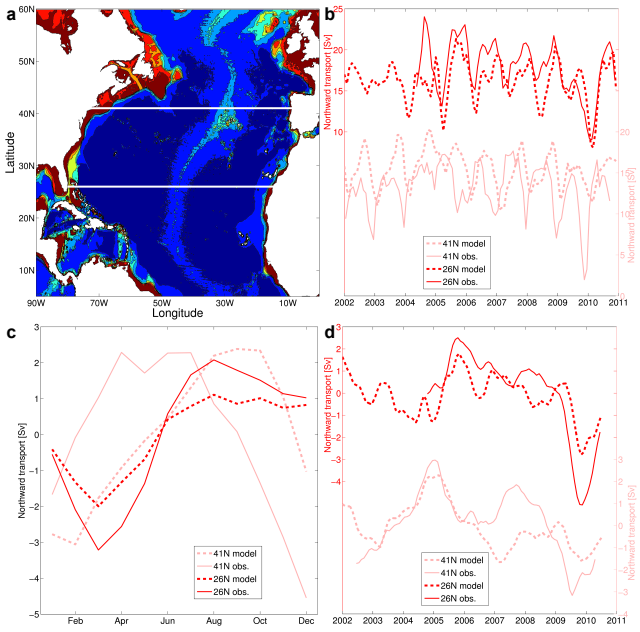

Figure 2.1: a) Bathymetry of the North Atlantic ocean in the Max-Planck-Institute (MPI) ocean model (STORM project) after interpolation and latitudes of interest, b) observed (solid) and model (dashed) AMOC annual cycle at 26°N (dark) and 41°N (light), c) AMOC time series, d) AMOC time series with seasonal cycle removed.

The model output stems from a high resolution ocean model simulation with the MPI ocean model (Jungclaus et al., 2006, Marsland et al., 2003) in a setup with a horizontal resolution of 0.1° and 80 vertical levels ($10 - 280$ m thickness, Figure 1a). The simulation is forced by 6−hourly NCEP reanalysis data, and covers the time period 1948–2010 (von Storch et al. (2012), Section 2.6.1). Here, we focus on the period that overlaps with the 41°N observations (2002−2010). The overturning streamfunction is directly calculated from the velocities in the model, and the AMOC is defined as the vertical maximum of

the streamfunction. The Ekman transport is calculated from the zonal wind stress compontent τ_x as $\psi_{Ekman} = -\int \frac{\tau_x}{\rho f} dx$, where ρ is the density and f is the Coriolis parameter. The model output is smoothed to three-month running means for comparison with the observations.

For both latitudes, we calculate the wind stress curl from NCEP reanalysis data (Kalnay et al., 1996), which we refer to as the observed wind stress curl. For the model, a wind stress curl is calculated from the output wind stress fields between 15°N and 50°N. In both cases, the Sverdrup transport is calculated as the zonal integral of the wind stress curl, following standard theory: $\psi_{Sverdrup} = \int \frac{curl_z \tau}{\beta} dx$, where β is the rate of change of the Coriolis parameter with latitude. In the following, we will not distinguish between observed and modelled Sverdrup transport, as they are not substantially different because the NCEP data are used to force the model run. For completeness, both curves are displayed in the figures.

2.3 Latitudinal covariability at seasonal timescales

At 26°N, the observed AMOC transport has a time-mean value of 18 Sv (1 Sv = 10^6 m^3s^{-1}, for exact values and standard deviations for all transports, see Table 2.1, all values are calculated from the smoothed time series). At 41°N, the observed AMOC has a smaller time-mean value (about 13 Sv), but a higher standard deviation than at 26°N. However, we find no obvious contemporaneous relation between the observed AMOC estimates at these latitudes (Figure 1b), although—given the shortness of the available time series—lead-lag relationships on longer timescales cannot be excluded. The observed AMOC seasonal cycle (Figure 1c) at 26°N agrees well with the seasonal cycle computed by Kanzow et al. (2010) using only data from 2004−2008.

		MOC	Ekman	AMOC–Ekman	Sverdrup
26°N	obs.	17.9 ± 3.2 (5.3)	3.5 ± 1.5 (3.0)	15.1 ± 2.1 (2.8)	-25.3 ± 6.5 (8.6)
	model	16.4 ± 2.5 (3.1)	3.7 ± 1.4 (1.7)	12.6 ± 1.7 (2.0)	-19.8 ± 6.7 (9.1)
41°N	obs.	13.2 ± 3.0 (6.8)	-2.6 ± 1.7 (3.6)	15.8 ± 2.1 (4.3)	-6.0 ± 17.0 (11.1)
	model	15.2 ± 2.4 (5.4)	-2.3 ± 1.7 (3.7)	17.8 ± 1.2 (2.4)	-0.3 ± 10.2 (7.8)

Table 2.1: Mean values, standard deviations and seasonal range in parentheses for the transports discussed in this paper (all values are in Sv).

To analyze the seasonal to interannual variability, we subtract the Ekman transport (Figure S2) from the observed AMOC time series (we will refer to this quantity as AMOC−Ekman). This removes short-term variability and leaves the internal, non-Ekman part of the circulation, which dominates the northward heat transport (Johns et al., 2011). There is northward Ekman transport at 26°N, so removing the Ekman transport from the observed AMOC decreases the time-mean value to about 15 Sv. At 41°N, the Ekman transport is southward, and the observed AMOC−Ekman has a time-mean value of almost 16 Sv.

In the observations, we generally find an inverse phasing between AMOC−Ekman at 26°N and 41°N (Figure 2a). One exception is the winter of 2009/10, where AMOC−Ekman is in phase between the two latitudes. In contrast, the modelled AMOC−Ekman has a positive correlation between the two latitudes (Figure 2a).

The Sverdrup transport is inversely phased between 26°N and 41°N (Figure 2b). Directly comparing model and observations reveals a statistically significant positive correlation between observations and model for AMOC−Ekman at 26°N (correlation coefficient: 0.44, $p < 0.01$), but not at 41°N. Subtracting the Ekman transport from the Sverdrup transport does not influence our

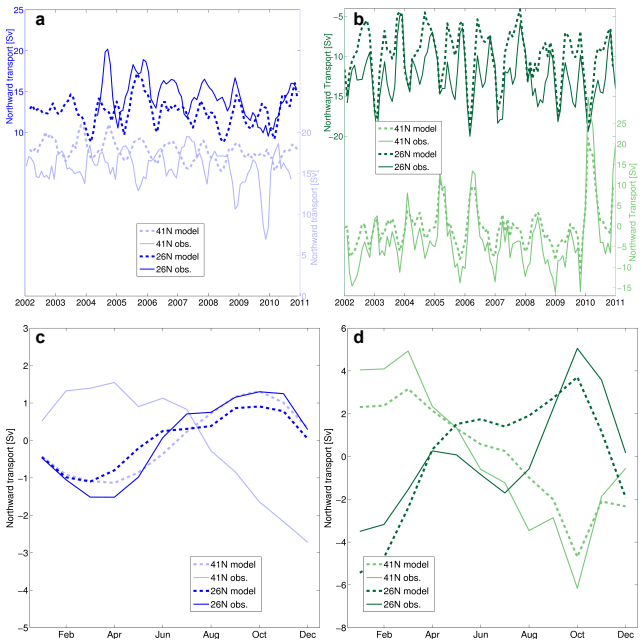

Figure 2.2: time series and mean annual cycle anomalies of observed (solid) and model (dashed) AMOC−Ekman and Sverdrup transport at 26°N (dark) and 41°N (light): a) AMOC−Ekman time series, b) Sverdrup transport time series, c) AMOC−Ekman annual cycle anomalies, d) Sverdrup transport annual cycle anomalies.

results.

The AMOC−Ekman and Sverdrup transport time series are dominated by the seasonal cycle (Figure 2c,d, see Table 2.1 for the seasonal range) in all cases. Although the available observed time series are only 5.5 years at 26°N and 8.5 years at 41°N, we compute the mean seasonal cycles from the observations. Similarly, we compute the mean seasonal cycles from the model for the period that overlaps with the 41°N observations. The seasonal cycle computed for the period that overlaps with the 26°N observations is not significantly different (Figure S4). We choose to use the same time period for both modelled latitudes to allow for a direct comparison. At 26°N, the AMOC−Ekman seasonal cycle has a maximum in autumn and a minimum in spring in both model and observations. At 41°N, the model AMOC−Ekman seasonal cycle also has a maximum in autumn and a minimum in spring, but the observed AMOC−Ekman seasonal cycle has a maximum in spring and a minimum in

autumn.

Model and observations agree on the AMOC−Ekman seasonal cycle at 26°N, but at 41°N, AMOC−Ekman shows an inverse phasing between model and observations. The Sverdrup transport seasonal cycle agrees with the observed AMOC−Ekman seasonal cycle at both latitudes: At 26°N, the maximum occurs in autumn and the minimum occurs in spring, while at 41°N the maximum occurs in autumn. The seasonal cycle agrees for all transports between model and observations for 26°N, but only for the Sverdrup transport for 41°N.

The seasonal cycle for AMOC−Ekman emerges clearly from the noise in both model and observations, but results for the Sverdrup transport should be treated with caution, as the amplitude is not as robust as for AMOC−Ekman (Figure S3). For the model, time series for all transports are available starting in 1948, and we find that the seasonal cycles computed with only the period that overlaps with the 41°N observations does not differ significantly from the model seasonal cycles since 1948. The Sverdrup transport seasonal cycle agrees well with the findings by Atkinson et al. (2010), although they use a longer time series (1980−2007).

In the model, we can also analyze the seasonal cycle of all transports at latitudes between 26°N and 41°N. AMOC−Ekman (Figure 3a) is in phase across all latitudes north of about 23°N. For the Sverdrup transport (Figure 3b), there is an inversion of the seasonal cycle at about 35°N: north of 35°N, the seasonal cycle shows a maximum in spring, while south of 35°N, the maximum transport occurs in autumn. This is due to changes in the meridional wind stress at the eastern boundary north of 35°N and is therefore not apparent in the Ekman transport seasonal cycle (Figure 3c). The AMOC seasonal variability (Figure 3d) is dominated by the Ekman transport. As a consequence, the AMOC−Ekman seasonal cycle has a smaller amplitude than the AMOC seasonal cycle at all latitudes, and the maximum transport occurs later in the year for AMOC−Ekman at each latitude. Figure 3 also demonstrates that the

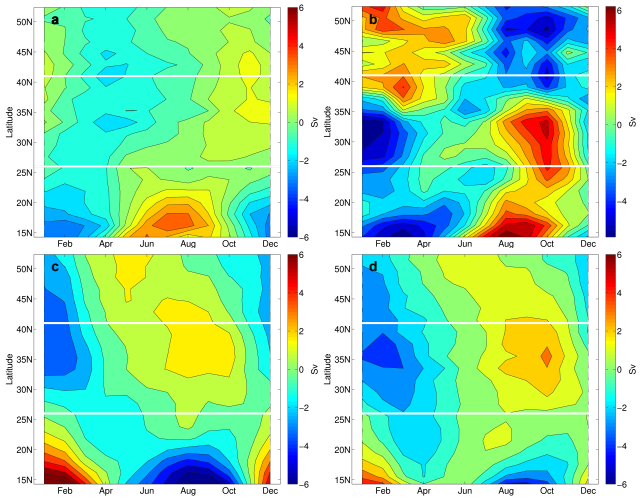

Figure 2.3: Hovmoeller plots of the mean annual cycle anomalies of AMOC and transport components calculated from the STORM run: a) AMOC−Ekman, b) Sverdrup transport, c) Ekman transport, d) AMOC.

exact choice of latitude (e.g., 41°N ± 5°) is not important in the model.

2.4 Latitudinal dependence at interannual timescales

We remove the seasonal cycle from all time series and apply an 11-month running mean to remove the remaining seasonality from the time series (Figures and 1d and 4). There is no clear relation between the two latitudes for the Sverdrup transport. In the observations, we find an inverse phasing between 26°N and 41°N for 2005–2008 for AMOC−Ekman. But in 2009–2010, there is agreement for AMOC−Ekman between the latitudes. In contrast to the observations, there appears to be no relation between the two latitudes for the modelled AMOC−Ekman time series.

The winter of 2009/10 stands out in the anomaly time series, with a pronounced minimum in AMOC and Ekman transport at both latitudes in both

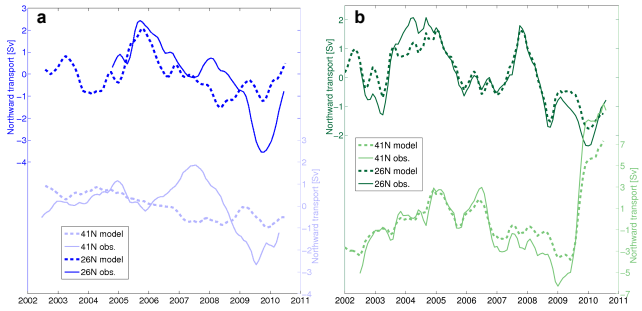

Figure 2.4: Interannual variability in the observed (solid) and model (dashed) time series of AMOC−Ekman and Sverdrup transport at 26°N (dark) and 41°N (light) with annual cycle removed, smoothed by a 11-month running mean: a) AMOC−Ekman, b) Sverdrup transport.

model and observations (least prominent in the Ekman transport at 41°N). This is likely caused by an extreme negative NAO index in that winter (Jung et al., 2011). The minimum occurs in autumn at 41°N and in the beginning of 2010 at 26°N in both model and observations. At both latitudes, the AMOC minimum is a little earlier in the observations than in the model, and we observe a pronounced minimum of AMOC−Ekman in autumn, which is not apparent in the model. The Sverdrup transport at 26°N shows no anomaly, while there is a prominent maximum at 41°N in both model and observations.

2.5 Summary and Conclusions

In the observations, we find opposing annual cycles for AMOC−Ekman at the two investigated latitudes: At 26°N, AMOC−Ekman has a maximum in autumn and a minimum in spring, at 41°N the maximum occurs in spring and the minimum occurs in autumn. The same inverse phasing is also apparent in the Sverdrup annual cycle. By contrast, we find the same seasonality for the modelled AMOC−Ekman at 26°N and 41°N, with a maximum in autumn and a minimum in spring.

It is, at this point, unclear why model and observations agree on

AMOC−Ekman at 26°N, but not at 41°N. In their comparison of several ocean reanalyses, Munoz et al. (2011) find similar seasonal cycles for the AMOC, and further studies using oceanic state estimates or further models might also be able to shed light on this issue. In addition, AMOC observations at different latitudes, especially between 26°N and 41°N, will be useful in determining the reasons for the inverse phasing of AMOC−Ekman at 26°N and 41°N, and whether it is gyre-specific or switches phase as does the Sverdrup transport. Tests of the 41°N observing system in high-resolution models, as have been done extensively for the RAPID array (Hirschi et al., 2003, Baehr et al., 2004), might shed further light on the discrepancies between model and observations. Understanding these discrepancies in the simulation of the seasonal cycle will be crucial as medium-term climate predictions inherently rely on the meaningful predictions of modulations of the seasonal cycle.

While further studies are required, our results suggest that the non-Ekman part of the AMOC and its seasonal cycle is meridionally covariable on seasonal and interannual timescales. The AMOC's covariability on seasonal timescales has not been the subject of many studies to date, but coherence on interannual timescales has been identified in model analyses (Balan Sarojini et al., 2011, Bingham et al., 2007). Both of these studies find correlation lengths that are in line with our results. Longer observational time series are needed to identify possible lead-lag relationships on timescales longer than interannual.

An implication of this is the possibility of capturing seasonal AMOC variability throughout the North Atlantic away from the specific latitude of measurements. Specifically, the 26°N observations might be used for inferring the seasonal AMOC variability at mid-latitudes, where it is relevant for the climate of Western Europe. Our findings also offer the prospect of investigating seasonal heat storage and ocean convergence and divergence, and thus further our understanding of the relationship of the AMOC with sea surface temperature and climate indices such as the NAO.

2.6 Supplementary material

The following information was published as supplementary material with Mielke et al. (2013), and contains details about the model experiment, as well as four supplementary figures that illustrate points made in the made text.

2.6.1 Further details of the model setup

The model output stems from a high resolution ocean model simulation with the Max-Planck Institute Ocean model (MPI-OM). The bipolar grid from previous MPI-OM versions has been replaced by a tripolar grid that is Mercator south of the equator (von Storch et al., 2012), but the underlying physics equation are the unchanged (Marsland et al., 2003, von Storch et al., 2012). The downward shortwave flux, the precipitation and the windstress are taken directly from the NCEP reanalysis. The sensible, upward shortwave, upward and downward longwave fluxes, as well as the latent heat flux and the conductive heat flux through sea ice are calculated using the bulk formulae described in (Marsland et al., 2003). Sea surface salinity is relaxed to the Polar science center Hydrographic Climatology [Steele et al, 2001]. Deep water formation in the North Atlantic takes place in the central Labrador Sea and the Nordic seas; and open ocean convection in the Wedell Sea. The AMOC maximum is located at about 35°N and 1000 m depth.

2.6.2 Auxiliary figures

The auxiliary figures show a comparison of AMOC time series calculated with ERA-Interim and NCEP reanalysis data (Figure S1), the Ekman transport time series and seasonal cycle (Figure S2), the representativeness of the AMOC, AMOC−Ekman and Sverdrup transport seasonal cycles (Figure S3)

and the mean annual cycle anomalies for the period overlapping with the RAPID observations (Figure S4).

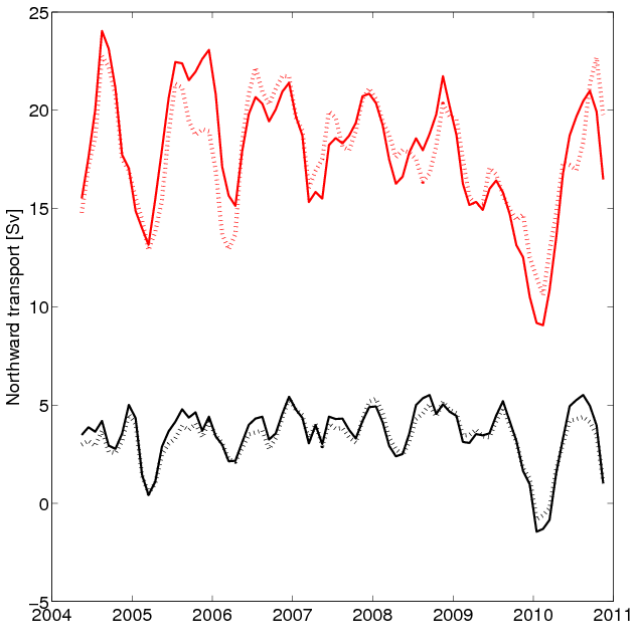

Figure S1: MOC (red) and Ekman (black) transport time series calculated using ERA-Interim (solid) and NCEP (dotted) reanalysis data.

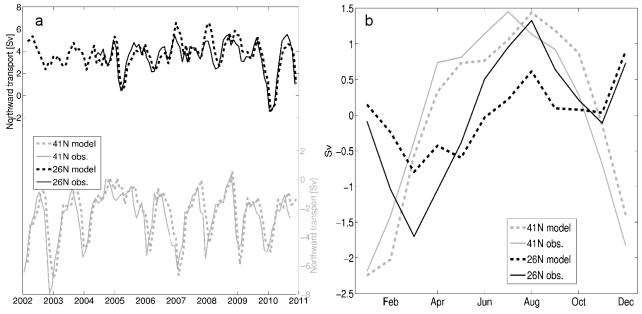

Figure S2: Observed (solid) and model (dashed) Ekman transport: a) time series, b) seasonal cycle anomalies.

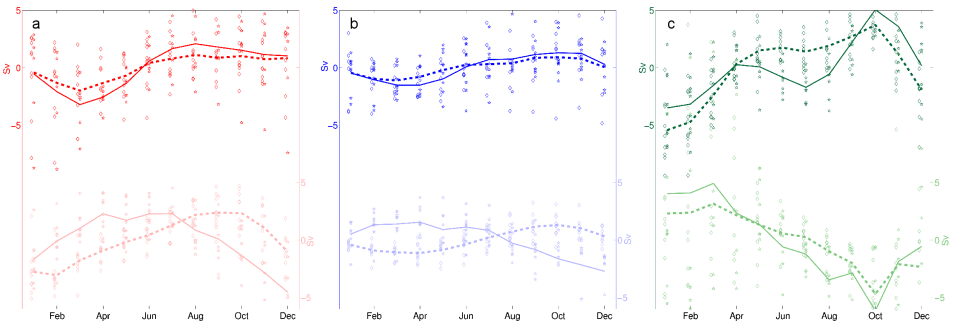

Figure S3: Mean annual cycle anomalies and individual values of observed (solid and stars) and model (dashed and diamonds) AMOC and transport components at 26N (dark) and 41N (light): a) AMOC, b) AMOC−Ekman, c) Sverdrup transport.

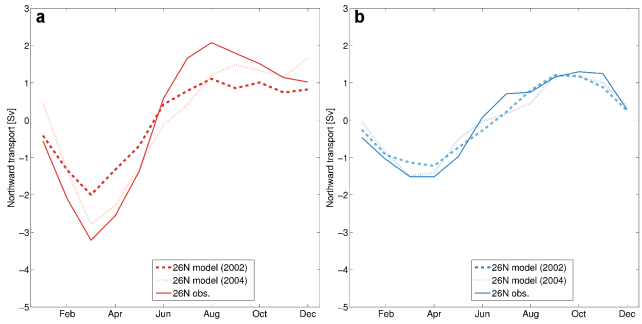

Figure S4: Mean annual cycle anomalies for the model periods 2004–2010 and 2002–2010 and the observations at 26N: a) AMOC, b) AMOC−Ekman.

Acknowledgements

We thank Stuart Cunningham, Shane Elipot, Stefan Gary and Jochem Marotzke for helpful discussions. We thank the two reviewers for constructive comments in the review process of the manuscript, and Irina Fast and Helmuth Haak for their help with the model output and the interpolation. We also thank Josh Willis and Will Hobbs for providing the 41°N data. Data from the RAPID-WATCH/MOCHA monitoring project are funded by the Natural Environment Research Council (NERC) and National Science Foundation (NSF) and are freely available from www.noc.soton.ac.uk/rapidmoc. Florida Current transports estimates are funded by the National Oceanic and Atmospheric Administration (NOAA), and are available from www.aoml.noaa.gov/phod/floridacurrent. The STORM/NCEP simulation is part of the German STORM consortium project and has received financial support from the

Institute of Coastal Research of the Helmholtz Zentrum Geestacht and the Alfred Wegener Institute for Polar and Marine Research. This work is supported by the International Max Planck Research School on Earth System Modelling (IMPRS-ESM), Hamburg, (CM) and the Cluster of Excellence CliSAP (EXC177), University of Hamburg, funded through the German Science Foundation (DFG) (JB).

3 Observed and simulated seasonal variability of the meridional heat transport in the North Atlantic

Abstract

Two observational time series of the Atlantic meridional heat transport (MHT) have recently become available. Here, we investigate the seasonal variability of the MHT and its relation to the Atlantic meridional overturning circulation (AMOC) using the observed time series at 26°N and 41°N and results from a high-resolution ocean general circulation model. The preliminary analysis presented here focuses on the internal, non-Ekman part of the heat transport, although a true Ekman heat transport, which assumes mass balance, is not available for the observations. Subtracting the Ekman temperature transport from the MHT yields a robust seasonal cycle at both latitudes with differences in phasing between model and observations: At 26°N, the seasonal cycle of the non-Ekman component has a minimum in late winter and a maximum in summer in both model and observations. At 41°N, the observed seasonal cycle has a minimum in fall and no pronounced maximum, while the modeled

seasonal cycle has a minimum in spring and a maximum in late winter. Using the Ekman heat transport, the non-Ekman component has a maximum in summer and a minimum in late winter south of 37°N. North of 37°N, the maximum occurs in fall and the minimum occurs in spring. We find that the AMOC and the MHT are closely related in both model and observations south of 45°N. But the relation breaks down further north due to differences in the seasonality of the Ekman heat and mass transports at the higher latitudes, and the larger contribution of the non-Ekman component to the heat transport than to the mass transport. While preliminary, the analysis suggests coherence of the non-Ekman heat transport across a wide range of latitudes, and confirms that the MHT variability can be inferred from the AMOC variability in the subtropics and at midlatitudes.

3.1 Introduction

Continuous time series of the Atlantic meridional overturning circulation (AMOC) have recently become available at 26°N (Rayner et al., 2011) and 41°N (Willis, 2010), enabling the joint analysis of two observed AMOC estimates. In previous work (Mielke et al., 2013), we have found that the two time series are meridionally coherent on seasonal time scales, and covariable on interannual timescales.

Associated with the AMOC is a northward meridional heat transport (MHT) of up to 1.3 PW (1PW = 10^{15}W) (Ganachaud and Wunsch, 2003), or up to 25% of the total ocean-atmosphere heat transport in the northern hemisphere (Wunsch, 2005). The heat transport impacts sea surface temperatures in the North Atlantic (e.g. Knight et al. (2005), Hobbs and Willis (2012)), and can thereby be linked to rainfall in the equatorial North Atlantic and tropical hurricane frequency (Zhang and Delworth, 2006). The importance of the MHT for the European climate is still under debate (Riser and Lozier, 2013).

Over the next century, the MHT is expected to decline with the AMOC in response to anthropogenic forcing (IPCC, 2013), unless the reduced overturning strength is compensated by an increase in the horizontal or eddy-induced circulation (Drijfhout and Hazeleger, 2006). Fischer et al. (2014b) find that this decline is accompanied by a shift of the MHT's seasonal cycle of up to four months, complicating the interpretation of longterm trends, medium-term climate predictions and the investigation of potential impacts of seasonal heat storage.

The MHT is more difficult to observe and to correctly represent in models than the AMOC, since the computation of the MHT requires knowledge of both the velocity and the temperature field. Most studies therefore focus on the AMOC variability, implicitly assuming a close relation between AMOC and MHT. While recent studies show a close correspondence between the AMOC and the MHT at the subtropical to midlatitudes (e.g. Biastoch et al. (2008) for a model study, Msadek et al. (2013) for observations at 26°N), this relation breaks down further north (Biastoch et al., 2008). Heat transport observations at 26°N (Johns et al., 2011) suggest that the non-Ekman component of the transport could be more important for the MHT variability than previously assumed (e.g. Bryan (1982), Jayne and Marotzke (2001)). Hence, a direct linkage between MHT and AMOC across all latitudes and timescales can at this point not be safely presumed, and a separate analysis is required for the MHT variability.

The aim of this study is therefore to extend previous work on the seasonal variability of the AMOC (Mielke et al., 2013) by repeating the analysis of the seasonal AMOC variability for the MHT (Section 3.3), and then investigating the connection between the AMOC and the MHT (Section 3.4).

3.2 Observations, model and methods

Observations at 26°N are from the RAPID/MOCHA array (Rayner et al., 2011, Johns et al., 2011). Data are available at daily resolution from April 2004. The AMOC transport is calculated as the sum of Florida Straits transport, Ekman transport and upper mid-ocean transport, which is derived from density differences between the eastern and the western boundary (e.g. Cunningham et al. (2007)). For the MHT, the interior eddy heat transport is additionally estimated from repeat hydrographic and expendable bathythermograph (XBT) sections (Johns et al., 2011).

At 41°N, Argo floats and altimeter data are used to estimate the AMOC and the MHT (Willis, 2010, Hobbs and Willis, 2012). Data are available from January 2002 to May 2012, and as three-month running means.

Model results stem from the Max-Planck-Institute ocean model (Marsland et al., 2003, Jungclaus et al., 2006) in the high-resolution STORM setup (von Storch et al., 2012). The model has a horizontal resolution of $0.1° \times 0.1°$, and there are 80 vertical levels ($10 - 280$ m thickness). The simulation is forced by 6-hourly wind stress from the NCEP/NCAR reanalysis (Kalnay et al., 1996), and covers the time period $1948-2010$.

We calculate the MHT at each latitude from the model potential temperature and velocity fields:

$$Q(y) = \rho C_p \int \int \theta v dz dx,$$

where ρ is the density and C_p is the specific heat capacity of sea water, θ is the potential temperature, and v is the meridional velocity. x, y and z denote the longitude, latitude and depth coordinates.

The Ekman heat transport, i.e. the heat transport in the Ekman layer, is

calculated as

$$Q_{Ek}(y) = -C_p \int \frac{\tau_x}{f}(\theta_s - \theta_m)dx,$$

where τ_x is the zonal wind stress, f is the Coriolis parameter, and θ_s and θ_m are the potential temperature at the surface and the mean potential temperature in the water column, respectively. This definition assumes that the Ekman transport is compensated by a uniform barotropic return flow, and may only be valid for the time-dependent fluctuations, but not for the time-mean (Jayne and Marotzke, 2001).

For the observations, only an Ekman temperature transport is available (Johns et al., 2011, Hobbs and Willis, 2012). In contrast to the Ekman heat transport, the Ekman temperature transport does not assume zero mass transport, and is thus not independent of reference temperature. Here, a reference temperature of 0°C is used, and we calculate the Ekman temperature transport as

$$q_{Ek}(y) = -C_p \int \frac{\tau_x}{f}\theta_s dx.$$

The AMOC is calculated as the maximum of the overturning streamfunction, which is obtained directly from the model velocities, and the Ekman transport is calculated as

$$\psi_{Ekman} = -\int \frac{\tau_x}{\rho f}dx.$$

We focus on the time period 2002−2010, where observations at 41°N and the model run overlap. We use monthly data use and smooth them with a three-month running mean for all time series to match the format of the 41°N observations.

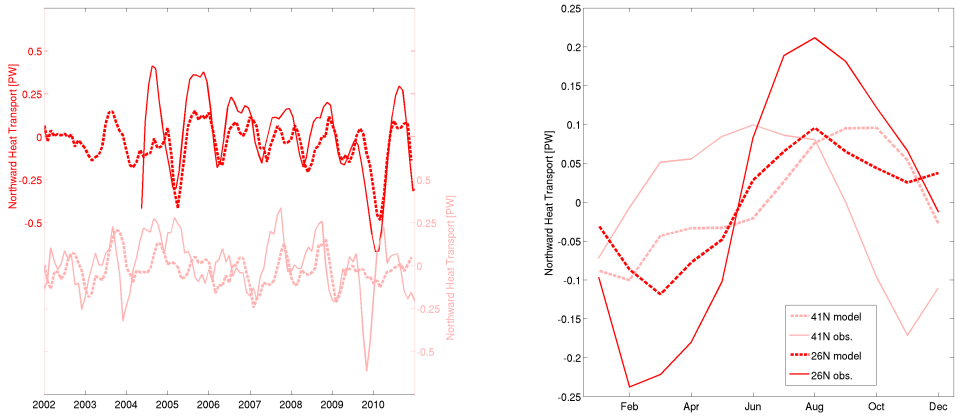

Figure 3.1: Anomaly time series (a) and seasonal cycle anomalies (b) of the observed (solid) and modeled (dashed) meridional heat transport at 26°N (dark) and 41°N (light).

		MHT	Q_{Ek}/q_{Ek}	Q_{nonEk}/q_{nonEk}
Observations	26°N	1.24 ± 0.25	0.31 ± 0.16	0.93 ± 0.16
	41°N	0.55 ± 0.16	-0.19 ± 0.11	0.74 ± 0.10
Model	26°N (temp.)	0.66 ± 0.12	0.25 ± 0.11	0.41 ± 0.08
	26°N		0.13 ± 0.06	0.53 ± 0.08
	41°N (temp.)	0.63 ± 0.09	-0.25 ± 0.17	0.88 ± 0.13
	41°N		-0.12 ± 0.08	0.75 ± 0.07

Table 3.1: Mean values and standard deviations for the observed and modeled MHT and its components. For the model, both temperature (denoted by "temp.") and heat transport values for the Ekman and non-Ekman components are given. All values are in PW.

3.3 Seasonal variability of the MHT in model and observations at 26°N and 41°N

The model does not exactly reproduce the time-mean of the observed MHT at either latitude (Table 3.1). At 26°N, the model underestimates the mean MHT; the observed mean is almost twice as high as the modeled mean. At 41°N, the model overestimates the mean MHT by 15%. Standard deviations are generally lower in the model than in the observations.

Despite the differences in the time-mean transport, the observed and modeled

MHT time series are highly correlated at 26°N ($r = 0.82$, Figure 3.1a). There is no instantaneous correlation between the model and observed time series at 41°N, but a weak correlation at a lag of two months ($r = 0.54$, model leading).

It is notable that the 2009/10 minimum is not well-represented in the 41°N model time series. In the winter of 2009/10, the model time series at 41°N shows a regular seasonal minimum, but not an exceptional downturn like the observations at both latitudes and the model at 26°N. Also, the modeled minimum at 41°N occurs about four months later than the observed minimum which is in September/November. At 26°N, the minimum is represented in both model and observations, and the minimum is only two months earlier in the observations than in the model.

Both the observed and the modeled MHT have a well-defined seasonal cycle at both 26°N and 41°N (Figure 3.1b). For the calculation of the model seasonal cycles, we only use the time period that overlaps with observations, but the results do not change appreciably if the full time series is used. At 26°N, both the model and the observed seasonal cycle show a maximum in August and a minimum February and March. At 41°N, the model has a seasonal maximum in July and a minimum in December, while the observed seasonal cycle shows a maximum in September and a minimum in February. This explains why the correlation between the modeled and the observed time series at 41°N improves for a two-month lag between the two time series.

As the wind-induced Ekman heat transport plays an important role for the variability of the MHT on seasonal timescales (Böning et al., 2001), we analyse the Ekman and the non-Ekman component of the heat transport separately. We analyse both Ekman temperature transport and heat transport for the model. Only the temperature transports can be compared with observations, but the heat transport is more physically meaningful. We denote the Ekman heat transport by Q_{Ek} and the temperature transport by q_{Ek}. Accordingly the non-Ekman components, which are calculated by subtracting the Ekman heat

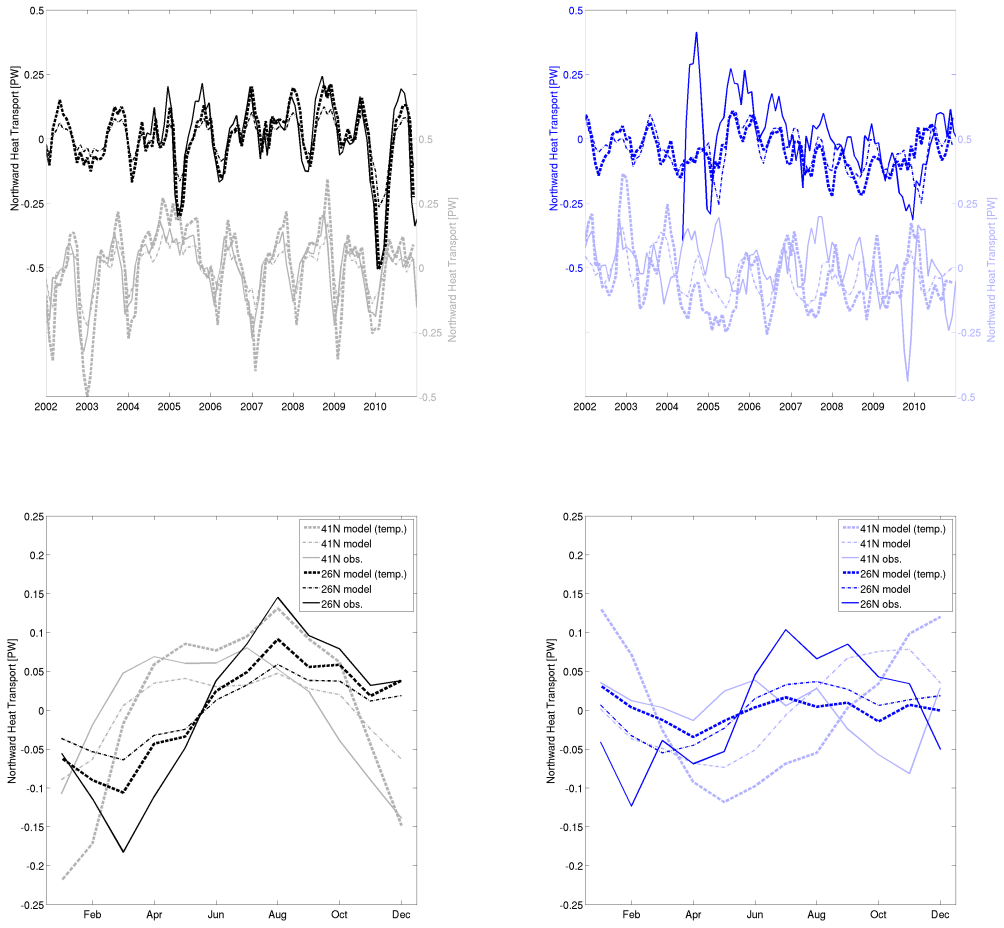

Figure 3.2: Anomaly time series (upper figures) and seasonal cycle anomalies (lower figures) of the observed (solid) and modeled (dotted) Ekman (left panels) and non-Ekman (right panels) components of the MHT at 26°N (dark) and 41°N (light). Dotted lines show the modeled temperature and dashed lines show the modeled heat component components.

or temperature transport from the MHT, are denoted by Q_{nonEk} and q_{nonEk}.

The Ekman temperature and heat transport are positive at 26°N and negative at 41°N (Table 3.1). At 26°N, the observed and modeled q_{Ek} show a similar mean transport, while the observed q_{Ek} at 41°N is weaker than the modeled q_{Ek}.

At both 26°N and 41°N, q_{Ek} has a higher absolute mean and standard deviation

than Q_{Ek}. This implies that q_{nonEk} has a lower time-mean than Q_{nonEk} at 26°N, and the reverse holds for 41°N.

q_{Ek} is highly correlated between model and observations at both 26°N ($r = 0.85$, Figure 3.2a) and 41°N ($r = 0.83$). There is only a much weaker correlation between the observed and modeled q_{nonEk} at 26°N ($r = 0.43$, Figure 3.2b), and no significant correlation at 41°N.

At 26°N, the observed seasonal cycle of q_{nonEk} has a maximum in June to August and a minimum in February. While the modeled q_{nonEk} shows the same seasonality, the model seasonal cycle is more smooth and has a smaller seasonal range (Figure 3.2d). At 41°N, the seasonal cycles of observed and modeled q_{nonEk} differ substantially: While the observed seasonal cycle has a minimum in November and does not show a pronounced maximum, the modeled seasonal cycle has a minimum in May and a maximum in January (Figure 3.2c). In contrast to 26°N, the modeled seasonal range at 41°N exceeds the observed seasonal range.

At 26°N, the seasonal cycle of q_{nonEk} agrees with the seasonal cycle of Q_{nonEk}. But at 41°N, Q_{nonEk} has a maximum in November instead of January like q_{nonEk}, while the minimum occurs in May for both Q_{nonEk} and q_{nonEk}. The reason for this shift in seasonality lies mainly in the smaller seasonal range of Q_{Ek} compared q_{Ek}.

Independent of whether one uses the Ekman temperature or heat transports, or considers the model or the observations, there is a shift in the seasonal cycles of the non-Ekman components of the MHT between 26°N and 41°N. We therefore analyse the variability of the MHT between 26°N and 41°N in the model. For the Ekman and non-Ekman components, we will only discuss the heat transport and not the temperature transport.

The full MHT is coherent throughout the North Atlantic, with a maximum in late winter or early spring and a minimum in late summer or early fall,

although the maximum tends to be later in the year at the higher latitudes (north of 40°N (Figure 3.3a)). Q_{Ek} is coherent south of 35°N and again north of 43°N (Figure 3.3b). Between 35°N and 43°N, the seasonal maximum shifts from late summer to spring, and the minimum shifts from early spring to winter. The seasonal cycle of Q_{nonEk} resembles the seasonal cycle of the full heat transport. However, the seasonal maximum occurs about two months earlier for Q_{nonEk} than for the full MHT north of 45°N, and the shift is less gradual (Figure 3.3c).

Thus, at latitudes south of 35°N, the full heat transport and the Ekman and non-Ekman components all have the same seasonal cycle. It is therefore, from this simple analysis, impossible to determine whether the Ekman or the non-Ekman component is more important in determining the seasonal cycle at the subtropical latitudes. Between 35°N and 45°N, the seasonal cycle of the full heat transport is dominated by the non-Ekman component. Further north, both components influence the seasonality.

To investigate whether the seasonality of the MHT is mainly due to seasonal changes in the temperature or the velocity field, we calculate the seasonal cycle of the MHT with either temperature or velocity kept constant (Figure 3.3 middle and right panels). South of 45°N, the seasonal cycle of the full MHT can almost exclusively be attributed to the seasonality of the velocity field. Further north, positive anomalies in the beginning of the year can be attributed to the seasonality of the temperature field. This is mainly due Q_{Ek}, since Q_{Ek}'s seasonal cycle is determined by changes in the velocity field south of 45°N, but by changes in the temperature field further north. The seasonal cycle of Q_{nonEk} is a composite of the seasonality of the temperature and the velocity at all latitudes. The seasonal maximum occurs one month earlier if the velocity field is kept fixed, and one month later if the temperature is kept fixed.

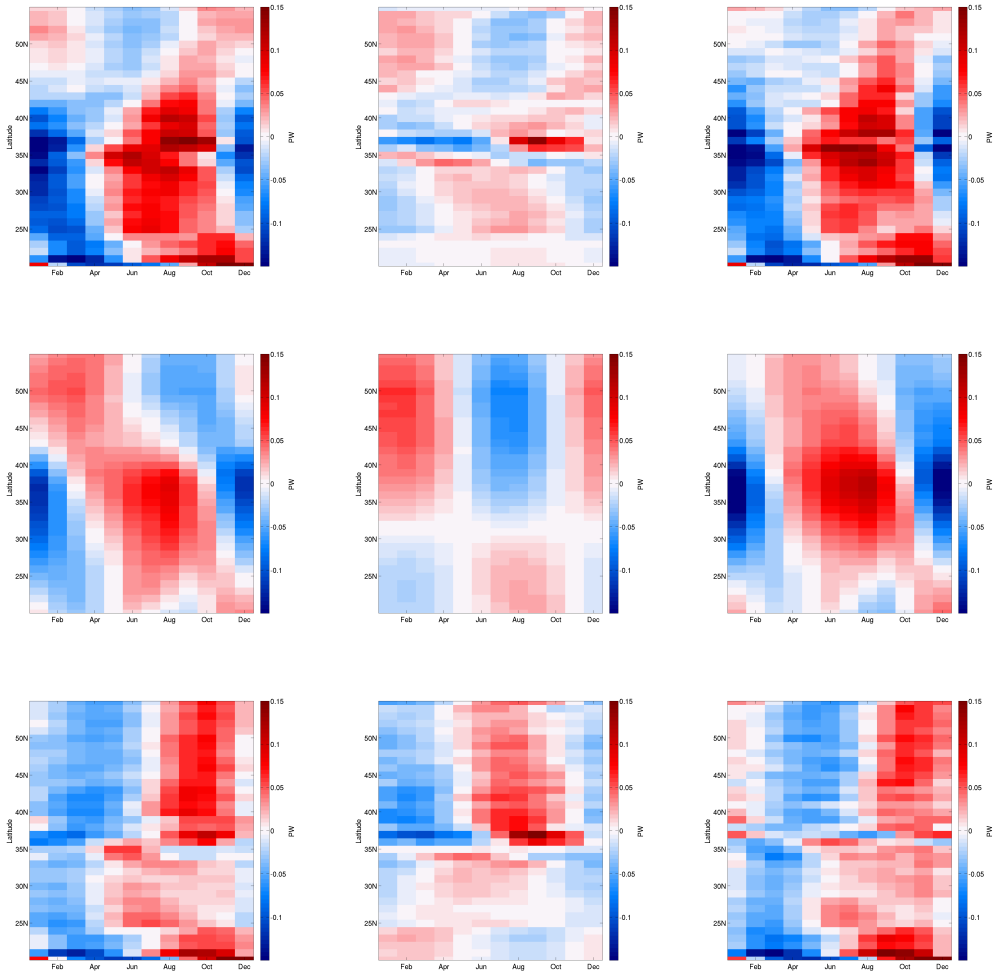

Figure 3.3: Hovmoeller plots of the mean seasonal cycle anomalies of the full MHT (upper panels), Q_{Ek} (middle panels) and Q_{nonEk} (lower panels). Both temperature and velocities fields are variable in the left panels. The middle panels show the heat transport computed with velocity/wind stress kept constant and the right panels show the heat transport computed with the temperature kept const.

3.4 The MHT's relation to the AMOC

The model MHT is underestimated at 26°N and overestimated at 41°N, with values 47% below and 15% above their observational counterparts (Section 3.3). The overestimation at 41°N can be explained by the overestimation of the mass transport by 15%, but at 26°N, the mean mass transport is underes-

timated by only 8%.

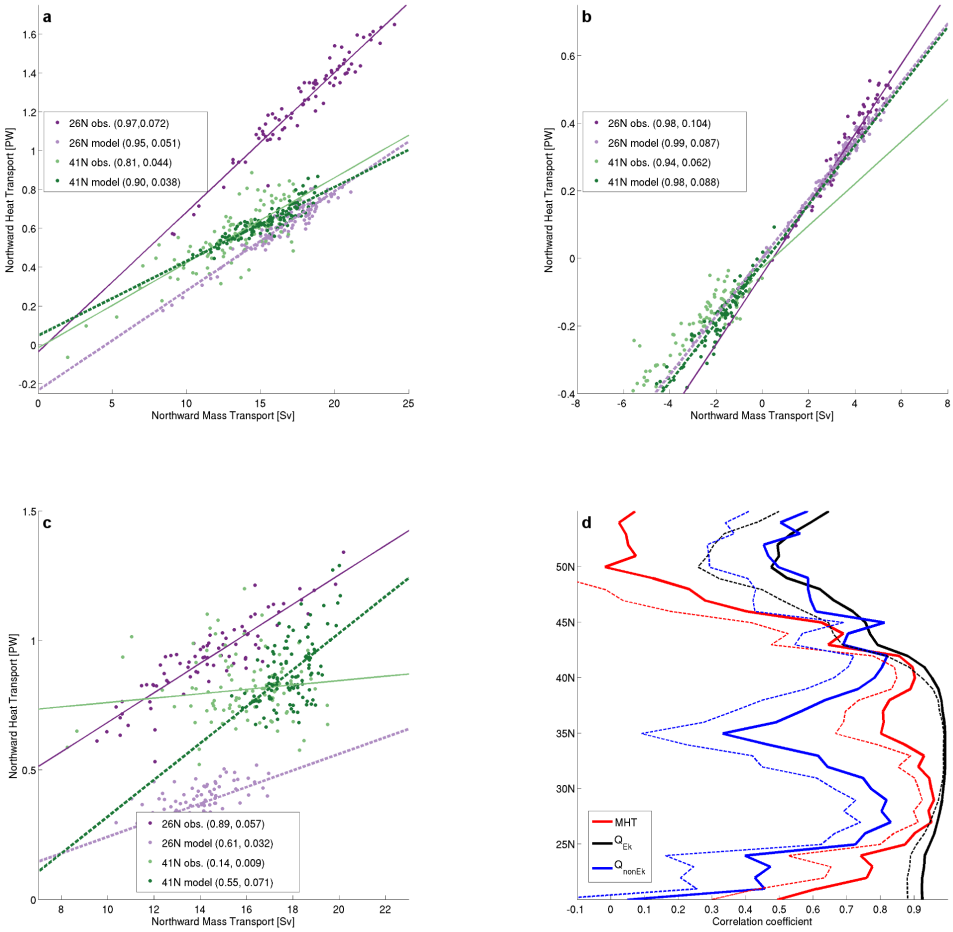

Figure 3.4: Regression of the observed (solid) and modeled (dashed) a) total meridional heat transport, b) q_{Ek}, c) q_{nonEk} and the corresponding mass transport components at 26°N (purple) and 41°N (green). For each pair of values, correlation (first value) and slope (second value) are given. d) Correlation coefficients for the correlation between MHT and AMOC variability and the individual transport components in the model. Dashed lines show the lower limit of the 99% confidence interval.

As previous studies (Msadek et al., 2013), we find a linear relation between the MHT and AMOC variabilities in both model and observations. The correlation coefficient is slightly higher at 26°N than at 41°N (for exact values see Figure 3.4a). q_{Ek} and the Ekman mass component show an even higher correlation (Figure 3.4b), as expected since both the model and observed Ekman transport

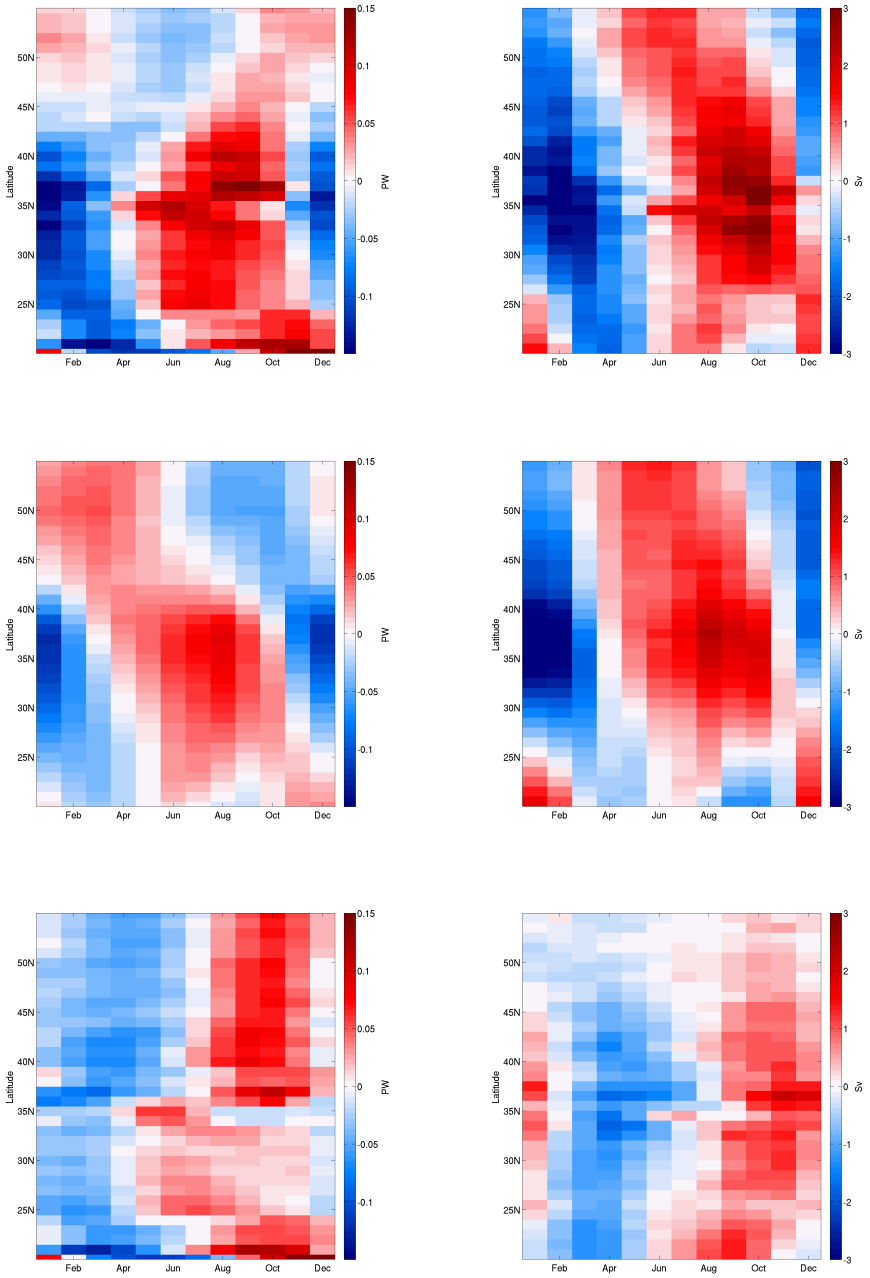

Figure 3.5: Hovmoeller plots of the mean seasonal cycles anomalies for the heat (left panels) and mass transport (right panels): MHT and AMOC (upper panels), Q_{Ek} and the Ekman mass transport (middle panels), Q_{nonEk} and the non-Ekman component of the AMOC (lower panels).

are calculated from reanalysis data. For the observed q_{nonEk}, there is a high correlation with the non-Ekman component of the AMOC at 26°N, but no correlation at 41°N.

In the model, the correlation between q_{nonEk} and the non-Ekman mass transport at 26°N is weaker than in the observations. In contrast to the observations, there is also a significant correlation at 41°N (Figure 3.4c). For Q_{nonEk}, the correlations are slightly higher than for q_{nonEk} at both 26°N and 41°N ($r = 0.77$ and $r = 0.72$ versus $r = 0.61$ and $r = 0.55$).

For a better understanding of how changes in the AMOC are represented in the MHT, we regress the MHT and its components on the AMOC and the corresponding AMOC components (Figure 3.4a). The model underestimates the observed slope at both 26°N and 41°N. This means that the discrepancies between model and observations increase for higher AMOC values. At 26°N, this can be attributed to both q_{Ek} and q_{nonEk}, as the model underestimates the slope in both cases (Figures 3.4b and c). In contrast, the slope for the Ekman component is overestimated at 41°N. A meaningful comparison of the slopes of the observed and modeled q_{nonEk} at 41°N is not possible, as the observed heat and mass transports are not correlated.

There are notable differences in the sensitivity of the heat transport components to changes in the mass transport components between the two latitudes. For the full MHT, the slope is higher at 26°N than at 41°N in both model and observations. Thus, the MHT at 26°N is more sensitive to changes in the mass transport than at 41°N. For q_{Ek}, the slope is higher at 26°N than at 41°N in the observations, but virtually the same in the model. For the q_{nonEk} the modeled slope is higher at 41°N than at 26°N. Hence, q_{nonEk} is more sensitive to changes in the non-Ekman mass transport at 41°N than at 26°N.

Using the model to analyse the latitudinal dependence of the relation between AMOC and MHT throughout the North Atlantic, we find a high correlation between AMOC and MHT until about 45°N, north of which the correlation

breaks down (Figure 3.4d). The correlation between Q_{Ek} and the Ekman mass transport is higher than the correlation between the full transports at all latitudes, but also decreases north of 40°N. The correlation between Q_{nonEk} and the non-Ekman component of the mass transport shows maxima at 28°N and 42°N, but decreases around 35°N.

The breakdown of the correlation between AMOC and MHT north of 45°N can neither be attributed exclusively to the Ekman or the non-Ekman component, although the shift in the seasonal cycle of Q_{Ek} north of 45°N is not mirrored in the Ekman mass transport (Figure 3.5). Instead, the non-Ekman component, whose seasonal cycle differs from the Ekman component's seasonal cycle, is important for the variability of the MHT than for the AMOC, and this results in a loss of correlation.

3.5 Discussion of results and preliminary conclusions

The underestimation of the observed mean heat transport at 26°N that we find here has also been noted in previous studies, both in coupled (Jia, 2003, Msadek et al., 2013) and ocean-only models (Böning et al., 2001, Biastoch et al., 2008), and cannot solely be explained by an underestimation of the mass transport. At 41°N, the model overestimates the mean heat transport from Hobbs and Willis (2012), but this can be explained by the difference in the mass transport. Also, the estimate from Hobbs and Willis (2012) is low compared to previous hydrographic estimates (Hobbs and Willis (2012) and references therein), whereas the 26°N estimate from Johns et al. (2011) fits within the error bars of earlier estimates.

Msadek et al. (2013) have attributed the underestimation of the mean observed heat transport at 26°N to the incorrect representation of the horizontal, or

gyre, circulation in the model. This could explain why the observed mean is better represented at 41°N: Since 41°N is located at the gyre boundary, one would not expect at large contribution from the gyre at this latitude. A decomposition of the heat transport in overturning and gyre component would shed light on this potential problem. Also, there are known temperature biases in the model (Jungclaus et al., 2013). Since the differences between the mean observed and modeled Ekman mass transport are smaller than for the heat transport (Mielke et al., 2013), the discrepancy between the time-mean of the observed and modeled Ekman heat transports can only be attributed to differences in the temperature field. A detailed analysis of the temperature field and a comparison with observations would be useful.

The observed variability of the MHT is well-represented in the model. At 41°N, there is a shift of two to three months between the observed and modeled seasonal cycle. This shift between model and observations is also apparent in the AMOC seasonal cycle (Mielke et al., 2013), and can thus not be attributed to differences in temperature field. Indeed, the modeled MHT seasonality at 41°N remains unchanged if the velocity field is kept fixed. The reasons for the discrepancy thus remain unclear.

The MHT seasonal cycle at 26°N has a maximum in late summer and a minimum in late winter/early spring in both model and observations. At 41°N, the model MHT shows a similar seasonal cycle, but the observed seasonal cycle has a maximum in summer and a minimum in winter. At both latitudes, and in model and observations, the MHT seasonal cycle agrees with the AMOC seasonal cycle.

South of 35°N and north of 45°N the MHT seasonal cycle has to be equally attributed to the Ekman and the non-Ekman component of the heat transport, while the non-Ekman component dominates the seasonality between 35°N and 45°N. In this regard, the MHT seasonal cycle differs from the AMOC seasonal cycle which is mainly associated with the Ekman component throughout the

North Atlantic (Mielke et al., 2013). Previous model studies have attributed the seasonal to interannual variability of the heat transport mainly to the Ekman component (Böning et al., 2001, Jayne and Marotzke, 2001), but recent results from the RAPID array emphasize the importance of the non-Ekman transport (Johns et al., 2011).

There is a close correspondence between mass and heat transport in model and observations at both latitudes. Taking a broader look at the North Atlantic in the model, the correlation breaks down north of 45°N. Biastoch et al. (2008) find a similar decrease in correlation north of 40°N, which they attribute to zonal temperature differences that become more important at the higher latitudes and would require the use of density coordinates instead of depth coordinates, and Yeager et al. (2012) suggest that the horizontal component might be more important at these latitudes. Our analysis suggests that the loss of correlation mainly stems from the larger contribution of the non-Ekman component to the heat transport than to the mass transport, and a shift in the Ekman heat transport's seasonal cycle north of 45°N. This shift is caused by the temperature field and is therefore not apparent in the Ekman mass transport.

The sensitivity of changes in the MHT to changes in the AMOC is underestimated in the model at both latitudes. Thus, although the present variability of the MHT seems to be well-represented in the model, the magnitude of a long-term decrease, as expected with the decrease of the AMOC in response to anthropogenic climate change, would likely be underestimated.

3.6 Preliminary conclusions and outlook

Based on our analysis of the seasonal MHT variability and its relation to the AMOC circulation in observations and a high-resolution model, we come to the following preliminary conclusions:

- The model severely underestimates the mean heat transport at 26°N. The observed mean is better represented at 41°N.

- Subtracting the Ekman temperature transport from the MHT, we find phasing differences between the modeled and observed non-Ekman components of the heat transport: At 26°N, both the observed and the modeled seasonal cycle of the non-Ekman component have a minimum in late winter and a maximum in summer. At 41°N, the observed seasonal cycle has a minimum in fall and no pronounced maximum, while the modeled seasonal cycle has a minimum in spring and a maximum in late winter.

- In the model, the Ekman heat transport, which assumes zero mass transport, can also be computed. Using the Ekman heat transport, the non-Ekman component has a maximum in summer and a minimum in late winter south of 35°N. North of 35°N, the maximum occurs in fall and the minimum occurs in spring. At all latitudes in the North Atlantic, the seasonal cycle of the non-Ekman component can be attributed to both the velocity and the temperature field.

- The AMOC and the MHT variability are closely related at both 26°N and 41°N in model and observations. Using the model for a broader look at the North Atlantic reveals that the relation breaks down north of 45°N.

A detailed analysis of the temperature field, and a comparison with the observational temperature field will be helpful in understanding the underestimation of the mean heat transport at 26°N. Along the same lines, it should be investigated whether the model misrepresents the horizontal component of the heat transport, as found by (Msadek et al., 2013). A decomposition of the model heat transport in overturning and horizontal component might also contribute to understanding the disagreement between the AMOC and the MHT variability at the higher latitudes. For a physically more meaningful analysis of

the observed non-Ekman components, an observed heat transport (instead of a temperature transport) will be required.

4 Seasonal variability of the modeled and observed Deep Western Boundary Current in the North Atlantic[1]

Abstract

We investigate the seasonal variability of the North Atlantic Deep Western Boundary Current (DWBC) in a high-resolution ocean general circulation model. The DWBC is defined in density classes after a comparison of temperature and salinity data between observations and the model. The modeled DWBC's mean, structure and range of seasonal variability are consistent with observations. We find that the DWBC has a prominent seasonal cycle, forced by local wind stress curl variations throughout the North Atlantic, and particularly in the subtropical gyre. This implies coherence of the DWBC both within the subtropical gyre, and possibly within the subpolar gyre, but the seasonal cycle is 180-degree out-of-phase between the two gyres: In the subtropical gyre, the southward transport in the DWBC is strongest in fall and

[1]C. L. Mielke, S. F. Gary, K. Shimizu, J. M. Toole, and J. Baehr (2013), Seasonal variability of the modeled and observed Deep Western Boundary Current in the North Atlantic, submitted to *Journal of Geophysical Research: Oceans*.

weakest in late winter, while the seasonality is reversed in the subpolar gyre. In the subtropical gyre, the western basin transports below 1000 m show a maximum in fall and a minimum in late winter, in agreement with the DWBC seasonal cycle. Because of an anti-correlation between the transports in the eastern and western basin, neither the Atlantic meridional overturning circulation (AMOC) nor its seasonal cycle can be directly inferred from the DWBC. Our results suggest that modulations of the western basin seasonal cycle might be inferred from changes in the DWBC seasonal cycle, which could be readily obtained from wind stress variability at the western boundary.

4.1 Introduction

The Deep Western Boundary Current (DWBC) is a major part of the southward branch of the Atlantic meridional overturning circulation (AMOC). Simplified theories of the circulation suggest that the deep flow in the basin interior is poleward, and all southward flow confined to the deep western boundary (Stommel, 1957, Stommel and Arons, 1960). Although recent studies suggest that recirculations and interior pathways are also important branches of the return flow at mid-latitudes (Bower et al., 2009, Gary et al., 2011, 2012), disturbances from the higher latitudes propagate along the DWBC, as coastally trapped waves or, on longer timescales, by advection (Johnson and Marshall, 2002, Yang and Joyce, 2003, Zhang, 2010, Elipot et al., 2013).

There is a long history of observations of the structure and strength of the DWBC (Meinen et al. (2013a) and references therein), but continuous time series have only recently become available, enabling for the first time studies of the intraannual and seasonal variability of the DWBC (Toole et al., 2011, Meinen et al., 2013a, Fischer et al., 2014a). A precise knowledge of the seasonality is necessary for the correct interpretation of interannual and decadal trends (Kanzow et al., 2010) and for medium-term climate projections. Much

like the AMOC, the observed DWBC shows variability on timescales from days to interannual, but because of the short observational time series, there are only inconclusive, or even contradicting, results on the seasonality of the DWBC: At 26°N, Meinen et al. (2013a) do not find a strong annual signal in their data, although that depends on how far out they integrate the transports, and the seasonality changes considerably if a random four years are used instead of the full five year time series. Their results conflict with earlier results from current meter data from Lee et al. (1996), who find a seasonal cycle with a maximum southward transport in October and a minimum in February. Toole et al. (2011) and Fischer et al. (2014a) find indications of a seasonal cycle in the four-year observational Line W time series and the nine-year record at 53°N. However, in all cases, the time series are too short to determine a statistically significant seasonal cycle.

At present, the question of whether the DWBC has a seasonal cycle can therefore only be investigated in model studies. Focusing on 26°N, Böning et al. (1991) find a seasonal cycle in the DWBC, which they link to wind stress curl variability in the western part of the basin.

To broaden the analysis across the North Atlantic, we define a DWBC in a high-resolution NCEP-forced ocean model (Section 2). After a comparison of the model results with available observations (Section 3), we take advantage of the 60-year model time series to evaluate the DWBC variability throughout the North Atlantic. As we find a dominant seasonal signal, we then focus on the analysis of the seasonal cycle of the DWBC and its forcing mechanisms (Section 4). We also investigate whether the seasonal cycle of the basin-wide meridional transport can be inferred from the DWBC seasonal cycle (Section 5).

4.2 Model and methods

4.2.1 Model and observations

We use observations from both the RAPID/MOCHA array at 26°N (Rayner et al., 2011) and the Line W array at 39°N (Toole et al., 2011). At 26°N, we use merged western boundary profiles of observed temperature and salinity from April 2004 to April 2011. At Line W, we use time-mean temperature and salinity data from moorings W3 and W5 as well as a time series of DWBC transports from May 2004 to April 2008.

The model employed in this study is the Max-Planck-Institute ocean model (Marsland et al., 2003, Jungclaus et al., 2006) in the high-resolution STORM setup (von Storch et al., 2012) with a horizontal resolution of 0.1° and 80 vertical levels ($10 - 280$ m thickness). The simulation covers the time period 1948–2010, and is forced by 6-hourly NCEP wind stress (Kalnay et al., 1996). Velocity, temperature and salinity are output daily, but we use monthly averages for our analysis, retaining the spatial resolution. Sea surface salinity is relaxed to the Polar Science Center Hydrographic Climatology (Steele et al., 2001), and the AMOC maximum is located at about 35°N and 1000 m depth.

As in Mielke et al. (2013), the AMOC in the model is defined as the maximum of the overturning streamfunction ψ, which is calculated directly from the output meridional velocities $v(x, y, z, t)$ as

$$\psi(y, z, t) = \int_0^z \int_{x_{east}}^{x_{west}} v(x, y, z, t) dx dz,$$

where x, y, z and t denote the longitude, latitude, depth and time coordinates, and x_{west} and x_{east} are the latitude- and depth-dependent western and eastern ocean boundaries. Calculating the AMOC at a fixed depth, e.g. 1000 m, only marginally changes the mean and variability of the AMOC.

As we are interested in the internal part of the circulation, we calculate the non-Ekman component of the AMOC by subtracting the Ekman transport from the full transport. The Ekman transport is calculated from the zonal wind stress $\tau_x(x, y, t)$ as

$$\psi_{Ekman}(y, t) = -\int \frac{\tau_x(x, y, t)}{\rho f(y)} dx,$$

where ρ is a reference density and f is the Coriolis parameter. Transport values are given in Sverdrups (1 Sv = 10^6 m/s).

4.2.2 Defining a DWBC in the model

Calculating a DWBC in the model is not straightforward. Defining the DWBC in depth layers is imprecise, due to differences in ocean stratification between different latitudes. In observations, the water masses that compromise the DWBC are customarily defined in terms of density classes (e.g., Yashayaev (2007), van Sebille et al. (2011)), although other quantities, including temperature, salinity and tracers, have also been used (e.g., McCartney (1992), Molinari et al. (1992)).

	Observations		Model
	26°N (σ_2)	line W (γ_n)	σ_2
uLSW	$36.5 - 36.82$	$27.8 - 27.897$	$36.5 - 36.82$
cLSW	$36.82 - 36.97$	$27.897 - 27.983$	
ISOW	$36.97 - 37.08$	$27.983 - 28.066$	$36.82 - 37.08$
DSOW	$37.08 - 37.16$	> 28.125	> 37.08

Table 4.1: Definition of density classes in observations and model. Values are in kg/m^3. The LSW layers cannot be properly distinguished in the model. Observations at 26°N are from van Sebille et al. (2011), and observations at Line W are from Toole et al. (2011).

Following van Sebille et al. (2011), we use σ_2 densities for the identification of the DWBC's water masses. van Sebille et al. (2011) focused on the Labrador Sea Water (LSW) at the Abaco line east of the Bahamas at 26°N and base

their choice of density classes on Yashayaev (2007). In his analysis, Yashayaev (2007) found LSW properties change considerably over time. For example, severe winters in the late 1980s and early 1990s caused much denser LSW than the conditions ten years later. To facilitate the analysis and for consistency with previous definitions of water masses outside the subpolar regions, van Sebille et al. (2011) define the LSW as a compilation of the density classes from Yashayaev (2007), and find that this classification agrees well with previous, local classification in depth space at the Abaco line (Molinari et al., 1992). They also note that using neutral density instead of potential density does not change the results. The density classes from van Sebille et al. (2011) can be found in Table 4.1.

As there are temperature and salinity biases in the model (Jungclaus et al. (2013), Figure 4.1), we do not use the same density classes to define the DWBC in the model. Instead, we compare model and observed temperature-salinity curves (Figure 4.1). At both 26°N and Line W, the observed Iceland-Scotland Overflow Water (ISOW) is the most distinguishable, with (relatively) constant salinity, in agreement with observations (Yashayaev, 2007), and we therefore define the ISOW in the model with a σ_2 density range of $36.82 - 37.08$ kg/m^3. Everything with a higher density is defined as Denmark Straits Overflow Water (DSOW), while lower densities are classified as LSW, with a reasonable lower limit. Distinguishing between upper LSW and central LSW is not possible in the model. Similarly, there is an upper limit for the DSOW densities in the observations, which cannot be identified in the model. With these considerations, we define the densities classes in the model as listed in Table 4.1 and shown in Figure 4.1.

For the zonal extent of the DWBC, we first identify the western edge of the DWBC in the horizontal flow field. Often, this is the coast, but in some cases, a northward return flow sits inshore of the DWBC. We then integrate the velocities eastward until the next zero crossing at each time step. This is, in principle, equivalent to the southward maximum of the transport stream-

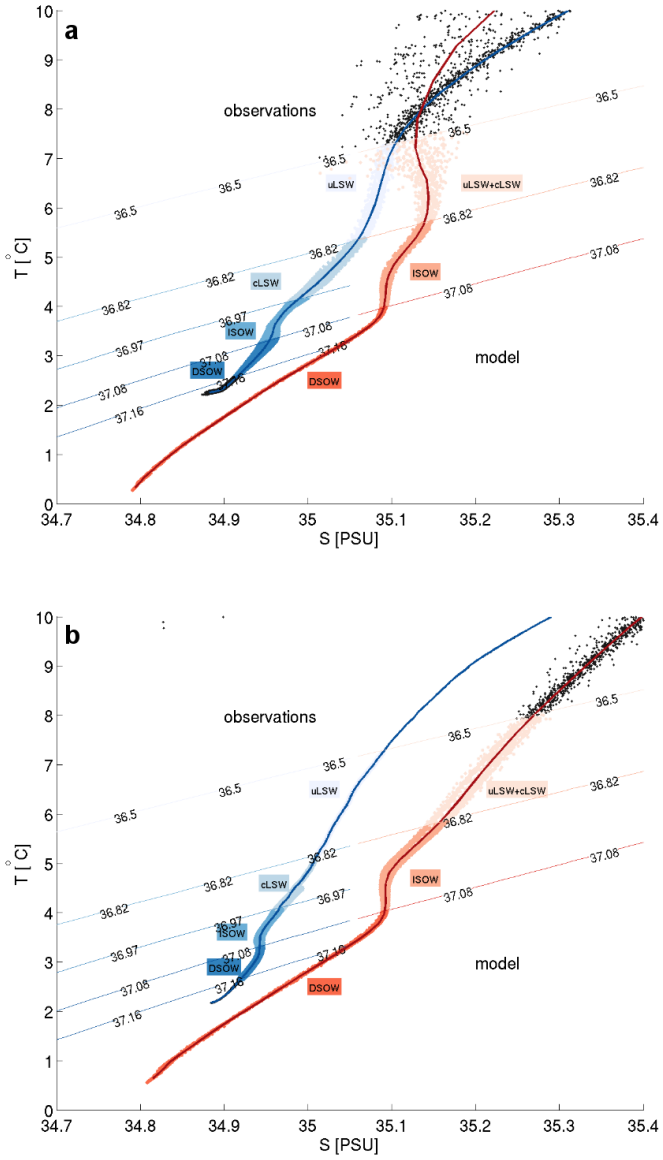

Figure 4.1: Temperature-salinity diagram at 26°N (a) and Line W (b) for model and observations with defined density contours for model (right) and observations (left). Density contour values are in kg/m^3. Dots represent individual data points, and solid lines are the mean values of the corresponding dots.

function, but we do permit integration over small recirculations after careful comparison with the velocity field. Due to the complicated nature of the flow field in the western North Atlantic (Section 4.3.1), the DWBC is not clearly

confined at every latitude, and as the DWBC is a narrow current with high velocities, one has to be very careful not to over- or underestimate the mean and variability by identifying a recirculation as part of the DWBC. The definition in density classes implies that the upper depth limit changes with every time step. Thus, we can track meandering and changes in water masses in the DWBC.

Also, a particular latitude in the real world is not necessarily "equivalent" to the same latitude in the model world: For example, the observational Line W is close to the Gulf Stream separation, but in the model the Gulf Stream path is more zonal after the separation. As a result, we correct the nominal latitude to place the DWBC section at a comparable dynamical latitude for a comparison with the observations. As this requires a careful analysis of the local velocity field for each timestep, we only define a DWBC in the model at five locations throughout the North Atlantic: 26°N, 28°N, 32°N, a line roughly equivalent to the observational Line W, and 48°N (Figure 4.2a). The region between Line W and 48°N is dynamically very active and the DWBC is weaker and not as narrow in this region (Section 4.3.1), so a meaningful definition of a DWBC is not possible here. Thus, there are in total four subtropical and one subpolar latitude at which we compute a DWBC time series from monthly temperature, salinity and velocity data from 1950 to 2010.

4.3 The modeled and observational DWBC: structure, mean, and temporal variability

4.3.1 The flowfield in the western North Atlantic

In the model, the DWBC exits the Labrador Sea as a continuous flow, but the flow pattern becomes more complicated once the waters reach Flemish Cap

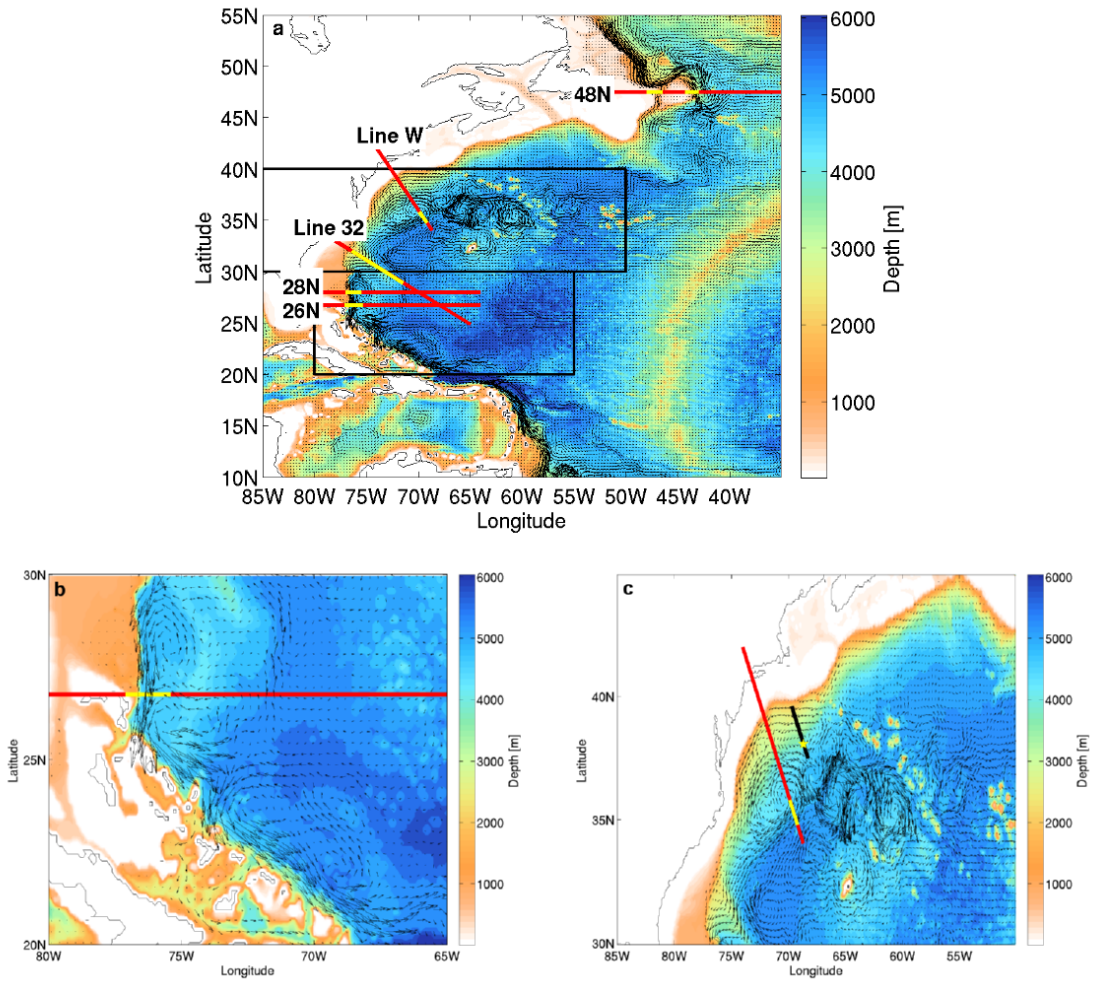

Figure 4.2: a) Bathymetry of the modeled western North Atlantic and DWBC velocity vectors. Vectors are computed by integrating the zonal and meridional velocities over the density classes of the DWBC, and every third vector is shown. b) Zoom-in on the equatorial North Atlantic and 26°N, c) Zoom-in on the region around Line W with location of the observed Line W (black line) and mooring W5 (star). Locations where the DWBC is calculated in the model are marked by red lines. The yellow part indicates the extent of the mean DWBC at each location.

(Figure 4.2a). There are a number of recirculations just south of the New England Seamounts, and the flow is generally less confined. South of 30°N the flow is again better confined, although recirculation gyres are still found farther offshore.

4.3.1.1 Boundary currents near 26°N in model and observations

At 26°N, a large part of the northward transport is confined to the Florida Straits west of the Bahamas, while the southward transport, including the DWBC, is located east of the Bahamas. Above the DWBC sits the shallow northward flowing Antilles current. The region east of the Bahamas is one of the best observed regions in the world oceans, with moorings first deployed in 1986 (Lee et al., 1990).

Comparable to the model study by Xu et al. (2012), there are two permanent recirculation gyres (Figure 4.2b). The first is located north of 26°N within the Blake Basin, while the second is a little further south. Because of the location of the second gyre, we calculate the DWBC at "26°N" at roughly 26.75°N (Figure 4.2a and b), between the two gyres. The RAPID/MOCHA array is at 26.5°N.

With this choice, the DWBC can be clearly identified in the mean meridional velocity field (Figure 4.3a). Generally, the model is able to reproduce the observed flow structure, that is the location of the Antilles Current and DWBC and the recirculations off-shore of the DWBC. As in observations (Bryden et al., 2005, Johns et al., 2008), the modeled Antilles Current is located above 800 m, although it extends farther offshore than indicated by observations. The mean modeled Antilles current has maximum speeds of 40 cm/s, which is in agreement with observations. The mean modeled DWBC, on the other hand, has higher maximum speeds than its observational counterparts: 26 cm/s in the model versus 16 cm/s in observations (Bryden et al., 2005).

On average, the modeled DWBC is about 160 km wide, about as wide as the mean DWBC from Bryden et al. (2005) (170 km), but notably wider than the 100 km reported by Johns et al. (2008). Similar to the model results from Xu et al. (2012), we find two recirculations patterns. Both are located a little further offshore than reported by Xu et al. (2012), but they also find a nar-

rower DWBC. A similar pattern of recirculations is also found in observations (Bryden et al., 2005).

In the model, the LSW is found between 850 m± 35 m and 1150 m ± 35 m. This is shallower than for the RAPID observations used to determine the density classes, where the LSW is in the mean located between 910 m ± 22 m and 1485 m ± 55 m. The layer is also much thinner in the model. The model ISOW extends until 2040 m ± 30 m, compared to 2410 m ± 55 m for the observed ISOW. In previous observational studies at this latitude (Molinari et al., 1992, van Sebille et al., 2011), the water masses were found even deeper than indicated by the RAPID observations.

It would be possible to choose density classes in the model such that the water masses in the model are at the same depth as in the observations. However, we do not expect the water masses to be located at the same depth in model and observations, and therefore use the density classes defined for the model (Section 4.2.2).

4.3.1.2 The modeled Line W

The region around Line W is dynamically active in the model (Figure 4.2c), with recirculation gyres and high eddy kinetic energy.

In the real ocean, Line W intersects with the Gulf Stream about 230 km offshore, at the location of mooring W5. This intersection is visible in both the observed mean temperature and velocity fields. But in the model, there is no intersection of the observed Line W (black line in Figure 4.2c) with the Gulf Stream. This could make a difference for the DWBC variability, since the position of the Gulf Stream North Wall might influence the transport (Toole et al., 2011). Another problem with the definition of a modeled Line W is that, even in the time-mean, the velocity field in the area is complex (Figure 4.2c), and involves a number of recirculations, especially south of the New England

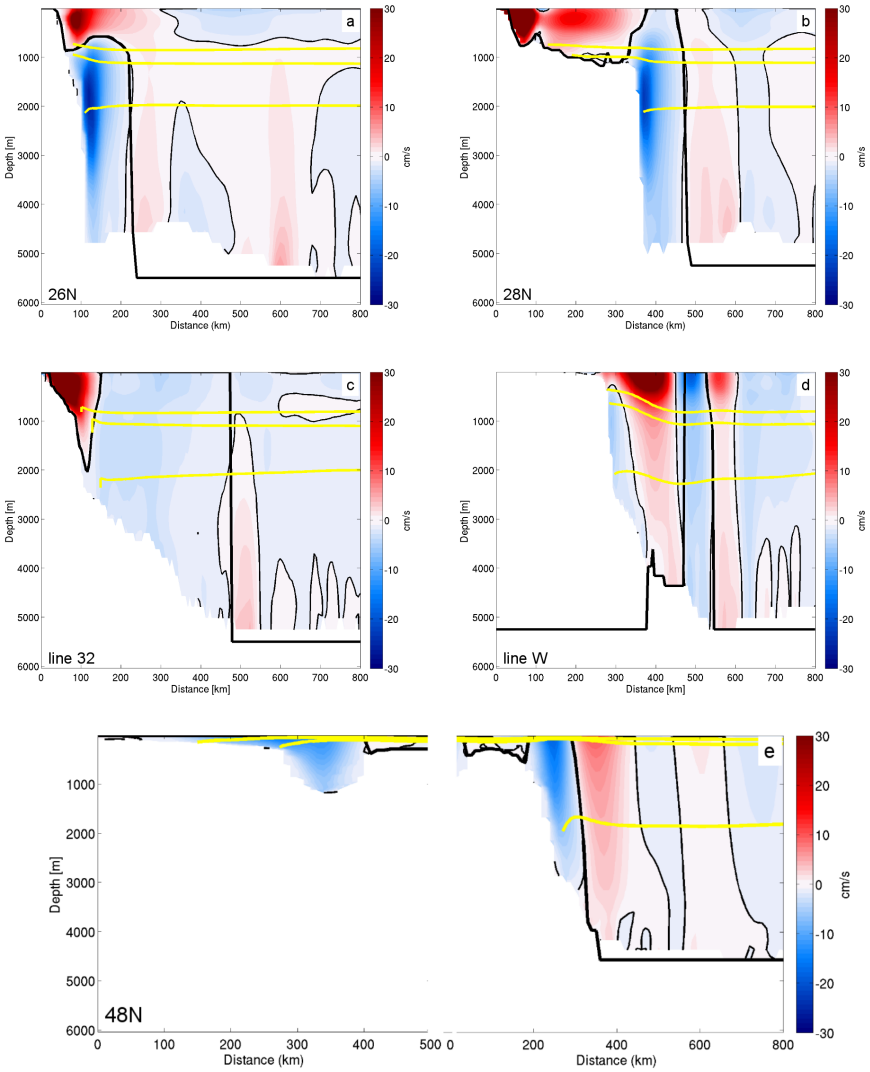

Figure 4.3: Mean meridional velocities at the western boundary at a) 26°N, east of the Bahamas, b) 28°N, c) Line 32, d) Line W, e) 48°N. Thin black lines indicate the zero isotachs. The thick black line is the automatically computed DWBC limit. Yellow lines indicate the boundaries between the different water masses, with the uppermost line representing the upper limit of LSW. Note that the zero isotach does not precisely match with the DWBC boundaries, as this is the mean DWBC boundary, and not the DWBC boundary calculated for the mean velocity field.

Seamounts. The observational Line W is located right in the middle of an inshore recirculation.

Therefore, we define the model "Line W" further south, at the "exit" of the

southern most recirculation (red line in Figure 4.2c). After this recirculation, the DWBC is again well-defined, so we can be confident to capture most of the transport, while still being near the location of the observed Line W. As a result of this adjustment, the DWBC at the model Line W is separated from the coast by recirculations, over which we do not integrate (Figures 4.2c and 4.3d).

The DWBC at Line W is narrower than at 26°N (Figure 4.2c), and has lower core velocities. In agreement with observations (Toole et al., 2011), the DWBC's core is shallower than at 26°N. At mooring W5, the observed LSW is found between 830 m ± 160 m and 2080 m ± 140 m, and the ISOW above 2900 m ± 140 m. For the model, the LSW at Line W is located between 755 m ± 60 m and 1070 m ± 40 m, and ISOW is above 2180 m ± 55 m. In contrast to the observations, the Gulf Stream in the model is located inshore of the DWBC.

4.3.1.3 The DWBC at 28°N, 32°N and 48°N

Sections of the average velocity with mean density contours and zonal extent of the DWBC for 28°N, Line 32 and 48°N are in Figure 4.3. At 28°N (Figure 4.3b), the DWBC's structure is very similar to the structure of the DWBC at 26°N, although the Antilles Current joins the Florida Current north of the Bahamas, and thus the northward and southward parts of the transport at 28°N are side by side rather than on top of each other. Core velocities are also similar to 26°N.

At Line 32, the DWBC is less confined, as evident from the flow field (Figure 4.2a). This results in lower core velocities in the DWBC (Figure 4.3c). The water masses are located at about the same depths as at 26°N and 28°N.

At 48°N, the DWBC is split in two components, one west and one east of Flemish Cap. The DWBC east of Flemish Cap is roughly as wide as it is at

Line W, but only extends to a depth of about 3500 m, compared to 5000 m at the other locations. Observations with RAFOS floats indicate that a large fraction of LSW exits the DWBC between Flemish Cap at 48°N and the Tail of the Grand Banks at 45°N (Bower et al., 2009). This is also evident from the flow field (Figure 4.2a), which shows recirculations to the subpolar gyre. At Flemish Cap, the northward part of a recirculation sits within the DWBC's density classes east of the southward current (Figure 4.2a and Figure 4.3e). Mean maximum core velocities in the DWBC at 48°N are less than 20 m/s, considerably less than at 26°N and 28°N, but similar to Line W.

The LSW and the ISOW are much shallower than at the lower latitudes (Figure 4.3e); the LSW starts at 100 m. Observations north of Flemish Cap (Bower et al., 2011) find the LSW similarly close to the surface, but extending until about 2000 m. In observations at Grand Banks (Schott et al., 2006), the LSW sits below 500 m.

4.3.2 Modeled and observed variability

At 26°N, the computed model DWBC has a mean southward transport of -28.8 Sv $\pm$ 7.5 Sv, and at Line W the mean southward transport is -18.9 Sv $\pm$ 11.5 Sv. The modeled mean transport and standard deviation at Line W are similar to the observations (Toole et al., 2011), although the standard deviations are similar (see Table 4.2 for exact values). At 26°N, Johns et al. (2008) find a mean southward DWBC transport of -26.5 Sv for $2004-2005$, similar to the estimate from current meter records by Bryden et al. (2005) (-24.2), but lower than the estimate by Meinen et al. (2013a) (-32 Sv $\pm$ 16 Sv) both in terms of the variability and the mean. At both latitudes, the LSW layer shows the lowest mean and standard deviation (Table 4.2 for exact values), while the DSOW layer has the highest mean and standard deviation, in agreement with the Line W observations (Toole et al., 2011). The differences in mean value may result from differences in layer

thickness between model and observations; although this is less relevant for the full DWBC than for the individual water mass transports.

	Model					Observations	
	26°N	28°N	Line 32	Line W	48°N	26°N	Line W
LSW	−2.1 ±0.8	−2.1 ±0.9	−1.4 ±0.9	−1.9 ±1.2	−0.5 ±0.4		−2.0 ±1.2
ISOW	−12.3 ±2.7	−9.5 ±2.9	−6.0 ±3.2	−6.8 ±3.9	−8.6 ±2.8		−6.4 ±3.5
DSOW	−14.3 ±4.8	−11.8 ±6.7	−5.3 ±4.1	−10.2 ±7.1	−3.1 ±2.6		−9.8 ±6.1
DWBC	−28.8 ±7.5	−23.4 ±9.8	−12.7 ±7.9	−18.9 ±11.5	−12.3 ±5.2	−32±2	−18.2 ±10.2
zonal extent	170 km	140 km	360 km	75 km	160 km	170 km	250 km

Table 4.2: Mean and standard deviations of northward transport in the DWBC layers. All values, except for the zonal extent, are in Sverdrup, and negative values correspond to southward transport. Estimates for the observed transport variability and zonal extent of the DWBC at 26°N are from Meinen et al. (2013a) and Bryden et al. (2005), and from Toole et al. (2011) for the zonal extent at Line W.

Mean transports in both model and observations are lower at Line W than at 26°N, but standard deviations are higher at Line W. Generally, the mean DWBC transport increases towards the lower latitudes (Table 4.2). The relative standard deviation (the standard deviation divided by the mean) is highest for Line 32 and Line W. This is not surprising since this region is especially dynamically active with high eddy kinetic energy (Richardson, 1983).

At all locations, the individual layer transports are highly correlated. The LSW and ISOW transports show a particulary high correlation (correlation coefficient of $r = 0.77$ at 26°N and $r = 0.94$ at Line W, similar values at the other locations), but there is even a significant correlation between LSW and DSOW (correlation coefficient of $r = 0.51$ at 26°N and $r = 0.66$ at Line W, similar values at the other locations). This indicates that the variability is strongly barotropic, and will be discussed in more detail in Section 4.4.1.

A direct comparison of the observed and modeled DWBC variability at Line W (Figure 4.4) shows that there is no significant correlation between the observed and modeled time series. However, the Line W time series is only four years long, and the two time series exhibit a similar range and frequency of seasonal variability, especially considering the difficulty of defining a narrow boundary current in a complicated region.

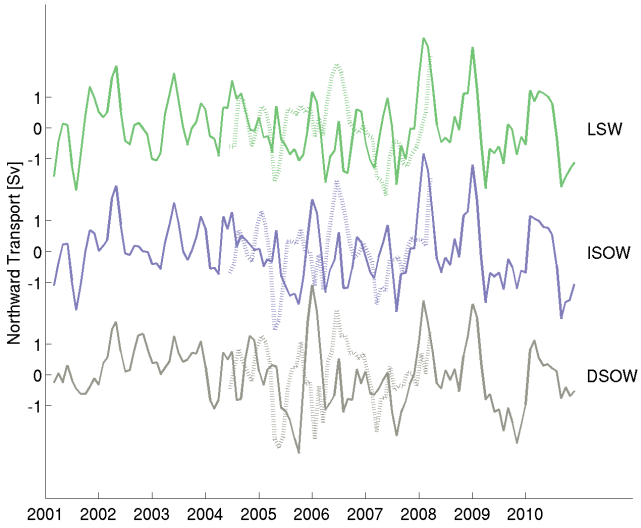

Figure 4.4: Observed (dashed) and modelled (solid) normalized anomaly time series of integrated water mass transports at Line W, smoothed with a three-months running mean. Color coding is LSW: green, ISOW: blue and DSOW: grey.

4.4 Seasonal variability of the DWBC

4.4.1 The seasonal cycle of the DWBC

The spectral density of the monthly DWBC transport time series (Figure 4.5) yields a peak at 12 months for all locations. The peak is most dominant at 26°N and 28°N, probably because the DWBC is best confined at these

latitudes. However, the spectrum indicates that there is a prominent seasonal cycle in the DWBC at all considered locations.

We calculate a seasonal cycle by averaging over each month of the year for the 60−year time series. For the four subtropical latitudes (26°N, 28°N, Line 32 and Line W), the seasonal cycle (Figure 4.6) has a maximum early in the year (January or February) and a minimum in fall (August to October). The seasonal peak to peak amplitude generally decreases towards the higher latitudes: At 26°N the seasonal range is 7.4 Sv. It is slightly higher at 28°N, but decreases to 4.7 Sv at Line 32, 5.4 Sv at Line W and 2.8 Sv at 48°N. As the standard deviations at Line 32 and Line W are not significantly lower than at 26°N and 28°N, this implies that the seasonal signal is more dominant at the lower latitudes, while other short-term variability is more important in the Line W region. At 48°N, the only subpolar latitude, the seasonal cycle has a minimum in February and a maximum in August, 180-degrees out-of-phase with subtropical latitudes.

The seasonal cycle of the DWBC is dominated by the depth-independent (barotropic) component at all locations (Figure 4.7), which we calculate by integrating the depth-averaged velocity over the zonal and depth ranges of the DWBC. The barotropic component of the seasonal cycle is in phase with the baroclinic (depth-dependent) component at 26°N and 48°N. The baroclinic component is obtained by subtracting the barotropic component from the full transport. There is no apparent relation at the other locations.

Taking a broader look at the North Atlantic, the seasonality of the deep transports in the western boundary region is evident in the depth-integrated eddy kinetic energy (EKE) across all latitudes between 10°N and 50°N (Figure 4.8). We calculate the EKE as $EKE = \int u'^2 + v'^2 dz$, where u' and v' denote the zonal and meridional velocity anomalies relative to the full model time series, and we integrate over the the DWBC's density classes. Compared to the zonal and meridional velocities, the EKE shows the strength of the velocities in a

given grid cell, independent of direction and takes both zonal and meridional velocities into account. This is especially useful between 30°N and 45°N, where the DWBC flow is both south- and westward.

Subtracting the mean EKE from the mean EKE in the months of January to March (the months in which the southward transport in the DWBC is at its minimum at 26°N) shows predominantly negative anomalies until 35°N (Figure 4.8a), but predominantly positive anomalies further north. In September to November (the months in which the southward transport in the DWBC is at its maximum at 26°N) EKE anomalies are mostly positive south of 35°N and mostly negative further north. Especially north of 45°N, the negative anomalies in September to November are much weaker than the positive anomalies in January to March, as the minimum at these latitudes occurs earlier in the year in August (Figure 4.6). Overall, the seasonal signal is strongest south of 30°N and north of 45°N, i.e. at the latitudes where the DWBC is narrow and well-confined.

4.4.2 Forcing mechanisms of the seasonal variability

To determine the origin of the DWBC's seasonal cycle, we follow Böning et al. (1991) and investigate the wind stress curl variability in the western part of the basin. For the months of minimum seasonal southward DWBC transport at 26°N (January to March), the wind stress curl in the western North Atlantic has a negative anomaly in the subtropical gyre, but a positive anomaly in the supolar gyre (Figure 4.9a). This reverses for September to November (Figure 4.9b). However, the anomalies from the subpolar latitudes penetrate further south near the western boundary.

For a quantitative analysis and comparison with the DWBC seasonality at the five locations, we therefore integrate the wind stress curl over both the western basin and the boundary. We define the western basin as the part of

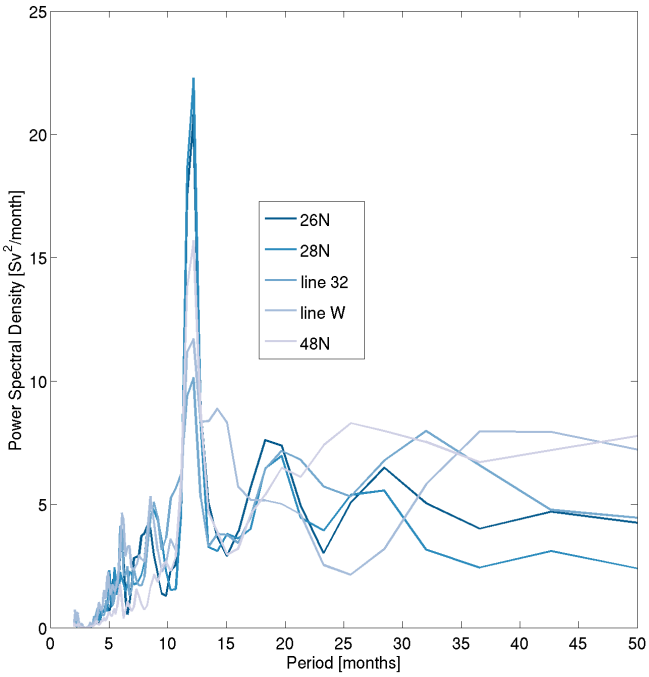

Figure 4.5: Power spectral density of the DWBC transport at the different locations. Spectra are scaled with transport variance at each location.

the basin west of the Mid-Atlantic Ridge. For the boundary wind stress curl, we integrate over the extent of the DWBC. In case of Line 32 and Line W, this means that we integrate along angular lines (Figures 4.2a and c). Note that the resolution of the NCEP wind fields is much lower than the model resolution (0.1° for the model simulation versus 2.5° for the NCEP reanalysis (Kalnay et al., 1996)).

At 26°N and 28°N, the seasonal cycles of the integrated western basin and boundary wind stress curl are almost indistinguishable, although the boundary wind stress curl – like the DWBC – does not show a second maximum in July. Further north, the boundary and western basin wind stress curls differ: At Line 32, the DWBC seasonal cycle shows a better agreement with the negative western basin wind stress curl in the first half of the year, but with the negative boundary wind stress curl in the second half of the year. At Line W and at

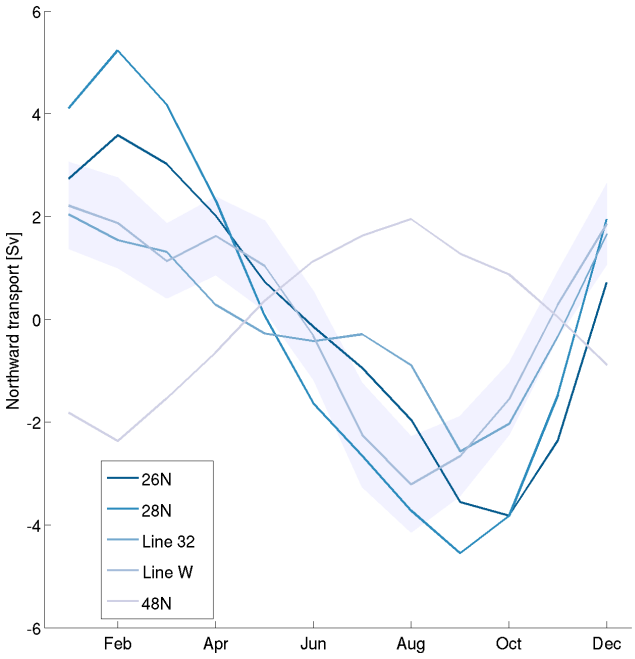

Figure 4.6: DWBC seasonal cycle anomalies with three-months running mean at the different locations. Shading indicates the standard error of the mean for Line W, where the standard deviation is the highest.

48°N, the wind stress curl seasonal cycles at the boundary and in the western part of the basin are out-of-phase by one to two months. At Line W, agreement with the negative western basin seasonal cycle seems slightly better, while at 48°N, the DWBC's seasonal cycle agrees with the negative of the boundary seasonal cycle and not the negative of the western basin seasonal cycle.

We expect that the negative boundary wind stress curl would be better related to the DWBC than the negative western basin wind stress curl for any latitude near 35°N, as the EKE seasonality (Figure 4.8) agrees with the negative boundary wind stress curl, but not the negative western basin wind stress curl in this region. The disagreement between the DWBC's seasonal cycle and the negative boundary wind stress curl at Line W might be due to the low resolution of the wind fields, as the seasonality of the boundary wind stress at Line

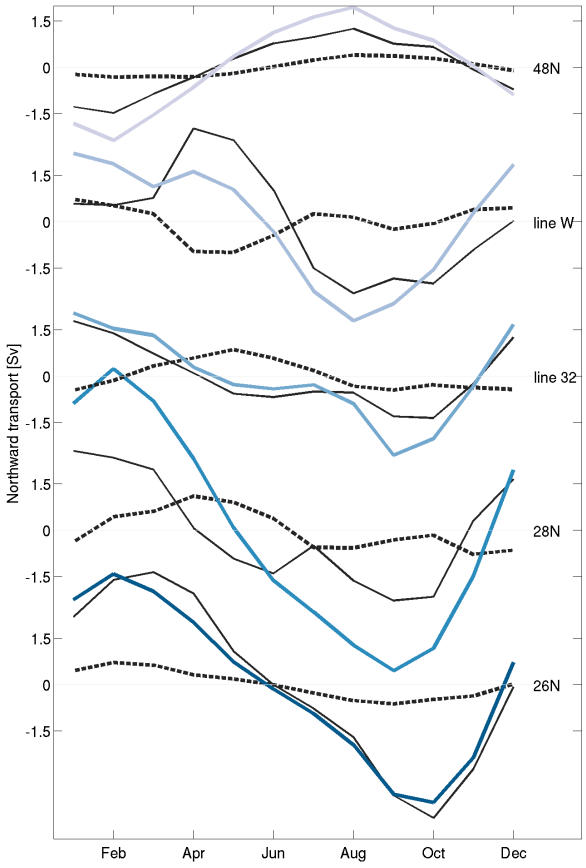

Figure 4.7: Seasonal anomalies of the baroclinic (black, dashed) and barotropic (black, solid) parts of the DWBC at all locations. The full DWBC is shown in blue.

W is very sensitive to the exact limits of the zonal integration, which is not the case at any of the other locations. We conclude that the seasonal cycle of the DWBC originates locally at the western boundary rather than in the western basin, at least north of 35°N.

Unlike the DWBC, we can calculate the boundary wind stress curl at all latitudes. Slightly deviating from the above definition of "boundary", here we calculate a boundary wind stress curl by integrating four degrees of longitude

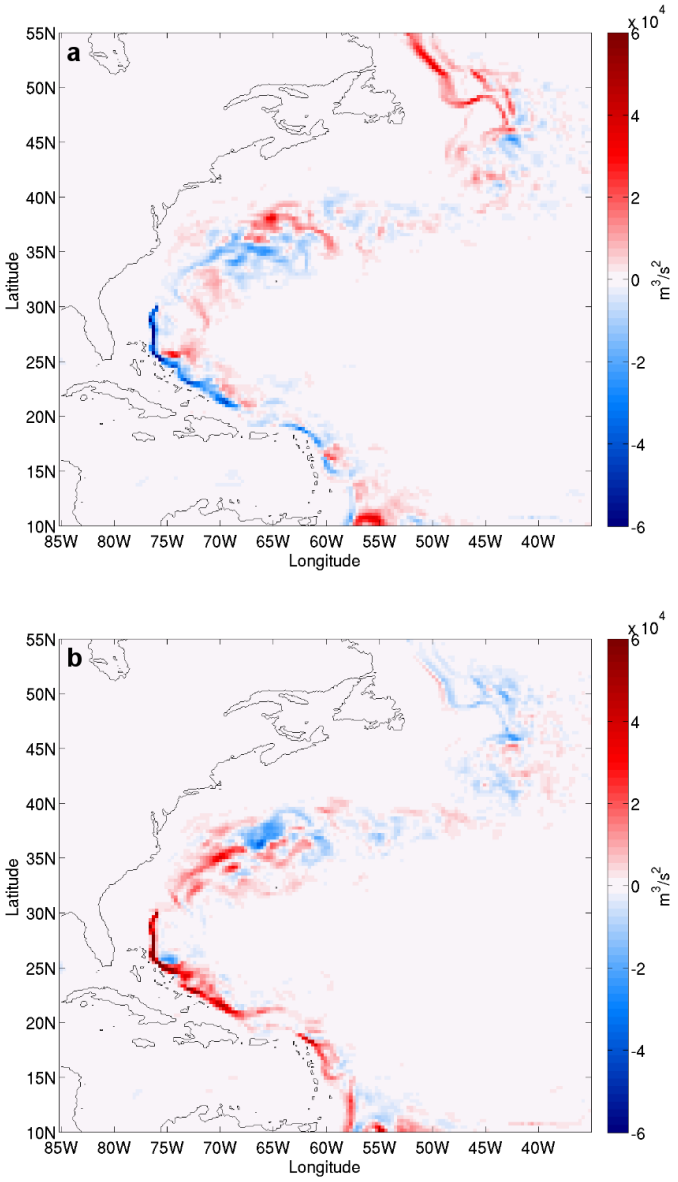

Figure 4.8: Mean anomalies of the depth-integrated eddy-kinetic energy for January to March (a) and September to November (b). Integration is over the DWBC's density classes. Every third data point is shown.

outward from the 1442 meter isobath (between the black lines in Figures 4.9a and b, equal to 400 km at 26°N). In the subtropical gyre, the negative boundary wind stress curl has a maximum in late winter and a minimum in fall (Figure 4.10a). In the subpolar gyre, the seasonality is reversed: The negative

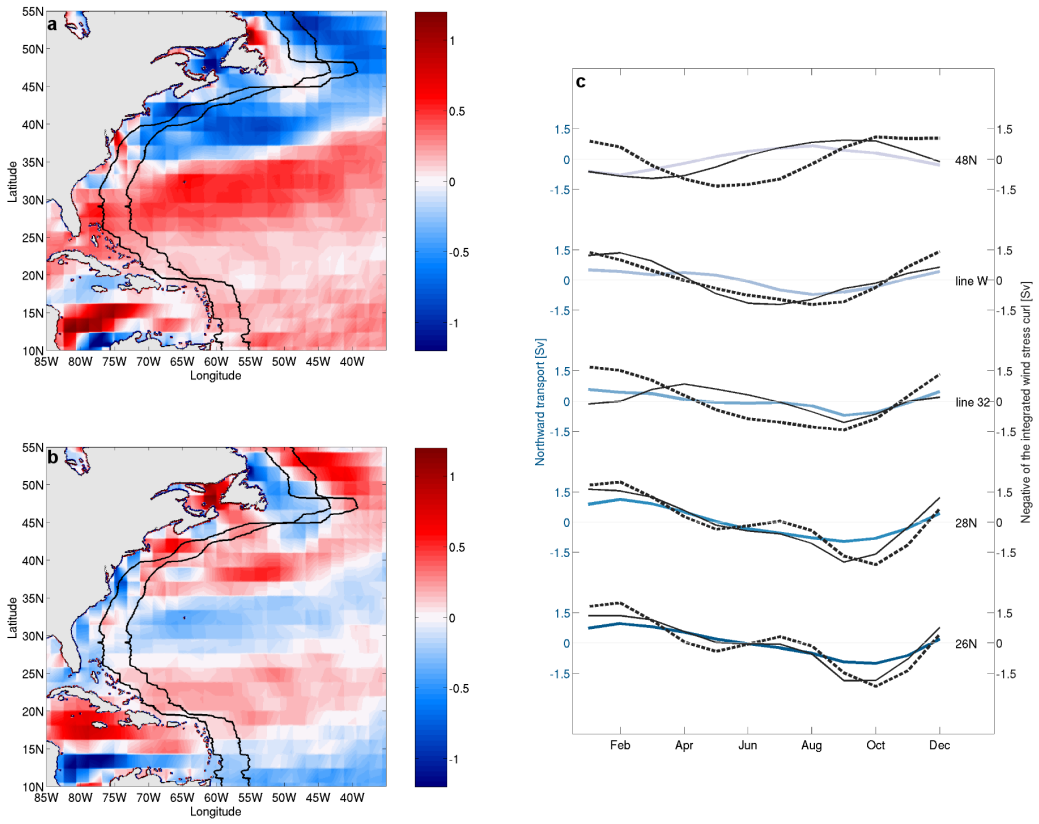

Figure 4.9: Mean anomalies of negative wind stress curl in January to March (a) and September to November (b). The black lines define the boundary, as used for Figure 4.10a. c) Normalized (divided by the standard deviation) seasonal anomalies for the zonally integrated boundary wind stress curl (black, solid) and wind stress curl in the western part of the basin (black, dashed). For Line 32 and Line W, the boundary wind stress curl has been integrated along the angular lines (Figures 4.2a and c). The full seasonal DWBC cycle is shown in blue.

boundary wind stress curl has a minimum in late winter and a maximum in late summer (Figure 4.10a). The relation between the seasonal cycles of the negative boundary wind stress curl and the DWBC (Figure 4.10b) is more robust in the subtropical gyre. We conclude that the DWBC's seasonal cycle, driven by the local wind stress curl, is coherent throughout both the subtropical and subpolar gyre, with opposing seasonality between the two gyres.

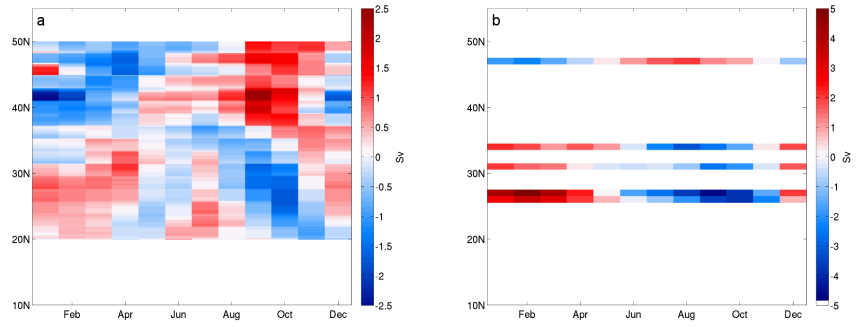

Figure 4.10: a) Hovmoeller plot of seasonal anomalies of the negative of the zonally integrated boundary wind stress curl with the boundary as defined in Figures 4.9a and b, b) the DWBC.

4.5 Relation of the DWBC's seasonal variabiliy to the AMOC

At all analyzed locations, the modeled variability of the DWBC is much higher than the variability of the basin-wide transport: At 26°N, the AMOC has a standard deviation of 3.2 Sv, and the DWBC has a standard deviation of 7.5 Sv (Table 4.2). The time-mean DWBC transport (−28.5 Sv) is also stronger than the time-mean AMOC transport (16.4 Sv). The higher variability suggests that there is a lot more high-frequency variability in the DWBC than in the AMOC, which might obscure any relation between the two transports. Indeed, there is no significant correlation between AMOC and DWBC at any latitude on seasonal timescales, or for either the baroclinic or barotropic component.

The local high-frequency variability averages out if one integrates further eastward, and the variability of the deep transports changes significantly: While the integrated transport below 1000 m still has a significant correlation with the DWBC if one integrates until 500 km offshore ($r = 0.64$, the modeled DWBC at 26°N is, on average, 170 km wide, section 4.3.1.1), an integration until 1000 km only yields a very weak correlation of $r = 0.31$. The correlation becomes insignificant if one integrates out to the Mid-Atlantic Ridge.

Apart from the prevalence of local high-frequency variability in the DWBC, even the western basin transports cannot be used as a proxy for the seasonal variability of the non-Ekman component of the AMOC: Although most of the mean AMOC transport is in the western basin (-15.5 Sv versus -1.4 Sv at 26°N), the magnitude of variability is comparable for both basins, twice as high as the variability of the full basin transport, and the eastern and western basin transports are anti-correlated.

However, all of the transports discussed above have a well-defined seasonal cycle. In the subtropical gyre, the DWBC seasonal cycle has a minimum in southward transport in February and a maximum southward transport in October (Figure 4.6, Section 4.4.1). The western basin seasonal cycle has a minimum in February and a maximum in October at all latitudes (Figure 4.11a). Thus, in the subtropical gyre, the seasonal cycle of the wind stress curl (Figure 4.11b), and thereby the DWBC's seasonal cycle, is consistent with the western basin seasonal cycle. Recirculations and local processes, which cause the high-frequency variability of the DWBC are not permanent and average out in the seasonal cycle of the 60-year model run. The eastern basin seasonal cycle is 180-degree out-of-phase compared to the western basin seasonal cycle (Figure 4.11d).

The seasonal cycle of the non-Ekman component of the AMOC (Figure 4.11c) is shifted by one month compared to the western basin seasonal cycle (Figure 4.11a) due to the influence of the eastern basin seasonal cycle. The seasonal range of the western basin seasonal cycle is twice that of the eastern basin seasonal cycle, and thus the western basin seasonal cycle dominates the variability.

Like the eastern and western basin seasonal cycles, the AMOC seasonal cycle is coherent throughout the North Atlantic (Figure 4.11c, Mielke et al. (2013)). The seasonal cycle of the DWBC, on the other hand, changes sign between the subtropical and the subpolar gyre (Figure 4.11b), due to local wind stress

curl variability. Thus, in the subtropical gyre, the DWBC seasonal cycle is representative of the western basin seasonal cycle, and is thereby related to the AMOC seasonal cycle.

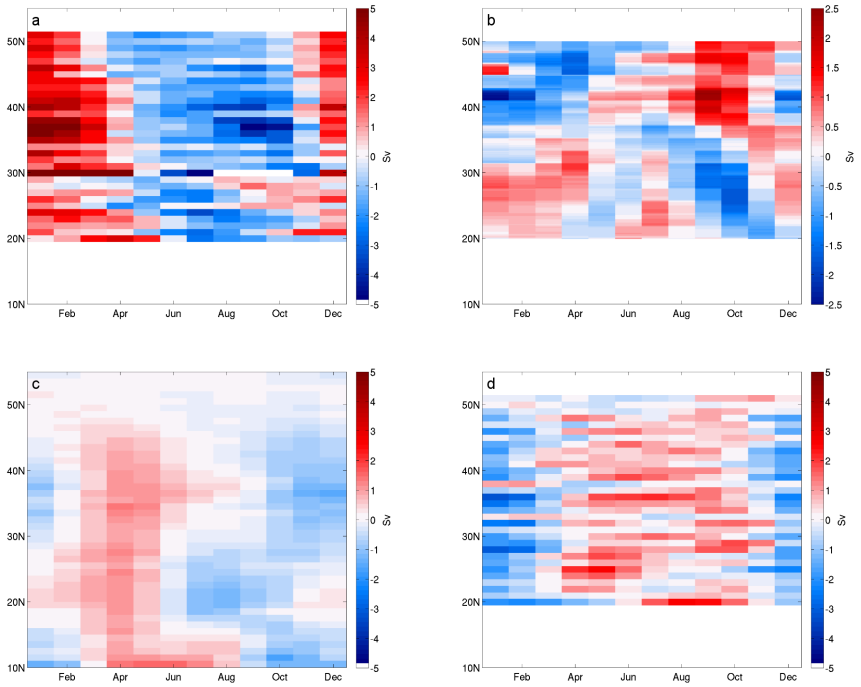

Figure 4.11: Hovmoeller plots of seasonal anomalies for a) integrated the western basin transport below 1000 m, b) the negative of the integrated boundary wind stress curl (same as Figure 4.10a), c) the negative of the non-Ekman component of the AMOC, and d) integrated eastern basin transport below 1000 m.

4.6 Discussion

The purpose of this study is to investigate the seasonal variability of the DWBC, which is to date not clear from observations due to the shortness of the available time series (Toole et al., 2011, Meinen et al., 2013a). Overall, the model used here appears to reproduce the "real ocean" DWBC in terms of structure, mean and range and frequency of variability at the locations where comparisons between observations and model are possible (26°N and

Line W), although the observational time series are too short for a quantitative comparison of the variability. Both the mean and the standard deviation of the modeled DWBC decrease toward the higher latitudes, consistent with the existence of interior pathways (Gary et al., 2011) and in agreement with observations at 26°N (Meinen et al., 2013a) and Line W (Toole et al., 2011).

A spectral analysis of the model time series reveals a prominent seasonal cycle in the model DWBC at all latitudes, which is largely undisturbed by short-term fluctuations. Again, observational time series are too short to meaningfully calculate a seasonal cycle, although Toole et al. (2011) suspect a seasonal cycle in the Line W data. However, a previous model study by Böning et al. (1991) finds a seasonal cycle in the DWBC at 26°N. Böning et al. (1991) link the DWBC seasonal cycle to the negative western basin wind stress curl. Here, we find the DWBC's seasonal cycle to be related to the negative western boundary wind stress curl, defined as the wind stress curl directly above the DWBC. The distinction between western basin and boundary wind stress curl is especially important at the gyre boundary and in the subpolar gyre. Also, the model used by Böning et al. (1991) has a lower resolution, so there would be less distinction between the boundary and the interior than in the model used in this study.

The DWBC's seasonal cycle is coherent between the four investigated subtropical locations, but the seasonal cycle at the one subpolar latitude (48°N) is 180-degree out-of-phase. The eddy kinetic energy and wind stress curl patterns, however, suggest that the seasonal cycle at 48°N is representative of the seasonal cycle in the subpolar gyre. Thus, the seasonal cycle of the DWBC appears to be coherent throughout both the subtropical and the subpolar gyre, but not across the gyre boundary. As the DWBC seasonal cycle is related to the wind stress curl, the correct representation of the wind stress curl near the boundaries will be important in future ocean modelling.

The DWBC is not directly correlated with the basin-wide transport on seasonal

timescales. This is partly due to local recirculations and other local short-term variability, which cause the variability of the DWBC to be much higher than the variability of the basin-wide transport, both in our model and in observations (Meinen et al., 2013a). Observational studies at 26°N have attributed the higher mean and variability of the DWBC to recirculations outside of the range of moorings (Johns et al., 2008), local processes in the western basin and deep transports in the eastern part of the basin (Meinen et al., 2013a) and baroclinic Rossby waves (Kanzow et al., 2008). The limited range of moorings is clearly not an issue for a model study, and we find that the variability of the DWBC is mostly barotropic, so baroclinic Rossby waves do not have a major influence on the variability.

The DWBC seasonal cycle agrees with the western basin transport seasonal cycle at all analyzed locations except for 48°N. The disagreement at 48°N can be partially understood by a permanent recirculation east of Flemish Cap (Section 4.3.1.3 and Figure 4.2). If one includes this recirculation in the DWBC, the seasonal cycles of DWBC and western basin transport agree for the second half of the year. Although recirculations exist at other latitudes as well, none of them are permanent and thus average out over the course of the model run. Another possible explanation is that the AMOC seasonal cycle might be incorrectly represented in the model in the subpolar gyre, which would explain the phasing discrepancies in the non-Ekman component of the AMOC between model and observations at 41°N (Mielke et al., 2013). Unfortunately, calculating a DWBC at 41°N is not feasible because the DWBC is not confined at this latitude, but the wind stress curl pattern suggests that the seasonal cycle at 41°N would be equivalent to the seasonal cycle at 48°N. Eventually, longer observational time series of the AMOC and the boundary currents in this area are needed.

The seasonal cycle of the full basin-wide AMOC is a combination of the eastern basin seasonal cycle and the western basin seasonal cycle. The western basin seasonal cycle agrees with the DWBC seasonal cycle in the subtropical gyre.

The eastern basin transport is anti-correlated with the western basin transport, resulting in a shift in seasonal cycle of the full basin-wide AMOC by one month compared to the western basin seasonal cycle. This agrees with the findings from Kanzow et al. (2008) for 16°N, and explains why the deep western boundary current alone, or even the western basin transport cannot explain the seasonality of the full AMOC.

The question whether modulations in the AMOC seasonal cycle can be inferred from changes in the DWBC or the western basin seasonal cycle requires further analysis. Although the deep basins are separated by the Mid-Atlantic Ridge at the subtropical latitudes, the anti-correlation between the two transports indicates that they are not unrelated. Changes in the western basin seasonal cycle might therefore be compensated by the eastern basin, and thus not be reflected in the AMOC seasonal cycle. The AMOC and the DWBC might show a higher correspondence on longer timescales, where the DWBC variability is not dominated by high-frequency fluctuations.

4.7 Summary and Conclusions

In this study, the seasonal variability of the DWBC and its relation to the basin-wide transport is investigated in a high-resolution ocean general circulation model. We define a model DWBC at five locations from 26°N to 48°N based on a comparison of modeled and observed temperature and salinity data and an analysis of the local velocity fields. The modeled and observed DWBC exhibit a similar structure, mean transport and range and frequency of seasonal variability at both 26°N and Line W. The model is thus able to adequately represent the DWBC. From our analysis, we conclude:

- The DWBC has a well-defined seasonal cycle. In the subtropical gyre, the southward transport is strongest in fall and weakest in late winter. In

the subpolar gyre, the maximum occurs in late winter and the minimum occurs in late summer.

- The DWBC's seasonal cycle is mostly barotropic and forced by the local wind stress curl.
- In the subtropical gyre, the DWBC's seasonal cycle agrees with the western basin seasonal cycle, which is anti-correlated with the eastern basin seasonal cycle.
- The DWBC might be used as a proxy for modulations of the western basin seasonal cycle.

Acknowledgements

We thank Eleanor Frajka-Williams and Jochem Marotzke for helpful discussions, and Irina Fast and Helmuth Haak for their help with the model output and the interpolation. The STORM/NCEP simulation is part of the German STORM consortium project and has received financial support from the Institute of Coastal Research of the Helmholtz Zentrum Geestacht and the Alfred Wegener Institute for Polar and Marine Research. Results are available to the scientific community (https://verc.enes.org/storm/results/data). Data from the RAPID-WATCH/MOCHA monitoring project are funded by the Natural Environment Research Council (NERC) and National Science Foundation (NSF) and are freely available from www.noc.soton.ac.uk/rapidmoc. Data from the Line W array are available from http://www.whoi.edu/science/PO/linew/download_data.php. This work is supported by the International Max Planck Research School on Earth System Modelling (IMPRS-ESM), Hamburg (CLM), the Cluster of Excellence CliSAP (EXC177), University of Hamburg, funded through the German Science Foundation (DFG) (JB), and the U.S. National Science Foundation (JMT, SFG).

5 Decadal covariability of the DWBC and the AMOC in the North Atlantic [1]

Abstract

We investigate whether the Deep Western Boundary Current (DWBC) and Atlantic Meridional Overturning Circulation (AMOC) are related on decadal timescales by analysing results from a high-resolution general ocean circulation model. In our analysis, we find that the DWBC exhibits multidecadal oscillations, which are mostly coherent throughout the North Atlantic, although the DWBC's variability is susceptible to local recirculations. The variability of the DWBC on decadal timescales is modulated by the local wind stress curl variability, particularly in the subtropical gyre. This suggests that the decadal variability of the DWBC can be inferred from the local wind stress curl, enabling an estimate of its variability at latitudes where observations are not available and on longer timescales than currently possible from continuous observations. The decadal AMOC and DWBC are covariable, but the relationship is non-stationary, and depends on the relative phasing of the boundary and basin-interior wind stress curl: Opposing behavior of the wind stress curl

[1] C. Mielke, S. Gary, and J. Baehr (2013), Decadal covariability of the DWBC and the AMOC in the North Atlantic, in preparation for submission to *Geophysical Research Letters*.

between the boundary and the basin leads to opposing behavior for the AMOC and the DWBC. Our results therefore indicate that observations of the DWBC cannot easily be used as a shortcut to obtain an estimate of the decadal AMOC variability.

5.1 Introduction

The Deep Western Boundary Current (DWBC) is one of the major export pathways of water masses that form through convection at the high latitudes of the North Atlantic (e.g. Lozier (2012)). The DWBC is a key component of the Atlantic Meridional Overturning Circulation (AMOC), which has a major influence on the climate in North America and Europe (Sutton and Hodson, 2005), and is expected to decline in response to anthropogenic forcing (IPCC, 2013). Recent model studies, for example, relate the decadal AMOC variability to wind forcing and the North Atlantic Oscillation (NAO, Biastoch et al. (2008) and references therein), but the results to date cannot be verified against observations, as continuous measurements of the AMOC have only recently become available (Cunningham et al., 2007, Willis, 2010).

Understanding the linkage between AMOC and DWBC would greatly enhance our current knowledge, as the decadal variability of the DWBC has been the subject of a number of observational studies over the past years. The decadal variability of transports in the Labrador and Irminger Seas has been inferred from hydrographic sections in the area (Bacon, 1998, Kieke and Rhein, 2006). Moorings that provide continuous measurements exist, among others, in the Labrador Sea (Dengler et al., 2006, Fischer et al., 2014a), in the Denmark Straits (Jochumsen et al., 2012), and newer arrays also measure the DWBC further downstream (Toole et al., 2011, Meinen et al., 2013a), but the available time series are to date too short to investigate the decadal variability or meridional coherence.

Most of the existing studies on the long-term DWBC variability focus on the higher latitudes, where a connection with convection events and water mass formation rates can often be established (e.g., Kieke and Rhein (2006), Sarafanov et al. (2010) for observational studies, and Böning et al. (2006) for a model study), and anomalies are expected to propagate southward through fast coastally trapped waves and eventually by advection (Johnson and Marshall, 2002, Zhang, 2010, Elipot et al., 2013). Nevertheless, it is at present not clear how the decadal variability of the DWBC at the subarctic latitudes relates to the variability of the DWBC at the lower latitudes.

Like the DWBC, the AMOC has been linked to buoyancy forcing (Böning et al., 2006, Biastoch et al., 2008), but the coherent signal weakens towards the lower latitudes, where it is masked by local wind stress variations (Jayne and Marotzke, 2001, Böning et al., 2006) and eddy variability (Biastoch et al., 2008). Thus, although both AMOC and DWBC are likely related to the deep water formation in the subarctic, their relationship at latitudes further south remains unclear. On seasonal timescales, a model study shows that the relationship between the AMOC and the DWBC is aliased by short-term fluctuations, but these average out in the seasonal cycle (Chapter 4), and are possibly even less important on longer timescales. Furthermore, interior pathways may also be relevant for the conduit of deep waters from the higher latitudes (Bower et al., 2009, Gary et al., 2011, 2012).

The aim of this study is therefore to understand the variability of the DWBC on decadal timescales, and to investigate whether it allows conclusions about the long-term AMOC variability. We therefore evaluate the decadal variability of both the DWBC and the AMOC in a high-resolution NCEP-forced ocean general circulation model. The DWBC is defined in density classes, based on a comparison of observed and modeled temperature, salinity and velocity fields, and has been shown to reproduce the observed mean, structure and temporal variability of the DWBC on seasonal time scales (Chapter 4).

The manuscript is organized as follows: In section 5.2, we explain the model and the employed methods. Then we investigate the decadal DWBC variability and its driving mechanisms (Section 5.3), and its relation to the decadal variability of the basin-wide transport (Section 5.4). A discussion of the results and conclusions (Section 5.5) follow.

5.2 Model and methods

The model used in this study is the Max-Planck-Institute ocean model (Marsland et al., 2003, Jungclaus et al., 2006) in the high-resolution STORM setup (von Storch et al., 2012) with a horizontal resolution of 0.1° and 80 vertical levels ($10-280$ m thickness). After a 25-year spin-up phase using the German Ocean Model Intercomparison Project forcing, the simulation is forced by 6-hourly NCEP wind stress (Kalnay et al., 1996). The resulting run covers the time period 1948–2010. Velocity, temperature and salinity are output daily, but we use monthly averages for our analysis. Sea surface salinity is relaxed to the Polar Science Center Hydrographic Climatology (Steele et al., 2001), and the AMOC maximum is located at about 35°N and 1000 m depth.

Following observational practice (e.g., Yashayaev (2007), van Sebille et al. (2011)), we define the DWBC in density classes described in more detail in Chapter 4. Thus, we first determine the density classes for the three DWBC water masses, Labrador Sea Water (LSW), Iceland-Scotland Overflow Water (ISOW) and Denmark Strait Overflow Water (DSOW), by comparing temperature and salinity properties at the latitudes where observations are available (26°N and Line W). We then analyse the horizontal and vertical velocity field to find suitable locations for the DWBC. Particularly between 35°N and 45°N, the DWBC is not very confined or obscured by recirculations, rendering a meaningful DWBC calculation impossible. As observations are available at 26°N and Line W, we include latitudes that are dynamically similar in our

analysis. In the case of Line W, this means that we have to adjust the nominal latitude for a comparable latitude in the model. Even after this adjustment, the computation of a model DWBC requires a careful analysis of the velocity field at each time step to account for non-permanent recirculations. We therefore restrict the computation to four subtropical and one subpolar location (Chapter 4): 26°N, 28°N, an angular line at about 32°N (hereafter Line 32), a line roughly equivalent to the observational Line W and 48°N (Figure 5.1).

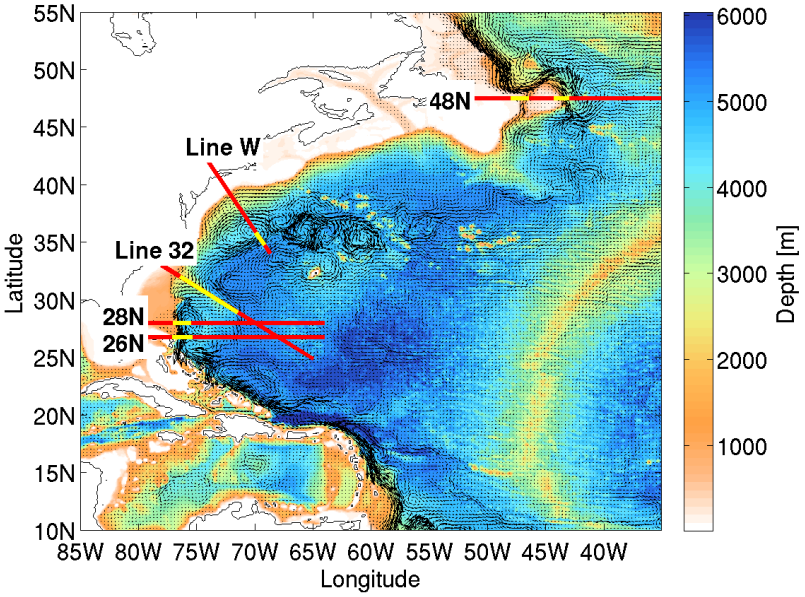

Figure 5.1: Bathymetry of the modeled western North Atlantic and DWBC velocity vectors. Vectors are computed by depth-integrating the zonal and meridional velocities over the density classes of the DWBC, and every third vector is shown. Locations where the DWBC is calculated in the model are marked by red lines. The yellow part indicates the extent of the mean DWBC at each location.

We calculate the DWBC time series from the monthly averages of temperature, salinity and zonal and meridional velocity. The AMOC is defined as the maximum of the overturning streamfunction, which is calculated directly from the model velocities. Then we smooth both time series with a ten-year running mean. This filtering reduces the usable length of the time series. In the following, the term "decadal" refers to the ten-year smoothed time series.

5.3 Decadal variability of the DWBC

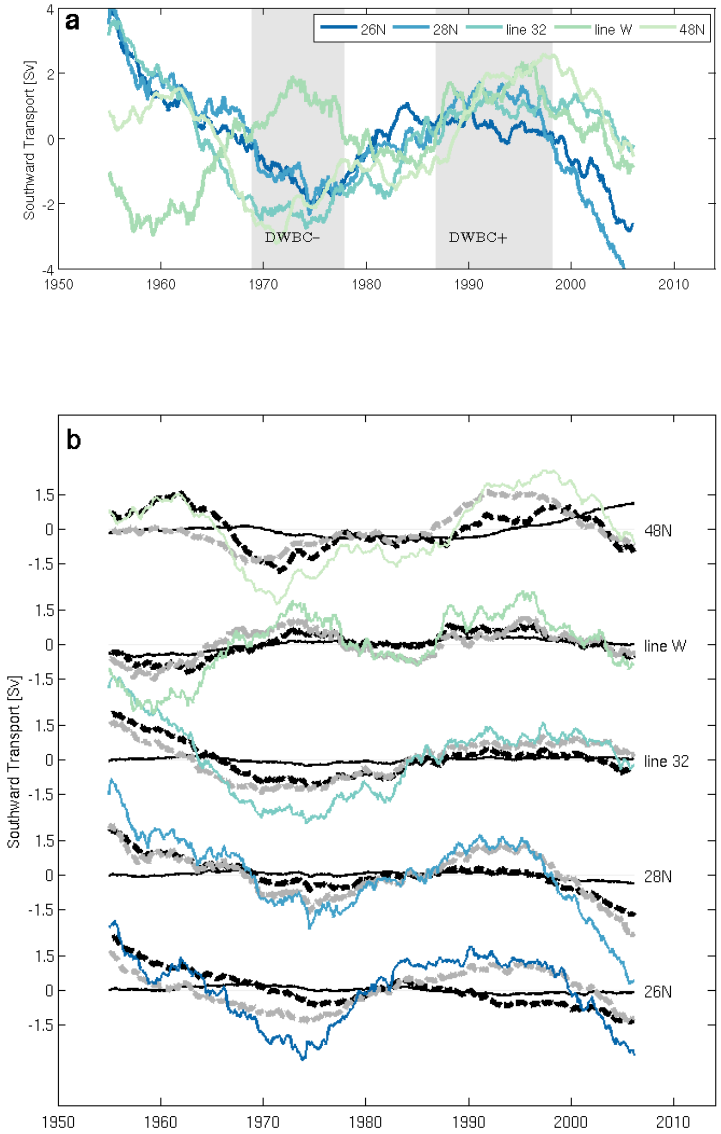

Figure 5.2: a) Anomaly time series of the southward DWBC transport. The shading illustrates the defined time periods (see text). b) Anomalies of the LSW (black), ISOW (black, dashed) and DSOW transport components (grey, dashed) and the full southward DWBC (blue-green).

The DWBC shows multidecadal variability at all investigated locations (Figure

5.2a). The mean southward transport at 26°N is −26 Sv and decreases towards the higher latitudes (Chapter 4). At all locations, most of this transport is in the ISOW and the DSOW, with a smaller contribution from the LSW. For example, at 26°N, the LSW transport contributes only −2 Sv, while ISOW and DSOW transports are close to −12 Sv each. At all locations, the standard deviation of the DSOW is about twice that of the ISOW transport, which in turn is higher than the standard deviation of the LSW transport. The standard deviation of the full transport, as well as the individual water masses, is highest at the mid-latitude locations, Line 32 and Line W.

At all locations except Line W, to which we will return later, the southward transport decreases from the beginning of the time series until the mid-1970s, then increases until the 1990s, after which it decreases until the end of the model time series (Figure 5.2a). At 26°N and 28°N, the southward transport in the DWBC is slightly weaker at the beginning of the time series at its end, while the southward transport at Line W and 48°N is slightly stronger. There is no change at Line 32. We can at present not determine whether this increase and decrease are part of longterm oscillations. The detrended DWBC at 26°N is significantly correlated at the 99% level with the detrended DWBC transports at 28°N (0.87), Line 32 (0.81) and 48°N (0.64). The correlations of the 26°N transports with the Line 32 and 48°N transports increase slightly if 26°N lags by 2.5 years (line 32, 0.87) or 4.5 years (48°N, 0.71).

The Nordic Seas Overflow Waters transports (ISOW and DSOW) are highly with each other correlated at all locations (Figure 5.2b). The Labrador Sea Water (LSW) transport is correlated with both the ISOW and DSOW transports at all locations except for 48°N, where there is no relation between the LSW and the ISOW and DSOW transports. The high correlation between the different water mass transports indicates that the variability of the decadal DWBC at every individual location is mostly uniform over the entire depth range of the DWBC.

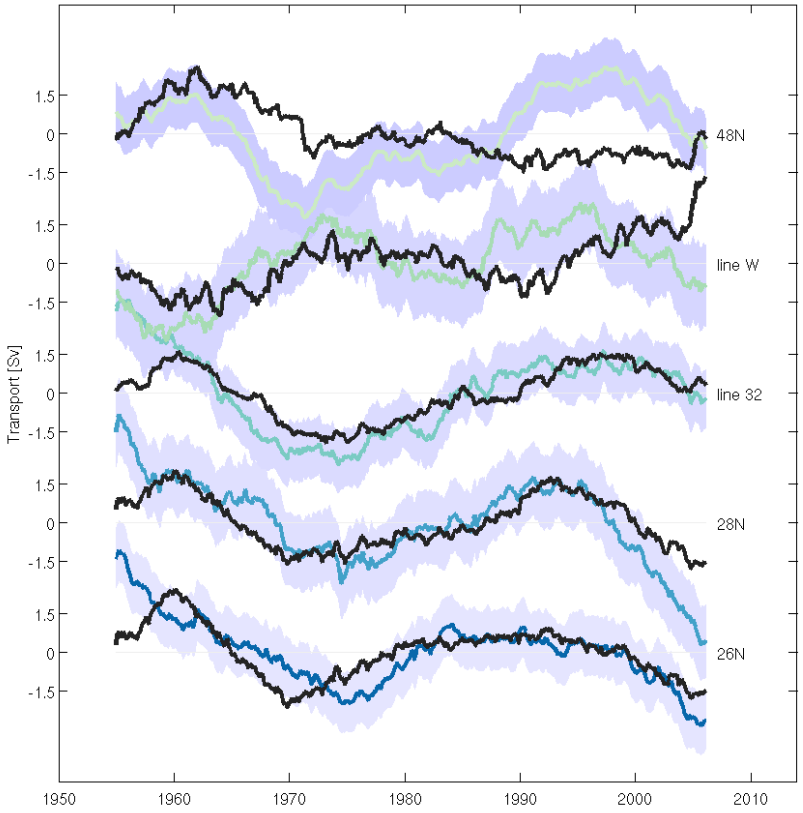

Figure 5.3: Normalized by the standard deviation anomalies of the (northward) integrated boundary wind stress curl (black) and the full (southward) DWBC (blue-green). Shading shows the standard error of the mean for the DWBC. Error bars for the integrated boundary wind stress curl are of similar magnitude.

This relationship also holds on seasonal timescales, where the variability of the DWBC is driven by the local wind stress curl variability, particularly in the subtropical gyre (Chapter 4). Similarly, on decadal timescales, the DWBC variability is strongly related to the negative boundary wind stress curl variability at the three four southern locations (Figure 5.3). Here, "boundary wind stress" means the wind stress directly above the DWBC. In the case of Line 32 and Line W, this means that we integrate along angular lines (Figure 5.1). The relation between the DWBC and the negative of the local wind stress curl

is weaker at 48°N, especially towards the end of the time series. Hence – as on seasonal timescales – the decadal DWBC variability appears to be forced locally at the western boundary, particularly in the subtropical gyre. The sign differs from the classical Sverdrup relation (e.g. Olbers et al. (2012)), as positive wind stress curl anomalies lead to reduced northward transport.

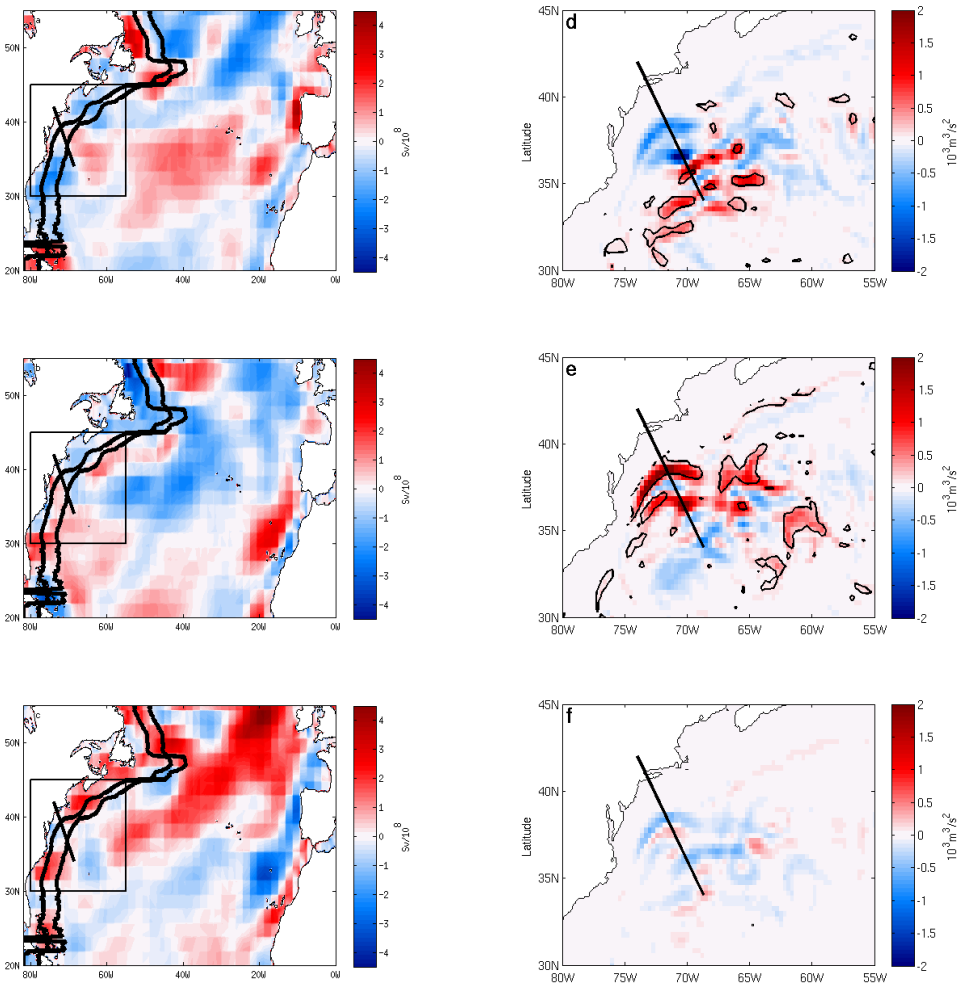

Figure 5.4: Left panels: Mean wind stress curl anomaly in the North Atlantic for a) DWBC−, b) DWBC+ and c) the remainder of the time series. The area between the black lines is the "boundary", as defined for the purpose of Figure 5.5. The box indicates the area that is zoomed-in on in the right panels. Right panels: Mean eddy kinetic energy anomaly in the North Atlantic for d) DWBC−, e) DWBC+ and f) the remainder of the time series. Black contours show the one sigma level, and the thick black line is the modeled line W.

For a broader look at the wind stress curl variability throughout the North

Atlantic, we define two time periods with differing DWBC behavior (shading in Figure 5.2a). For DWBC− (1968−1977), the DWBC shows a negative anomaly at all locations except for Line W, and the boundary wind stress curl anomaly is negative, except for a few latitudes around 38°N and again around 45°N (Figure 5.4a). For DWBC+ (1986−1998), the DWBC shows a positive anomaly at all locations, and the boundary wind stress curl anomaly is positive until about 40°N, and mostly negative further North, although there are a few latitudes with positive values near 45°N again (Figure 5.4b). For the remainder of the time series, the boundary wind stress curl anomaly shows no clear patterns (Figure 5.4c), as expected since the time period includes both positive and negative DWBC anomalies.

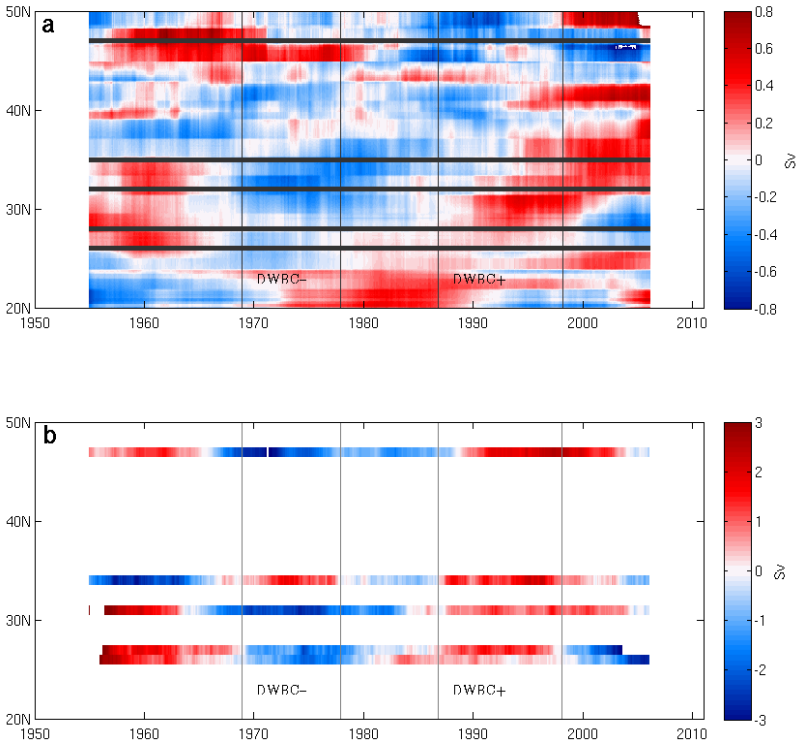

Figure 5.5: Hovmoeller plots of a) the integrated decadal wind stress curl, zonally integrated over the boundary region b) the decadal DWBC.

We have calculated the DWBC at five individual locations, but the wind stress curl is known for the entire North Atlantic. It is therefore possible to describe

the DWBC variability at every latitude by calculating a time series for the boundary wind stress curl. We calculate a boundary wind stress curl by integrating 4 degrees of longitude outward from the 1442 meter isobath (black lines in the left panels in Figure 5.4). Note that this definition differs slightly from the above definition of "boundary", where the wind stress curl is integrated over the extent of the DWBC. But the results do not differ appreciably at the locations where we have defined a DWBC and calculated a boundary wind stress curl directly above the DWBC.

The decadal variability of the boundary wind stress curl is coherent between 25°N and 35°N (Figure 5.5a), and is in this region likely representative of the DWBC variability (Figure 5.5b). North of 35°N, the decadal variability of the boundary wind stress curl is more varied both temporally and spatially, although it is still coherent across a smaller range of latitudes (e.g., 39°N to 43°N). However, it should be noted that the resolution of the NCEP wind fields is much lower than the model resolution (0.1° for the model simulation versus 2.5° for the NCEP reanalysis, (Kalnay et al., 1996)), and this may artificially increase the coherence north of 35°N.

The DWBC at Line W differs from the transport at the other locations in the first half of the model run, until the 1980s, including DWBC−. While the DWBC at the other locations decreases towards its minimum in the 1970s, the DWBC at Line W increases and has a maximum in the 1970s. In the second half of the time series, the DWBC is coherent between all locations.

Differences between DWBC− and DWBC+ are apparent in the velocity field in the area: Although the DWBC at Line W has virtually the same mean value during DWBC− and DWBC+, the velocity or eddy-kinetic energy fields in the area differ considerably (Figure 5.4d and e) with smaller velocities close to the coast during DWBC−. For all time periods, the calculated mean DWBC is located at roughly the same distance offshore, but is much better defined for DWBC+ and the remainder of the time series (Figure 5.4f) than for DWBC−.

However, the main reason for the different behavior of DWBC at Line W is the positive wind stress curl anomaly around 38°N during DWBC− (Figure 5.4a), which is also evident in the integrated boundary wind stress time series (Figure 5.3).

5.4 The AMOC's relation to the DWBC

The AMOC has a relatively constant mean transport of 18 Sv from 20°N to 35°N, north of which it decreases towards the higher latitudes, reaching 12 Sv at 50°N. The variability of the AMOC is characterized by multidecadal oscillations (Figures 5.6a), and the standard deviation is highest around 37°N. Starting from the beginning of the model run, the AMOC at all latitudes decreases until the 1960s, then increases until the 1980s, after which it decreases until the end of the model run (Figure 5.6b). The AMOC shows both a lower mean transport and a lower standard deviation than the DWBC, but both quantities decrease towards the higher latitudes and show the highest variability between 35°N and 50°N.

Contrary to the DWBC, the AMOC shows a (slightly) positive anomaly for both DWBC− and DWBC+ (Figure 5.6a), so AMOC and DWBC are out-of-phase for DWBC−, except at Line W, but in-phase for DWBC+ at all locations (Figure 5.6d). The wind stress curl patterns at the western boundary and the basin-interior reflect this relation: For DWBC−, the wind stress curl anomaly at the western boundary is negative at most latitudes, while there are positive anomalies in the basin-interior between 25°N and 40°N (Figure 5.4a). For DWBC+, the AMOC and the DWBC are in-phase at all locations. Here, the wind stress curl has positive anomalies at the western boundary until 35°N and mostly negative anomalies further north (Figure 5.4b). The wind stress curl anomaly is mostly positive in the basin interior until 35°N and negative further north.

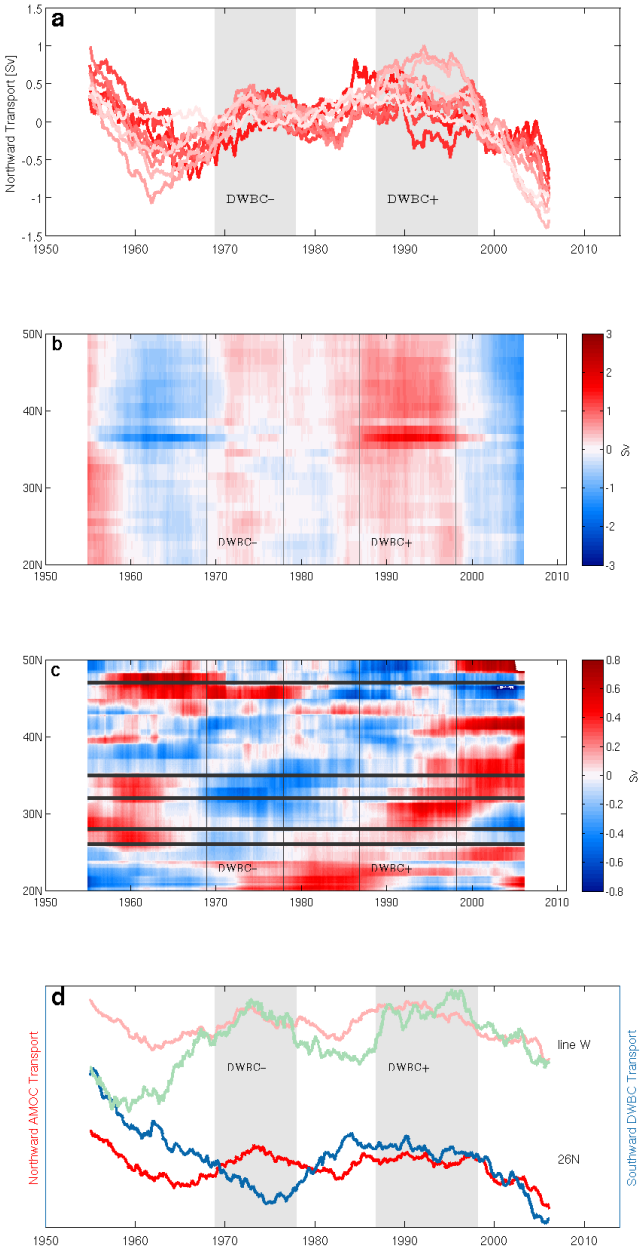

Figure 5.6: Anomaly time series (a) and Hovmoeller plot (b) of the decadal AMOC. Lighter colors in a) correspond to higher latitudes. (c) integrated decadal boundary wind stress curl (same as Figure 5.5a). (d) Normalized by the standard deviation anomaly time series of the negative of the decadal AMOC (red) and the decadal DWBC (blue-green) at 26°N and 35°N/line W. Shading in (a) and (d) illustrates the defined time periods (see text).

Thus, in contrast to DWBC−, the wind stress curl mostly agrees between the western boundary and the basin interior for DWBC+. As a result, the AMOC and the DWBC are in-phase for this time period as well. The remainder of the time series shows strong positive anomalies in the basin interior north of 40°N, but no clear patterns at the western boundary or in the basin interior, as both the AMOC and the DWBC show positive as well as negative anomalies.

The relationship of the AMOC and the DWBC in the subtropical gyre thus depends on the relation of western boundary and basin interior wind stress curl, as the AMOC depends on the basin interior and the DWBC depends on the western boundary wind stress curl. The AMOC and the DWBC are therefore only in phase when the wind stress curl at the western boundary and in the basin interior are in phase.

5.5 Discussion of results and conclusions

Excluding Line W, in the STORM model, we find higher DWBC transports in the 1950s and 1960s, a transport minimum in the mid-1970s and again higher transports towards the late 1990s. Long-term observational studies of the DWBC only exist at the higher latitudes, and report different decadal variability: Bacon (1998) uses data from 22 hydrographic sections between 43°N and 60°N in the western subpolar North Atlantic, and finds low transports in the 1950s, 1960s and again in the 1990s and high transports in the 1970s and 1980s. Using a different set of sections, Kieke and Rhein (2006) mostly confirm this, although in both studies, the true variability of the DWBC in the Labrador and Irminger Seas might be aliased by short-term variability due to the snapshot nature of the hydrographic sections (Kieke and Rhein, 2006). In contrast to the observational results, in their model study, Böning et al. (2006) find stronger southward transport in the DWBC at 53°N in the late 1970s and early 1990s.

The decadal AMOC variability has also been investigated in previous model studies. Both Böning et al. (2006) and Biastoch et al. (2008) find similar decadal AMOC variability, with maximum transport in the 1990s. Our slightly longer model run reveals that the maximum in 1990s is not indicative of a longterm upward trend. Rather, the AMOC was similarly strong in the 1950s and is at a minimum in the mid-2000s. From our time series, we thus cannot conclude that there is any longterm trend in either the AMOC or DWBC in the model.

While the DWBC is related to the negative wind stress curl at the western boundary, previous studies have found that the AMOC's variability depends on the larger-scale atmospheric conditions: Böning et al. (2006) and Biastoch et al. (2008) relate the decadal AMOC to convection events, which are connected to the NAO (Eden and Willebrand, 2001), and we also find a correlation between the NAO and the AMOC in our model run (not shown, correlation coefficient of 0.55). AMOC anomalies then propagate southward via fast boundary waves (Getzlaff et al., 2005), and are the main source of decadal variability even in the subtropics, even though they grow weaker further south due to aliasing from local wind stress variability (Jayne and Marotzke, 2001, Böning et al., 2006). Signals from the Nordic Seas are also expected to propagate southward within the DWBC (Elipot et al., 2013), and Böning et al. (2006) link the DWBC at 53°N to LSW formation. But our results suggest that these signals are mostly overlayed by local wind-driven fluctuations further south, in agreement with (Biastoch et al., 2008).

The relation between AMOC and DWBC thus depends on the atmospheric conditions in the North Atlantic basin interior and the western boundary: If the wind stress curl anomalies in the basin interior and at the western boundary are of opposite sign, the DWBC and the AMOC show opposing behavior as well. Hence, the DWBC can only be used as a direct proxy for the AMOC on decadal timescales if the wind stress curl is in phase between the basin interior and the western boundary.

Both the AMOC and the DWBC are coherent over a wide range of adjacent latitudes in the North Atlantic on both decadal and seasonal timescales (Böning et al. (2006), Biastoch et al. (2008), Bingham et al. (2007), Lozier et al. (2010), Mielke et al. (2013) and Chapter 4), and the DWBC is related to the boundary wind stress curl on both timescales. Consequently, a combination of knowledge about the basin-interior transport from Argo and altimeter data (Willis, 2010) and knowledge about the deep transports at the western boundary from the local wind stress curl variability could provide an improved picture of variability of the overturning circulation in the North Atlantic.

6 Summary and Conclusions

To evaluate the variability and latitudinal dependence of the Atlantic meridional overturning circulation (AMOC) and its deep western return flow, the Deep Western Boundary Current (DWBC), I have jointly analysed the recently available observations at 26°N, Line W (about 38°N) and 41°N, and compared them to results from a 60-year high-resolution, wind-forced ocean simulation. In addition, I have analysed the variability of the meridional heat transport in model and observations. In the following, I will first briefly describe the model I used and the employed methods before presenting the main results of the thesis.

6.1 Model and methods

6.1.1 Computing AMOC, DWBC and heat transport in the model

The model results stem from a high-resolution run with the Max-Planck-Institute ocean model (Marsland et al., 2003, Jungclaus et al., 2006, von Storch et al., 2012). The horizontal resolution is 0.1°, and there are 80 vertical levels ($10 - 280$ m thickness). The model is forced with $6-$hourly NCEP reanalysis data (Kalnay et al., 1996) and covers the time period $1948-2010$ (von

Storch et al., 2012). The AMOC maximum is located at about 35°N and 1000 m depth (Figure 1.1), and deep water formation in the North Atlantic takes place in the central Labrador Sea and the Nordic Seas.

The definition of the AMOC in the model at any latitude is straightforward, as the full velocity field is known and only a simple zonal and depth integration has to be performed. For my analysis, I have defined the AMOC as the maximum of the overturning streamfunction, although the results do not change appreciably if values are taken at a fixed depth (for example 1000 m). Similarly, the modeled meridional heat transport can be readily computed from the velocity, temperature and salinity fields.

Precisely defining the DWBC in a model is more complicated. In observations, the DWBC is conventionally defined in density classes instead of depth layers because the three water masses that constitute the DWBC (Labrador Sea Water, Iceland-Scotland Overflow Water, Denmark Strait Overflow Water) have specific temperature and salinity properties according to the formation processes, and are not found at the same depth throughout the entire North Atlantic due to differences in ocean stratification. A definition in depth layers would therefore be imprecise.

Unfortunately, observationally established density classes cannot be directly applied to a model because of temperature and salinity biases. Instead, for the definition of model-specific density classes, I have compared observed western boundary temperatures and salinities at 26°N and Line W with the corresponding model output to identify the density classes in the model.

In addition to the vertical limit of the model DWBC, it is also necessary to define the zonal extent of the modeled DWBC. At many latitudes, the DWBC is a very narrow current with a width of less than 200 km. As the flow field in the North Atlantic is complicated with permanent and non-permanent recirculations and eddies, a careful analysis of the velocity field is required for each time step. Furthermore, the DWBC is not clearly confined at all latitudes,

especially between 35°N and 45°N.

The comparison between observed and modeled DWBC variability is complicated by the fact that a specific latitude in the real ocean is not necessarily dynamically equivalent to the same nominal latitude in the model world. For example in the particular model used here, the Gulf Stream separation is located further south than in the real ocean. Therefore, I have in some cases (for example at Line W) adjusted the nominal latitude for a more comparable latitude.

6.1.2 Timescales and latitudinal scope

Although model data are output at daily resolution, I have focused my analysis on the more climatically relevant seasonal to decadal timescales. Also, the 41°N AMOC observations are only available as three-month running means.

The seasonal variability of the AMOC, its associated meridional heat transport and the DWBC are analysed in both model and the available observations at 26°N, Line W and 41°N. I have investigated the coherence of the AMOC in the observed time series, but complement the analysis with the model results for a broader analysis of the AMOC's latitude dependence between 20°N and 55°N. Because of the more challenging definition of a modeled DWBC, I have limited the analysis of the DWBC in the model to five locations between 26°N and 48°N.

As the available observed time series are too short, the decadal variability of both the AMOC and the DWBC, as well as their coherence on these timescales is analysed only in the model. The observed DWBC's mean, structure and range of temporal variability are well-represented in the model (Chapter 4), although a quantitative comparison between the observed and modeled time series is not possible due to the amount of high-frequency variability in the

DWBC and the shortness of the observed time series. The observed AMOC's mean and variability are well-represented at 26°N, but there are phasing differences between model and observations at 41°N (Chapter 2 and Section 6.2.1).

6.2 Main results

In the following, I present the main results of the thesis by answering the questions raised in the introduction.

6.2.1 Are AMOC observations at one latitude representative of the AMOC variability at other latitudes?

After subtracting the wind-induced Ekman transport from the AMOC, the seasonal cycle of the internal, non-Ekman component of the transport, which dominates the northward heat transport, is covariable between 26°N and 41°N (Chapter 2). The phasing in the model differs from the observed phasing: In the observations, the non-Ekman component at 26°N has a maximum in fall and a minimum in spring, while at 41°N, the maximum occurs in spring and the minimum occurs in fall. In the model, the non-Ekman component's seasonal cycle is coherent throughout the entire North Atlantic, with a maximum in fall and a minimum in spring.

The reason for the discrepancy between modeled and observed AMOC seasonal cycles at 41°N is to date unclear, although Xu et al. (2014) find similar coherent seasonality in a different model. Previous studies have suggested that the AMOC variability might be gyre-specific. Indeed, both the Sverdrup transport (Chapter 2) and the modeled DWBC (Chapter 4 and Section 6.2.2) transport show opposing seasonality between the subpolar and the subtropical gyre. Simulating the method that is used for the estimation of the observed

AMOC at 41°N, which differs substantially from the method that is used at 26°N (Section 1.3), in this particular model would shed light on this issue.

After removing the seasonal cycle, the observed non-Ekman components of the AMOC are covariable between 26°N and 41°N, but the relation is non-stationary (Chapter 2). Specifically, they show opposing behavior for the first years of the time series, but both times series have an exceptional downturn in the winter of 2009/10. This implies that the downturn is not only related to a weakening of the wind-induced transport, but also to a coherent signal in the geostrophic transport. There is no relation between the modeled non-Ekman components at 26°N and 41°N after the seasonal cycle is removed. However, if the seasonal cycle is not removed, the modeled AMOC is coherent throughout the North Atlantic on interannual timescales.

On decadal timescales (Chapter 5), my analysis of the model results suggests a coherent AMOC throughout the North Atlantic, with no lag between subpolar and subtropical gyre. It should be noted that the depth representation that is used for the computation of the AMOC might not be the best choice at the higher latitudes. Here, northward and southward flow often occur at the same depth, but at different densities, and so part of the flow cancels out if one integrates over depth classes.

Although the phasing differences between model and observations at 41°N are not yet fully resolved and an analysis of the AMOC variability in density layers might be useful, the results from both model and observations suggest that the AMOC estimates at 26°N and 41°N are representative of the AMOC's variability on a broad range of adjacent latitudes on all timescales. This has implications for the seasonal heat storage in the North Atlantic, and might help further the understanding of the relation of AMOC variations and sea surface temperature.

As a follow-up to the analysis of the seasonal variability of the AMOC, the seasonal variability of the modeled and observed meridional heat transport was

also investigated (Chapter 3). At 41°N, I find a three-month shift between the modeled and observed heat transport variability, although the observed mean is well-represented in the observations. At 26°N, there is a high agreement between modeled and observed heat transport, while the mean is severely underestimated. The underestimation of the mean transport at 26°N might be due to temperature biases in the model, or a misrepresentation of the gyre transport in the model. This would be consistent with the fact that the mean observed heat transport is better represented at 41°N, since the gyre transport is not associated with the AMOC whose mean is well-represented in the model at both latitudes. As 41°N is located at the gyre boundary, a large contribution from the gyre is not to be expected at this latitude.

I find that the AMOC is closely related to the meridional heat transport at subtropical and mid-latitudes. However, the relation breaks down further north. A preliminary analysis (Chapter 3) shows that the Ekman and non-Ekman components of mass and heat transport are correlated even at high latitudes. But here, the heat transport's variability is mainly determined by the non-Ekman component, while the Ekman component is more important for the AMOC. The different seasonality of the Ekman and non-Ekman components at the high latitudes therefore results in a disagreement between AMOC and heat transport variability. In conclusion, the AMOC is an adequate measure for the meridional heat transport in the subtropical gyre and at mid-latitudes, while a close correspondence cannot be assumed at higher latitudes.

6.2.2 Can changes in convection activity be observed in the subtropical DWBC?

I find that the variability of the DWBC is determined by the local wind stress curl variability on both seasonal (Chapter 4) and decadal timescales (Chapter 5). Specifically, I find a high correspondence between the wind stress curl

at the western boundary and the transport in the DWBC at the same latitude, especially in the subtropical gyre. Hence, signals related to deep water formation at the higher latitudes are masked by more energetic wind-driven variability further south.

As a result of the close relation between the DWBC and the local wind stress curl, the DWBC has a well-defined seasonal cycle at all investigated latitudes, which is coherent both in the subpolar and the subtropical gyre, but not across the gyre boundary: In the subtropical gyre, the southward transport in the DWBC transport is strongest in fall and weakest in late winter, while in the subpolar gyre, the maximum occurs in late winter and the minimum occurs in late summer.

On decadal timescales, the modeled DWBC is coherent throughout most of the North Atlantic, with the exception of the modeled Line W. Here, the boundary wind stress curl has a positive anomaly during the first half of the time series, while the wind stress curl anomaly is negative at the other latitudes. Nevertheless, the DWBC is coherent across a broad range of latitudes.

Future work might further quantify the relation between the DWBC and the boundary wind stress curl on both seasonal and decadal timescales. Eventually, an estimate of the DWBC's variability throughout the subtropical North Atlantic could be obtained from satellite wind data.

6.2.3 Can observations of the DWBC be used as a proxy for AMOC observations?

The close relation of the DWBC with the local wind stress curl implies that AMOC variations cannot easily be inferred from DWBC observations (Chapters 4 and 5).

The seasonal cycle of the DWBC agrees with the seasonal cycle of the deep transports west of the Mid-Atlantic Ridge, but the deep transports east of the Mid-Atlantic Ridge show opposing seasonality (Chapter 4). Although the western basin seasonal cycle is more dominant, as it has a higher seasonal amplitude, the AMOC's seasonal cycle is shifted by two months compared to the western basin (and DWBC) seasonal cycle due to the influence of the eastern basin. Energetic high-frequency variability in the DWBC further complicates the relation with the basin-wide transports.

While the deep eastern and western basins are separated by the Mid-Atlantic Ridge throughout the subtropical North Atlantic, the anti-correlation between the eastern and western basin transports shows that they are not unrelated. It is therefore unclear whether changes in the western basin seasonal cycle, which might be apparent in the DWBC seasonal cycle, would be reflected in the AMOC seasonal cycle, or be compensated by variability in the eastern basin.

On decadal timescales (Chapter 5), the non-stationary relation between the wind stress curl in the basin interior and the wind stress curl at the western boundary results in a non-stationary relation between AMOC and DWBC. While the DWBC is related to the boundary wind stress curl variability, the AMOC's variability is determined by the basin-wide atmospheric conditions. Thus, if the wind stress curl anomalies at the western boundary and in the basin interior are of opposite sign, the AMOC and the DWBC show opposing behavior as well.

Combining an estimate of the DWBC from the local wind stress curl variability with an upper ocean velocity field obtained from Argo data, as for the 41°N AMOC estimate, could yield an improved picture of the basin-wide circulation across a wide range of latitudes. On decadal timescales, observations of the DWBC could be used as a proxy for the AMOC variability if the boundary and basin-wide wind stress curl are in phase.

7 Bibliography

Atkinson, C., Bryden, H. L., Cunningham, S. A., and King, B. A. (2012). Atlantic transport variability at 25°N in six hydrographic sections. *Ocean Science*, **8**, 497–523.

Atkinson, C. P., Bryden, H. L., Hirschi, J. J.-M., and Kanzow, T. (2010). On the seasonal cycles and variability of Florida Straits, Ekman and Sverdrup transports at 26°N in the Atlantic Ocean. *Ocean Science*, **6**, 853–859.

Bacon, S. (1998). Decadal variability in the outflow from the Nordic seas to the deep Atlantic Ocean. *Nature*, **394**, 871–873.

Baehr, J., Cunningham, S. A., Haak, H., Heimbach, P., Kanzow, T., and Marotzke, J. (2009). Observed and simulated estimates of the meridional overturning circulation at 26.5°N in the Atlantic. *Ocean Science*, **5**, 575–589.

Baehr, J., Hirschi, J. J.-M., Beismann, J.-O., and Marotzke, J. (2004). Monitoring the meridional overturning circulation in the North Atlantic: A model-based array-design study. *Journal of Marine Research*, **62**, 283–312.

Balan Sarojini, B., Gregory, J. M., Tailleux, R., Bigg, G. R., Blaker, A. T., Cameron, D. R., Edwards, N. R., Megann, A. P., Shaffrey, L. C., and Sinha, B. (2011). High-frequency variability of the Atlantic meridional overturning circulation. *Ocean Science*, **7**, 471–486.

Biastoch, A., Böning, C. W., Getzlaff, J., Molines, J.-M., and Madec, G. (2008). Causes of Interannual-Decadal Variability in the Meridional Overturning Circulation of the Midlatitude North Atlantic. *Journal of Climate*, **21**, 6599–6615.

Bingham, R. J., Hughes, C. W., Roussenov, V., and Williams, R. G. (2007). Meridional coherence of the North Atlantic meridional overturning circulation. *Geophysical Research Letters*, **34**, L23606.

Böning, C., Döscher, R., and Budich, R. G. (1991). Seasonal Transport Variation in the Western Subtropical North Atlantic: Experiments with and Eddy-resolving Model. *Journal of Physical Oceanography*, **21**, 1271–1289.

Böning, C. W., Dieterich, C., Barnier, B., and Jia, Y. (2001). Seasonal cycle of meridional heat transport in the subtropical North Atlantic: a model intercomparison in relation to observations near 25°N. *Progress in Oceanography*, **48**, 231–253.

Böning, C. W., M., S., Dengg, J., Biastoch, A., and Funk, A. (2006). Decadal variability of subpolar gyre transport and its reverberation in the North Atlantic overturning. *Geophysical Research Letters*, **33**.

Bower, A., Lozier, S., and Gary, S. (2011). Export of Labrador Sea Water from the subpolar North Atlantic: A Lagrangian perspective. *Deep-Sea Research II*, **58**, 1798–1818.

Bower, A. S., Lozier, M. S., Gary, S., and Boening, C. W. (2009). Interior pathways of the North Atlantic meridional overturning circulation. *Nature*, **459**, 243–248.

Bryan, K. (1982). Seasonal variation in meridional overturning and poleward heat transport in the Atlantic and Pacific Oceans: A model study. *Journal of Marine Research*, **40**, 39–53.

Bryden, H. L., Johns, W. E., and Saunders, P. M. (2005). Deep western boundary current east of Abaco: Mean structure and transport. *Journal of Marine Research*, **63**, 35–57.

Bryden, H. L., King, B. A., McCarthy, G. D., and McDonagh, E. L. (2014). Impact of a 30% reduction in atlantic meridional overturning during 2009-2010. *Ocean Science*, **10**, 683–691.

Church, J. A. (2007). A Change in Circulation? *Science*, **317**, 908–909.

Cunningham, S. A., Kanzow, T., Rayner, D., Baringer, M. O., Johns, W. E., Marotzke, J., Longworth, H. R., Grant, E. M., Hirschi, J. J.-M., Beal, L. M., Meinen, C. S., and Bryden, H. L. (2007). Temporal Variability of the Atlantic Meridional Overturning Circulation at 26.5°N. *Science*, **317**, 935–938.

Dee, D. P., Uppala, S. M., Simmons, A. J., Berrisford, P., Poli, P., Kobayashi, S., Andrae, U., Balmaseda, M. A., Balsamo, G., Bauer, P., Bechtold, P., Beljaars, A. C. M., van de Berg, L., Bidlot, J., Bormann, N., Delsol, C., Dragani, R., Fuentes, M., Geer, A. J., Haimberger, L., Healy, S. B., Hersbach, H., Hólm, E. V., Isaksen, L., Kållberg, P., Köhler, M., Matricardi, M., McNally, A. P., Monge-Sanz, B. M., Morcrette, J.-J., Park, B.-K., Peubey, C., de Rosnay, P., Tavolato, C., Thépaut, J.-N., and Vitart, F. (2011). The ERA-Interim reanalysis: configuration and performance of the data assimilation system. *Quarterly Journal of the Royal Meteorological Society*, **137**, 553–597.

Dengler, M., Fischer, J., Schott, F., and Zantopp, R. (2006). Deep Labrador Current and its variability in 1996-2005. *Geophysical Research Letters*, **33**, L21S06.

Dickson, R., Lazier, J., Meincke, J., Rhines, P., and Swift, J. (1996). Long-term coordinated changes in the convective activity of the North Atlantic. *Progress in Oceanography*, **38**, 241 – 295.

Drijfhout, S. S. and Hazeleger, W. (2006). Changes in MOC and gyre-induced Atlantic Ocean heat transport. *Geophysical Research Letters*, **33**, L077077.

Eden, C. and Willebrand, J. (2001). Mechanism of Interannual to Decadal Variability of the North Atlantic Circulation. *Journal of Climate*, **14**.

Elipot, S., Hughes, C., Olhede, S., and Toole, J. (2013). Coherence of Western Boundary Pressure at the RAPID WAVE Array: Boundary Wave Adjustments or Deep Western Boundary Current Advection? *Journal of Physical Oceanography*, **43**, 744–765.

Fischer, J., Karstensen, J., Zantopp, R., Visbeck, M., Biastoch, A., Behrens, E., Böning, C. W., Quadfasel, D., Jochumsen, K., Valdimarsson, H., Jónsson, S., Bacon, S., Holliday, N. P., Dye, S., Rhein, M., and Mertens, C. (2014a). Intra-seasonal variability of the DWBC in the western subpolar North Atlantic. *Progress in Oceanography*, , in press.

Fischer, J. and Schott, F. A. (2002). Labrador Sea Water Tracked by Profiling FloatsFrom the Boundary Current into the Open North Atlantic. *Journal of Physical Oceanography*, **32**, 573–584.

Fischer, M., Domeisen, D. I. V., Müller, W. A., and Baehr, J. (2014b). The Atlantic meridional heat transport seasonal cycle in a CMIP5 climate projection. , in preparation.

Fuglister, F. C. (1960). Atlantic Oceans Atlas of Temperature and Salinity Profiles and Data from the International Geophysical Year of 19571958. *The Woods Hole Oceanographic Institution Atlas Series*, **1**.

Ganachaud, A. and Wunsch, C. (2003). Large-Scale Ocean Heat and Freshwater Transports during the World Ocean Circulation Experiment. *Journal of Climate*, **16**, 696–705.

Gary, S., Lozier, M. S., Biastoch, A., and Böning, C. W. (2012). Reconciling tracer and float observations of the export pathways of Labrador Seas Water. *Geophysical Research Letters*, **39**, L24606.

Gary, S. F., Lozier, M. S., Böning, C. W., and Biastoch, A. (2011). Deciphering the pathways for the deep limb of the Meridional Overturning Circulation. *Deep Sea Research, Part II*, **58**, 1781–1797.

Getzlaff, J., Böning, C. W., Eden, C., and Biastoch, A. (2005). Signal propagation related to the North Atlantic overturning. *Geophysical Research Letters*, **32**, L09602.

Gregory, J. M., Dixon, K. W., Stouffer, R. J., Weaver, A. J., Driesschaert, E., Eby, M., Fichefet, T., Hasumi, H., Hu, A., Jungclaus, J. H., Kamenkovich, I. V., Levermann, A., Montoya, M., Murakami, S., Nawrath, S., Oka, A., Sokolov, A. P., and Thorpe, R. B. (2005). A model intercomparison of changes in the Atlantic thermohaline circulation in response to increasing atmospheric CO_2 concentration. *Geophysical Research Letters*, **32**, L12703.

Hirschi, J., Baehr, J., Marotzke, J., Stark, J., Cunningham, S., and Beismann, J. O. (2003). A monitoring design for the Atlantic meridional overturning circulation. *Geophysical Research Letters*, **30**, 1413.

Hobbs, W. R. and Willis, J. (2012). Midlatitude North Atlantic heat transport: A time series based on satellite and drifter data. *Journal of Geophysical Research*, **117**, C01008.

IPCC (2013). *Climate Change 2013: The Physical Science Basis. Working Group I Contribution to the Fifth Assessment Report of the Intergovernmental Panel on Climate Change*. Edited by Stocker, T. F., Qin, D., Plattner, G.-K., Tignor, M. M. B., Allen, S. K., Boschung, J., Nauels, A., Xia, Y., Bex, V., and Midgley, P. M. Cambridge University Press.

Jayne, S. and Marotzke, J. (2001). The dynamics of ocean heat transport variability. *Reviews of Geophysics*, **39**, 385–411.

Jia, Y. (2003). Ocean heat transport and its relationship to ocean circulation in the CMIP coupled models. *Climate Dynamics*, **20**, 153–174.

Jochumsen, K., Quadfasel, D., Valdimarsson, H., and Jonsson, S. (2012). Variability of the Denmark Strait overflow: Moored timeseries from 1996-2011. *Journal of Geophysical Research*, **117**.

Johns, W. E., Baringer, M. O., Beal, L. M., Cunningham, S. A., Kanzow, T., Bryden, H. L., Hirschi, J. J.-M., Marotzke, J., Meinen, C. S., Shaw, B., and Curry, R. (2011). Continuous, Array-Based Estimates of Atlantic Ocean Heat Transport at 26.5°N. *Journal of Climate*, **24**, 2429–2449.

Johns, W. E., Beal, L. M., Baringer, M. O., Molina, J. R., Cunningham, S. A., Kanzow, T., and Rayner, D. (2008). Variability of Shallow and Deep Western Boundary Currents off the Bahamas during 2004-05: Results from the 26°N RAPID-MOC Array. *Journal of Physical Oceanography*, **38**, 605–623.

Johnson, H. L. and Marshall, D. P. (2002). Localization of abrupt change in the North Atlantic thermohaline circulation. *Geophysical Research Letters*, **29**, 1083.

Jung, T., Vitart, F., Ferranti, L., and Morcrette, J.-J. (2011). Origin and predictability of the extreme negative NAO winter of 2009/10. *Geophysical Research Letters*, **38**, L07701.

Jungclaus, J. H., Fischer, N., Haak, H., Lohmann, K., Marotzke, J., Matei, D., Mikolajewicz, U., Notz, D., and von Storch, J. S. (2013). Characteristics of the ocean simulations in the Max Planck Institute Ocean Model (MPIOM) the ocean component of the MPI-Earth system model. *Journal of Advances in Modeling Earth Systems*, **5**, 422–446.

Jungclaus, J. H., Keenlyside, N., Botzet, M., Haak, H., Luo, J.-J., Latif, M., Marotzke, J., Mikolajewicz, U., and Roeckner, E. (2006). Ocean circulation and tropical variability in the coupled model ECHAM5/MPI-OM. *Journal of Climate*, **19**, 3952–3972.

Kalnay, E., Kanamitsu, M., Kistler, R., Collins, W., Deaven, D., Gandin, L., Iredell, M., Saha, S., White, G., Woollen, J., Zhu, Y., Leetmaa, A.,

Reynolds, R., Chelliah, M., Ebisuzaki, W., Higgins, W., Janowiak, J., Mo, K. C., Ropelewski, C., Wang, J., Jenne, R., and Joseph, D. (1996). The NCEP/NCAR 40-Year Reanalysis Project. *Bulletin of the American Meteorological Society*, **77**, 437–471.

Kanzow, T., Cunningham, S. A., Johns, W. E., Hirschi, J. J.-M., Marotzke, J., Baringer, M. O., Meinen, C. S., Chidichimo, M. P., Atkinson, C. P., Beal, L. M., Bryden, H. L., and Collins, J. (2010). Seasonal Variability of the Atlantic Meridional Overturning Circulation at 26.5°N. *Journal of Climate*, **23**, 5678–5698.

Kanzow, T., Cunningham, S. A., Rayner, D., Hirschi, J. J.-M., Johns, W. E., Baringer, M. O., Bryden, H. L., Beal, L. M., Meinen, C. S., and Marotzke, J. (2007). Observed Flow Compensation Associated with the MOC at 26.5°N in the Atlantic. *Science*, **317**, 938–941.

Kanzow, T., Send, U., and McCartney, M. (2008). On the variability of the deep meridional transports in the tropical north atlantic. *Deep Sea Research I*, **55**, 1601–1623.

Keenlyside, N. S., Latif, M., Jungclaus, J., Kornblueh, L., and Roeckner, E. (2008). Advancing decadal-scale climate prediction in the North Atlantic sector. *Nature*, **453**, 84–88.

Keller, K., Deutsch, C., Hall, M. G., and Bradford, D. F. (2007). Early Detection of Changes in the North Atlantic Meridional Overturning Circulation: Implications for the Design of Ocean Observation Systems. *Journal of Climate*, **20**, 145–157.

Kerr, R. A. (2005). The Atlantic Conveyor May Have Slowed, But Don't Panic Yet. *Science*, **310**, 1403–1405.

Kieke, D. and Rhein, M. (2006). Variability of the Overflow Water Transport in the Western Subpolar North Atlantic, 1950-97. *Journal of Physical Oceanography*, **36**, 435–455.

Knight, J. R., Allan, R. J., Folland, C. K., Vellinga, M., and Mann, M. E. (2005). A signature of persistent natural thermohaline circulation cycles in observed climate. *Geophysical Research Letters*, **32**, L20708.

Lee, T. N., Johns, W., Zantopp, R., and Fillenbaum, E. R. (1996). Moored observations of the Western Boundary Current variability and thermohaline circulation at 26.5°N in the subtropical North Atlantic. *Journal of Physical Oceanography*, **26**, 962–983.

Lee, T. N., Johns, W., Zantopp, R., and Schott, F. (1990). Western Boundary Current Structure and Variability East of Abaco, Bahamas, at 26.5°N. *Journal of Physical Oceanography*, **20**, 446–466.

Levermann, A., Griesel, A., Hofmann, M., Montoya, M., and Rahmstorf, S. (2005). Dynamic sea level changes following changes in the thermohaline circulation. *Climate Dynamics*, **24**, 347–354.

Longworth, H. R. and Bryden, H. L. (2013). Discovery and Quantification of the Atlantic Meridional Overturning Circulation: The Importance of 25°N. In *Ocean Circulation: Mechanisms and Impact – Past and Future Changes of Meridional Overturning*. American Geophysical Union.

Lozier, M. S. (1997). Evidence for Large-Scale Eddy-Driven Gyres in the North Atlantic. *Science*, **277**, 361–364.

Lozier, M. S. (2010). Deconstructing the Conveyor Belt. *Science*, **328** (5985), 1507–1511.

Lozier, M. S. (2012). Overturning in the North Atlantic. *Annual Review of Marine Science*, **4**, 291–315.

Lozier, M. S., Roussenov, V., Reed, M. S. C., and Williams, R. G. (2010). Opposing decadal changes of the North Atlantic meridional overturning circulation. *Nature Geoscience*, **3**, 728–734.

Lumpkin, R. and Speer, K. (2007). Global ocean meridional overturning. *Journal of Physical Oceanography*, **37**, 25502562.

Marotzke, J., Giering, R., Zhang, K. Q., Stammer, D., Hill, C., and Lee, T. (1999). Construction of the adjoint MIT ocean general circulation model and application to Atlantic heat transport sensitivity. *Journal of Geophysical Research: Oceans*, **104**, 29529–29547.

Marshall, J. and Schott, F. (1999). Open-ocean convection: Observations, theory, and models. *Reviews of Geophysics*, **37**, 1–64.

Marsland, S. J., Haak, H., Jungclaus, J. H., Latif, M., and Röske, F. (2003). The Max-Planck-Institute global ocean/sea ice model with orthogonal curvilinear coordinates. *Ocean Modelling*, **5**, 91–127.

McCarthy, G. and, F.-W. E., Johns, W. E., Baringer, M. O., Meinen, C. S., Bryden, H. L., Rayner, D., Duchez, A., Roberts, C., and Cunningham, S. A. (2012). Observed interannual variability of the Atlantic meridional overturning circulation at 26°N. *Geophysical Research Letters*, **39**, L19609.

McCartney, M. S. (1992). Recirculating components to the deep boundary current of the northern North Atlantic. *Progress in Oceanography*, **29**, 283–383.

Meinen, C. S., Baringer, M. O., and Garcia, R. F. (2010). Florida Current transport variability: An analysis of annual and longer-period signals. *Deep Sea Research, Part I*, **57**, 835–846.

Meinen, C. S., Johns, W. E., Garzoli, S. L., van Sebille, E., Rayner, D., Kanzow, T., and Baringer, M. O. (2013a). Variability of the Deep Western Boundary Current at 26.5°N during 2004-2009. *Deep Sea Research II*, **85**, 154–168.

Meinen, C. S., Speich, S., Perez, R. C., Dong, S., Piola, A. R., Garzoli, S. L., Baringer, M. O., Gladyshev, S., and Campos, E. J. D. (2013b). Temporal

variability of the meridional overturning circulation at 34.5°S: Results from two pilot boundary arrays in the South Atlantic. *Journal of Geophysical Research*, **118**, 64616478.

Mielke, C., Frajka-Williams, E., and Baehr, J. (2013). Observed and simulated variability of the AMOC at 26°N and 41°N. *Geophysical Research Letters*, **40**, 1159–1164.

Molinari, R. L., Fine, R. A., and Johns, E. (1992). The Deep Western Boundary Current in the tropical North Atlantic Ocean. *Deep-Sea Research I*, **39**, 1967–1984.

Molinari, R. L., Fine, R. A., Wilson, W. D., Curry, R. G., Abell, J., and McCartney, M. S. (1998). The arrival of recently formed Labrador Sea Water in the Deep Western Boundary Current at 26.5°N. *Geophysical Research Letters*, **25**, 2249–2252.

Msadek, R., Johns, W. E., Yeager, S. G., Donabasoglu, G. amd Delworth, T. L., and Rosati, A. (2013). The Atlantic Meridional Heat Transport at 26.5°N and Its Relationship with the MOC in the RAPID Array and the GFDL and NCAR Coupled Models. *Journal of Climate*, **26**, 4335–4356.

Munoz, E., Kirtman, B., and Weijer, W. (2011). Varied representation of the Atlantic meridional overturning across multidecadal ocean reanalyses. *Deep Sea Research, Part II*, **58**, 1848–1857.

Olbers, D., Willebrand, J., and Eden, C. (2012). *Ocean Dynamics*. Springer.

Peña-Molino, B., Joyce, T. M., and Toole, J. M. (2012). Variability in the Deep Western Boundary Current: Local versus remote forcing. *Journal of Geophysical Research*, **117**, C12022.

Quadfasel, D. and Käse, R. (2013). Present-Day Manifestation of the Nordic Seas Overflows. In *Ocean Circulation: Mechanisms and Impact – Past and Future Changes of Meridional Overturning*. American Geophysical Union.

Rayner, D., Hirschi, J. J.-M., Kanzow, T., Johns, W. E., Wright, P. G., Frajka-Williams, E., Bryden, H. L., Meinen, C. S., Baringer, M. O., Marotzke, J., Beal, L. M., and Cunningham, S. A. (2011). Monitoring the Atlantic meridional overturning circulation. *Deep-Sea Research II*, **58**, 1744–1753.

Rhein, M., Fischer, J., Smethie, W. M., Smythe-Wright, D., Weiss, R. F., Mertens, C., Min, D.-H., Fleischmann, U., and Putzka, A. (2002). Labrador Sea Water: Pathways, CFC Inventory, and Formation Rates. *Journal of Physical Oceanography*, **32**, 648–665.

Richardson, P. L. (1983). Eddy kinetic energy in the North Atlantic from surface drifters. *Journal of Geophysical Research*, **88**, 4355–4367.

Richardson, P. L. (2008). On the history of meridional overturning circulation schematic diagrams. *Progress in Oceanography*, **76**, 466–486.

Riser, S. C. and Lozier, M. S. (2013). Rethinking the Gulf Stream. *Scientific American*, **308**, 50–55.

Sarafanov, A., Falina, A., Lherminier, P., Mercier, H., Sokov, A., and Gourcuff, C. (2010). Assessing decadal changes in the Deep Western Boundary Current absolute transport southeast of Cape Farewell, Greenland, from hydrography and altimetry. *Journal of Geophysical Research*, **115**, C11003.

Schmittner, A. (2005). Decline of the marine ecosystem caused by a reduction in the Atlantic overturning circulation. *Nature*, **434**, 628–633.

Schmittner, A., Brook, E. J., and Ahn, J. (2013). Impact of the ocean's Overturning circulation on atmospheric CO_2. In *Ocean Circulation: Mechanisms and Impacts – Past and Future Changes of Meridional Overturning*. American Geophysical Union.

Schott, F. A., Fischer, J., Dengler, M., and Zantopp, R. (2006). Variability of the Deep Western Boundary Current east of the Grand Banks. *Geophysical Research Letters*, **33**, L21S07.

Seager, R., Kushnir, Y., Nakamura, J., Ting, M., and Naik, N. (2010). Northern Hemisphere winter snow anomalies: ENSO, NAO and the winter of 2009/10. *Geophysical Research Letters*, **37** (14), L14703.

Smeed, D. A., McCarthy, G. D., Cunningham, S. A., Frajka-Williams, E., Rayner, D., Johns, W. E., Meinen, C. S., Baringer, M. O., Moat, B. I., Duchez, A., and Bryden, H. L. (2014). Observed decline of the Atlantic meridional overturning circulation 2004-2012. *Ocean Science*, **10**, 29–38.

Steele, M., A., M., and Ermold, W. (2001). PHC: A Global Ocean Hydrography with a High-Quality Arctic Ocean. *Journal of Climate*, **14**, 2079–2087.

Stommel, H. (1957). A survey of ocean current theory. *Deep-Sea Research*, **4**, 149–184.

Stommel, H. and Arons, A. (1959-1960). On the abyssal circulation of the world ocean – II. An idealized model of the circulation pattern and amplitude in oceanic basins. *Deep Sea Research*, **6**, 217–233.

Sutton, R. T. and Hodson, D. L. R. (2005). Atlantic Ocean forcing of North American and European summer climate. *Science*, **309**, 115–118.

Swallow, J. and Worthington, L. (1961). An observation of a deep countercurrent in the Western North Atlantic. *Deep Sea Research*, **8**, 1–IN3.

Taws, S. L., Marsh, R., Wells, N. C., and Hirschi, J. J.-M. (2011). Re-emerging ocean temperature anomalies in late-2010 associated with a repeat negative NAO. *Geophysical Research Letters*, **38**.

Toole, J. M., Curry, R. G., Joyce, T. M., McCartney, M., and Peña-Molino, B. (2011). Transport of the North Atlantic Deep Western Boundary Current abut 39°N, 70°W: 2004-2008. *Deep-Sea Research II*, **58**, 1768–1780.

van Sebille, E., Baringer, M. O., Johns, W. E., Meinen, C. S., Beal, L. M., de Jong, M. F., and van Aken, H. M. (2011). Propagation of classical

Labrador Sea water from its source region to 26°N. *Journal of Geophysical Research*, **116**, C12027.

Vellinga, M. and Wood, R. (2002). Global Climatic Impacts of a Collapse of the Atlantic Thermohaline Circulation. *Climatic Change*, **54**, 251–267.

von Storch, J.-S., Eden, C., Fast, I., Haak, H., Hernandez-Deckers, D., Maier-Reimer, E., Marotzke, J., and Stammer, D. (2012). An estimate of Lorenz Energy Cycle for the World Ocean Based on the 1/10° STORM/NCEP Simulation. *Journal of Physical Oceanography*, **42**, 2185–2205.

Willis, J. (2010). Can in situ floats and satellite altimeters detect long-term changes in Atlantic Ocean overturning? *Geophysical Research Letters*, **37**, L06602.

Willis, J. K. and Fu, L.-L. (2008). Combining altimeter and subsurface float data to estimate the time-averaged circulation in the upper ocean. *Journal of Geophysical Research*, **113**, C12017.

Wunsch, C. (2005). The Total Meridional Heat Flux and Its Oceanic and Atmospheric Partition. *Journal of Climate*, **18**, 4374–4380.

Wunsch, C. (2008). Mass and volume transport variability in an eddy-filled ocean. *Nature Geoscience*, **1**, 165–168.

Xu, X., Chassignet, E. P., Johns, W. E., Schmitz, W. J., and Metzger, E. J. (2014). Intraseasonal to interannual variability of the Atlantic meridional overturning circulation from eddy-resolving simulations and observations. *Journal of Geophysical Research*, **119**, 5140–5159.

Xu, X., Schmitz, W. J., Hurlburt, H. E., and Hogan, P. J. (2012). Mean Atlantic meridional overturning circulation across 26.5°N from eddy-resolving simulations compared to observations. *Journal of Geophysical Research*, **117**, C03042.

Yang, J. and Joyce, T. M. (2003). How do high-latitude North Atlantic climate signals the crossover between the Deep Western Boundary Current and the Gulf Stream? *Geophysical Research Letters*, **30**, 1070.

Yashayaev, I. (2007). Hydrographic changes in the Labrador Sea, 1960-2005. *Progress in Oceanography*, **73**, 242–276.

Yeager, S., Karspeck, A., Danabasoglu, G., Tribbia, J., and Teng, H. (2012). A Decadal Prediction Case Study: Late Twentieth-Century North Atlantic Ocean Heat Content. *Journal of Climate*, **25**, 5173–5189.

Zhang, R. (2010). Latitudinal dependence of Atlantic meridional overturning circulation (AMOC) variations. *Geophysical Research Letters*, **37**, L16703.

Zhang, R. and Delworth, T. L. (2005). Simulated Tropical Response to a Substantial Weakening of the Atlantic Thermohaline Circulation. *Journal of Climate*, **18**, 1853–1860.

Zhang, R. and Delworth, T. L. (2006). Impact of Atlantic multidecadal oscillations on India/Sahel rainfall and Atlantic hurricanes. *Geophysical Research Letters*, **33**, L17712.

Acknowledgments

I am indebted to many people who have, through their support and encouragement, helped along the journey of my PhD.

First of all, thanks to my supervisor Johanna Baehr. Your guidance, advice and invaluable feedback have been a continuous motivation and inspiration.

Thanks also to Bjoern Stevens and Detlef Quadfasel for serving on my panel, and to the entire team of the IMPRS-ESM. I could not have asked for a better environment for my PhD.

Thanks to Eleanor Frajka-Williams, Stefan Gary, Kenji Shimizu and John Toole for fruitful discussions, and input. Thanks also to my all working group colleagues, both permanent and temporary. Special thanks to Bente Tiedje for sharing an office with me for almost three years.

Thanks to the scientists and crew of RRS Discovery cruise 382 for the opportunity to experience oceanography outside of a sheltered office, and to cross the Atlantic by ship.

Thanks also to my summer student, Fei Luo, for her help with the analysis and for letting me slip into the role of supervisor. I suspect I was the one learning the most.

Last but not least, many thanks to my family and friends for continued and unconditional support, and to Malte for being in my life.

Eidesstattliche Versicherung

Hiermit erkläre ich an Eides statt, dass ich die vorliegende Dissertationsschrift selbst verfasst und keine anderen als die angegebenen Quellen und Hilfsmittel benutzt habe.

Hamburg, den 11.11.2014

Charlotte Mielke

Hinweis / Reference

Die gesamten Veröffentlichungen in der Publikationsreihe des MPI-M
„Berichte zur Erdsystemforschung / Reports on Earth System Science“,
ISSN 1614-1199

sind über die Internetseiten des Max-Planck-Instituts für Meteorologie erhältlich:
http://www.mpimet.mpg.de/wissenschaft/publikationen.html

All the publications in the series of the MPI -M
„Berichte zur Erdsystemforschung / Reports on Earth System Science“,
ISSN 1614-1199

are available on the website of the Max Planck Institute for Meteorology:
http://www.mpimet.mpg.de/wissenschaft/publikationen.html